OUKA
The University of Osaka
Institutional Knowledge Archive

Title	Phase-Field Study on Solidification Microstructures of Crystalline Materials
Author(s)	Zhu, Chuanqi
Citation	大阪大学, 2023, 博士論文
Version Type	VoR
URL	https://doi.org/10.18910/92947
rights	
Note	

The University of Osaka Institutional Knowledge Archive : OUKA

https://ir.library.osaka-u.ac.jp/

The University of Osaka

Phase-Field Study on Solidification Microstructures of Crystalline Materials

フェーズフィールド法を用いた結晶性材料の凝固組織に関する研究

Chuanqi ZHU

朱伝奇

Division of Materials and Manufacturing Science
Graduate School of Engineering
Osaka University

2023/6

Abstract

The properties of crystalline materials depend largely on the microstructures formed during solidification processing. To control the solidification microstructures, the understanding of the motion of the solid-liquid interface is needed. The so-called "free boundary problem" describes the moving solid-liquid interface as a sharp plane associated with the mass/heat transport at the interface as well as in the bulk solid and liquid phases. Compared to this sharp interface model, the diffuse description of the solid-liquid interface is numerically efficient in obtaining the solution of the moving interface and its resulting microstructural morphology. The so-called phase-field method, which includes a diffuse interface in its thermodynamic formulation, has long been used to explore various microstructure problems on the nano- or micro-meter scale. The purpose of this work is to develop a framework of phase-field modeling based on the idea of diffuse interface and apply the numerical models to investigate the solidification microstructures of some industrially important materials. The content is arranged as follows: First, the fundamentals of the phase-field method, including the physical correlation, mathematical formulation, and numerical implementation, have been presented. The aim is to elaborate a way of phase-field modeling with consideration of both accuracy and efficiency. Second, to elucidate the extension mechanism of the grain boundaries during the directional solidification of multi-crystalline silicon, which is an important material in the solar cell industry, the phase-field model incorporated with anisotropic interface properties of faceted silicon crystal has been developed. The revealed mechanism of the interplay between the energetic and kinetic effects at the triple junction is believed to be a key knowledge for controlling the grain structure of multi-crystalline silicon. Third, a comprehensive study on the complex eutectic structure of $MoSi_2/Mo_5Si_3$, which is a promising candidate for ultra-high temperature material, has been presented. Based on the compari-

son between the numerical results and experimental observations, the formation mechanism of the script and inclined pattern of the embedded Mo_5Si_3 rods in the $MoSi_2$ has been discussed. Fourth, a new phase-field model for the alloy system with the so-called middle obstacle (MO) has been introduced to approximate its sharp interface counterpart. The velocity and morphology of the simulated dendrite tip can be independent of the artificial width of the diffuse interface. In addition, the model shows its capability of simulating the morphological transformation caused by non-equilibrium solute partitioning during rapid solidification. Overall, this work provides a framework for constructing phase-field models to elucidate the mechanisms underlying the formation of solidification microstructure for the development of advanced crystalline materials.

Keywords: Diffuse interface model; Solid-liquid interface; Facets; Eutectic; Dendrite; Non-equilibrium solute partitioning

Contents

Chapter 1 Introduction 9

1.1 Phase-field method 10

1.2 Materials of Concern 14

1.2.1 Directionally solidified multi-crystalline silicon 14

1.2.2 $MoSi_2/Mo_5Si_3$ eutectic with script lamellar pattern 16

1.2.3 Rapidly solidified aluminum alloy 17

1.3 Outline of This Study 19

Chapter 2 Idea of Diffuse Interface Model 33

2.1 Sharp and Diffuse Interface Models 34

2.2 Formulation 38

2.2.1 Free boundary problem 38

2.2.2 Correlation of diffuse and sharp interface models 43

2.2.3 Coupling with concentration field 48

2.2.4 Anisotropic interface properties 51

2.2.5 Multi-phase-field model 52

2.2.6 Phase-field-crystal model 55

2.3 Verification 60

2.3.1 Interface kinetics 60

2.3.2 Anisotropic shape 63

2.3.3 Alloy solidification 64

2.3.4 Solidification on the atomic scale 69

2.4 Conclusions 80

Chapter 3 Faceted Crystal Growth 87

3.1 Solidification of Multi-crystalline Silicon 88
3.2 Phase-Field Model of Silicon Solidification 92
3.2.1 Phase-field equation for multiple grains 92
3.2.2 Anisotropic surface properties of silicon crystal 93
3.3 Simulation of Silicon Solidification 97
3.3.1 Growth of single silicon grain 97
3.3.2 Growth of two misoriented grains 98
3.3.3 Growth of multiple misoriented grains 102
3.3.4 Three-dimensional simulation 106
3.4 Mechanisms of Grain Boundary Extension 110
3.4.1 Kinetic and energetic effects 111
3.4.2 Transformation of groove surfaces 113
3.4.3 Extension to 3D 114
3.4.4 Limitations of current model 115
3.5 Conclusions 115

Chapter 4 Complex Dual-phase Eutectic 125
4.1 Script Lamellar Pattern of $MoSi_2/Mo_5Si_3$ Eutectic 126
4.2 Analytical and Numerical models 130
4.2.1 Jackson-Hunt theory 130
4.2.2 Phase-field model of dual-phase growth 131
4.3 Growth Simulation of Regular Eutectic without Anisotropy 136
4.3.1 Analysis of interface undercooling 136
4.3.2 Spacing transition 138
4.3.3 Eutectic growth in three dimensions (3D) 142
4.4 Growth Simulation of Irregular Eutectic with Anisotropy 143
4.4.1 Lamellar discontinuity 143

4.4.2 Misfit accommodation at interphase boundary 151
4.5 Conclusions 157

Chapter 5 Rapid Solidification of Alloy 163
5.1 Non-equilibrium Solute Partitioning 164
5.2 Proposed Model for Rapid Solidification 167
5.2.1 Standard model of alloy solidification 167
5.2.2 Middle obstacle approach 172
5.3 Solidification Simulation of Al-Cu Alloy 179
5.3.1 Low growth rate 179
5.3.2 High growth rate 182
5.4 Conclusions 189

Chapter 6 Concluding Remarks 199

Achievements 205
Acknowledgments 209

.

Chapter 1

Introduction

New and advanced materials and processing technologies are continually needed to maintain the sustainability of human society [1]. Photovoltaic materials [2] can increase the usage of solar energy and reduce the consumption of fossil energy; materials that can withstand ultra-high temperature in gas turbines can enhance the efficiency of converting heat into work [3]; additive manufacturing enables the production of lightweight components with optimized micro- and macro-structures, expanding the application possibilities for traditional materials [4, 5]. On the other hand, as the fundamental process for almost all materials, solidification is an ancient technique dating back to the Bronze Age. In modern times, solidification technology is still of great importance as the precise control of the microscopic structure of solidified materials can dramatically improve their properties. As scientific research is motivated by either practical applications or experimental phenomena, the research on solidification lies at the intersection of the science and engineering of materials.

Basically, solidification is a phenomenon of phase transformation [6, 7], in which matters in their liquid states transform to solid states. The liquid can flow freely because the atoms that form the liquid are loosely bonded and in a state of disorder, in contrast to the atoms in the rigid solid, which are strongly

bonded and arranged in an ordered structure. For crystalline materials, of which the solid has a specific crystallographic symmetry, the solidification process starts from the emergence of small nuclei on the nanometer scale and ends up with big grains on the micrometer scale. The growth of these grains with anisotropic surface properties is also accompanied by the redistribution of solute in the case of alloy materials. The two simultaneous processes are mostly affected by the cooling conditions and give rise to a large variety of patterns under microscopic observation, which are also called microstructures. The mechanical, electronic, and magnetic properties of industrial materials are closely related to their microstructures formed during solidification [8, 9]. One of the main purposes of solidification research is to elucidate the effects of various solidification conditions and find ways of controlling the microstructure of solidified crystalline materials.

1.1 Phase-field method

The microscopic observation of the patterns on the micrometer scale is the main approach to gaining an understanding of the formation of solidification microstructures. However, the dynamic behaviors of moving interfaces cannot be fully revealed by the as-cast microstructures considering the interface motion can be affected by various factors, such as anisotropic interface properties, composition, cooling rate, and imposed electric and magnetic fields. To obtain the real-time process of the interface motion and gain deep insight into the microstructure formation, in-situ experiments are needed. When the interface velocity is on the order of one millimeter per second in traditional casting, its motion can be observed by either optical microscopy [10, 11, 12, 13] (Fig.1.1) or X-ray imaging method [14, 15, 16]. When the interface velocity is on the order of one meter per second during the laser melting process, the observation of the rapidly moving interface

has been achieved using time-resolved transmission electron microscopy (TRTEM) [17]. Despite the direct evidence obtained from in-situ observation, the characterization of microstructure and the elucidation of the underlying mechanism remains to be difficult because the observation is mostly limited to two-dimensional cross-sections. Additionally, carrying out experiments of in-situ observation is usually time-consuming and not cost-effective.

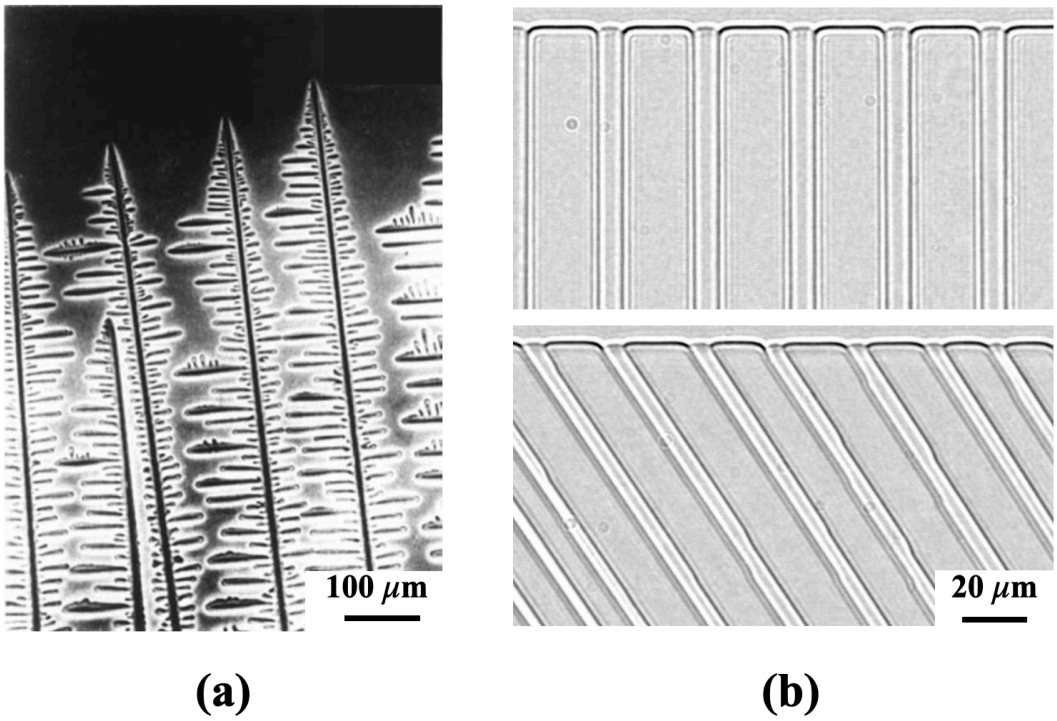

Figure 1.1: In-situ observations of patterns in solidification. (a)Columnar dendrites in a transparent organic alloy (After K.A. Jackson, Solidification, 1971 [10]); (b) lamellar eutectic ($(CBr_4$-$C_2Cl_6)$ during thin-sample directional solidification (After B. Caroli et al. 1992 [11]).

To accelerate the development of advanced materials and explore new materials, the numerical method [18], which is complementary to in-situ experiments, can be powerful for investigating microstructure problems in solidification. In the numerical simulation of microstructure formation, the phase-field method

[19, 20, 21, 22, 23, 24] stands out because of its description in the mesoscopic length that bridges the atomic to macroscopic lengths. The derivation of phase-field models can be consistent with the fundamental thermodynamic and kinetic principles [25, 26, 27], which are somewhat neglected in other numerical methods [28, 29]. The effect of surface tension and atomic attachment can be incorporated into the governing equation to describe the formation of complex patterns. The most celebrated example is the simulation of the dendrite structure, which was initiated by Kobayashi [30, 31] and followed by numerous researchers with a wide range of interests [32, 33, 34]

The core idea of the phase-field method is the microstructure evolution driven by energy minimization, which originates from the free energy description of the nonuniform system proposed by J. W. Cahn et al. [35, 36]. The free energy of the system is a function of a field variable that can represent the microstructure with bulk and interface regions. The field variable is also known as the order parameter in Landau Theory [19]. In solidification, which is the process of liquid-solid phase transformation, the field variable can be defined to indicate the local states, including solid, liquid, and interface. From the perspective of the atomic scale, the field variable is defined to be the atomic density that varies periodically in the solid with crystallographic symmetry and keeps almost unchanged in the liquid with randomly-arranged atoms [37, 38](Fig.1.2). From the mesoscale perspective, the periodicity of atoms can be averaged to indicate the local phase state. The field variable is then defined to be the phase density, which has constant but different values in solid and liquid phases and varies smoothly across the solid-liquid interface. This mesoscopic definition aligns with the name of the phase-field method and the field variable can be called "phase field". Consequently, the morphology of the solid-liquid interface, regardless of its geometrical complexity, can be described by the spatially-continuous phase field, which acts as the primary

variable in the formulation of the total free energy of the system. In addition, the free energy description enables the phase-field models to incorporate various physical processes by adding more types of field variables to the free energy, such as the temperature, composition, and crystallographic orientation, for simulating the realistic process of the solidification of crystalline materials.

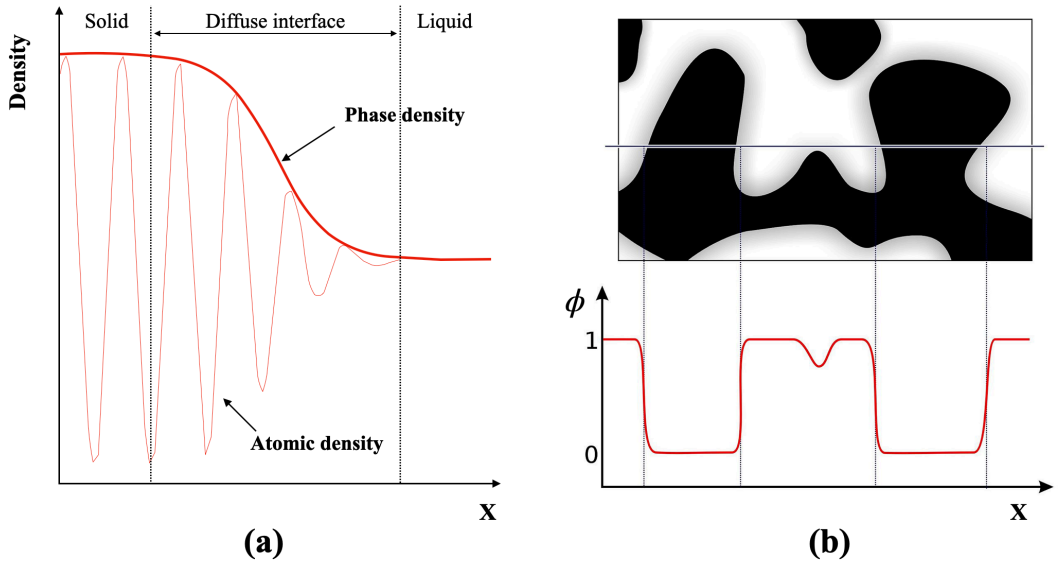

Figure 1.2: (a)Atomic density and generalized phase density near the solid-liquid interface; (b) microstructure represented by the order parameter (from Wikipedia by Cenna).

Through the development of the phase-field method in the past decades and thanks to the fast-growing computational technologies, the phase-field method has become more and more powerful in simulating a wide range of phenomena in materials science including phase transformations [39, 40] and the solid mechanics [41, 42, 43]. Valuable insights gained from simulation results provide guidance for the design and manufacturing of advanced materials [44]. In the field of solidification, the phase-field method has grown to be not only a qualitative method to elucidate the mechanisms but also a predictive tool in calculating microstructure

features [45, 46]. Both commercial [47] and open-source software [48] are available for simulating complex processes during microstructure formation. The modeling work of this dissertation is motivated by either the development of the phase-field technique for solidification processing or the application of this numerical method to elucidate the solidified microstructure of some industrially important materials that have not been fully understood through experimental and theoretical studies.

1.2 Materials of Concern

1.2.1 Directionally solidified multi-crystalline silicon

Among the materials in the solar cells industry, crystalline silicon, including mono-crystalline and multi-crystalline silicon, remains to be the dominating material with a market share of over 90% [49, 50, 51]. The cells made with multi-crystalline silicon (Fig.1.3a and b), grown by casting or directional solidification technique, have a much lower cost compared to the ones with mono-crystalline silicon, grown by Czochralski (CZ) method. However, the energy conversion efficiency of the cells with multi-crystalline silicon degrades due to the crystal defects in the polycrystalline grain structure, such as dislocations and grain boundaries [51]. Therefore, it is crucial to understand the fundamental phenomena that happen during the process of directional solidification of multi-crystalline silicon for developing advanced technology that can produce low-cost and high-efficiency solar cells. As one of the main defects, GBs are abundant in the final grain structure and their behavior during the directional solidification is hard to be understood, even with the help of in-situ-observations [50] (Fig.1.3c). Thus, the morphology and behavior of the growth front of the solid silicon can hardly be predicted through theoretical analysis and controlled by regulating cooling conditions during manufacturing.

Numerical modeling is expected to provide new insight and even predict the grain structure.

Basically, in the directional solidification of multi-crystalline silicon, multiple silicon grains, each of which has a faceted morphology and an arbitrary orientation, grow simultaneously with respect to the temperature gradient. On account of faceted morphology of a single grain, the phase field modeling of the grain structure of multi-crystalline silicon requires an accurate description of the anisotropic interface properties, including interface energy and kinetic coefficient. The simulation of single silicon grain should be verified by the result of in-situ observation prior to the simulation of multiple randomly oriented grains. The first task of the present study is to construct a phase-field model to facilitate experimental research and industrial manufacturing of silicon solidification.

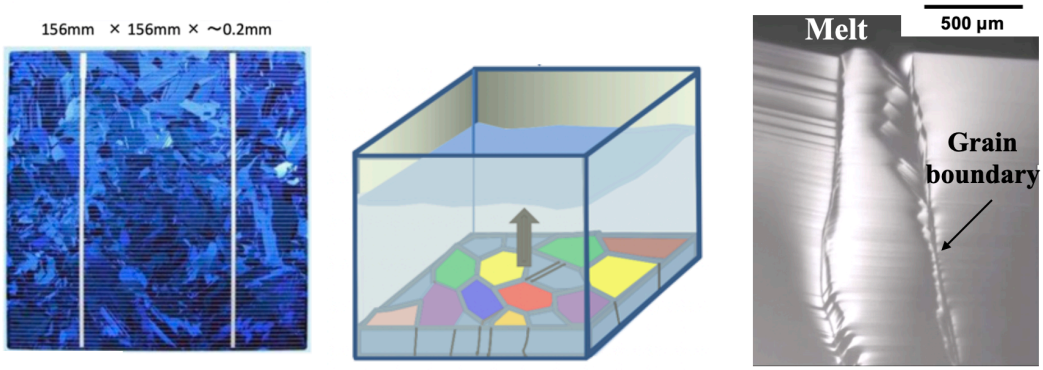

Figure 1.3: (a) polycrystalline grain structure in solar cells made by multi-crystalline silicon; (b) schematic image of the grain structure during directional growth; (c) In-situ observation of the three misoriented silicon grains with grain boundaries (Courtesy of K. Fujiwara and L. Chuang et al.).

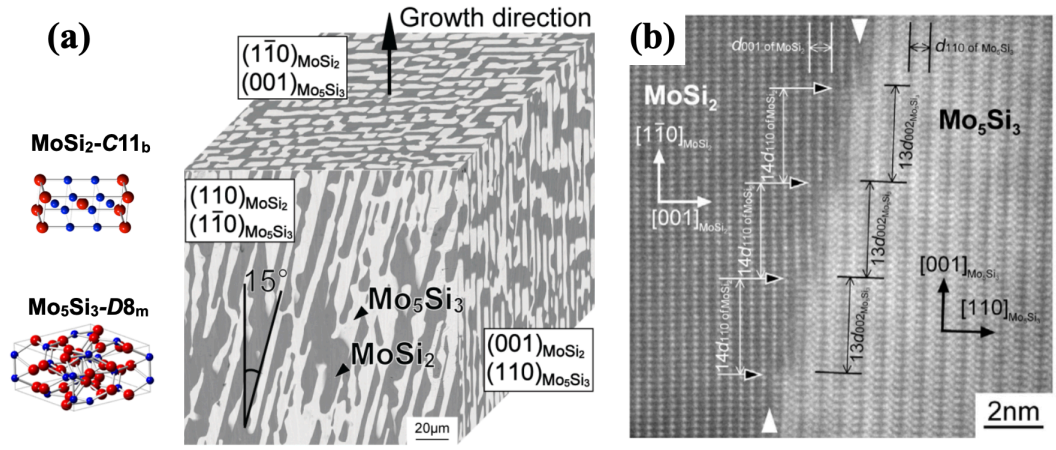

Figure 1.4: (a) Scanning electron microscope (SEM) image of the three-dimension microstructure of $MoSi_2/Mo_5Si_3$ eutectic shows the script lamellar eutectic structure. (b) Scanning transmission electron microscope (STEM) image shows the atomic arrangement and ledge-terrace structure at the interphase boundary (after K. Fujiwara et al.[52]).

1.2.2 $MoSi_2/Mo_5Si_3$ eutectic with script lamellar pattern

Facing the global issue of climate change, high-temperature materials are required for improving the conversion efficiency of heat to work and reducing carbon emissions [53, 54, 55]. The $MoSi_2/Mo_5Si_3$ eutectic alloy is one of the promising candidates that can surpass the traditional Ni-based superalloys. In order to improve the room temperature toughness, which is critical for the practical application of this new material, it is important to elucidate the formation mechanism of the eutectic structure during directional solidification [52]. As shown in (Fig.1.4a), the complex eutectic structure is the so-called script lamellar structure. The 'script' means the morphology in the horizontal cross-section has a square-like feature similar to the Chinese character. On the vertical cross-section, the white Mo_5Si_3 rods embedded in the grey $MoSi_2$ matrix appear to have a cuboidal shape. The irregularity and discontinuity of the rods are generally observed in eutectic alloys

with faceted phases, such as Al-Si alloy [8]. Thus, this unique dual-phase pattern is essentially related to the crystal structure of $MoSi_2$ and Mo_5Si_3 phases, which have C11b-type and D8m-type structures, respectively. Both of them are stoichiometric intermetallic compounds with directional covalent bonding. In Fig.1.4b, the atomic arrangement on the interphase boundary shows the ledge-and-terrace structure. The interphase boundaries tend to be aligned along the direction defined by the ledge-and-terrace structure to form inclined rods of Mo_5Si_3. With respect to the complexity of the microstructure depicted above, the second goal of the present research is to gain a deeper understanding of pattern formation during directional solidification through conducting phase-field simulations of the $MoSi_2/Mo_5Si_3$ eutectic system.

1.2.3 Rapidly solidified aluminum alloy

With the active development of additive manufacturing in recent years, the non-equilibrium microstructure during rapid solidification, which is quite different from the equilibrium one in normal casting processing, has attracted much attention [56, 57, 58, 59, 60, 61]. For most cases, the velocity of the solid-liquid interface in the melting pool can be in the range of 0.1 m/s to 10 m/s. As a result, the solute partitioning between the solid and liquid is incomplete because the time for solute redistribution at the interface is limited. The solid and liquid concentration at the moving interface can not be predicted by the equilibrium phase diagram. Consequently, the morphology of the solid-liquid interface changes with the increasing interface velocity in the following sequence: plane, cell, dendrite, cell, band, plane [62]. Fig.1.5 [1] shows the in-situ observation of the rapidly moving solid-liquid interface and the resulting microstructure of Al-4at.%Cu alloy. The

[1] Usage of the figure has been permitted by Springer Nature (License Number: 5591591323029).

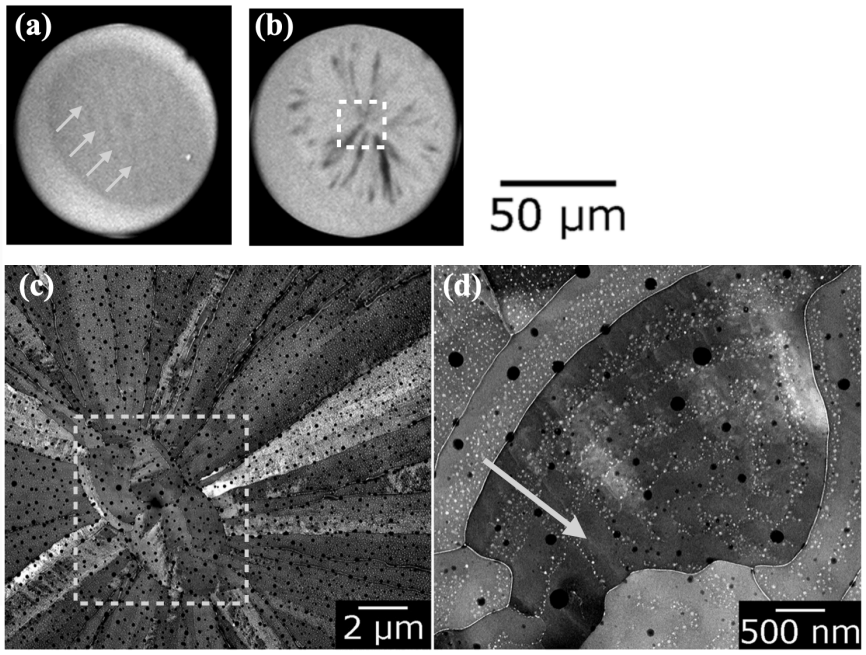

Figure 1.5: Non-equilibrium microstructure of Al-4at.%Cu alloy during (a, b) and after (c, d) laser melting processing. (a-b) In-situ observation of the melting pool. The arrow denotes the motion of the solid-liquid interface. The dashed square is magnified in (c); (c) columnar grain structure grown with a velocity between 0.20-0.84 m/s. The dashed square is magnified in (d); (d) the banded structure with alternating segregation-free and segregated Al phases. The growth velocity is about 2 m/s. The arrow denotes the growth direction. (After Joseph T. Mckeown et al. [17]. The dashed squares are added by the dissertation author for indicating the figures with smaller length scales. The square size may not be the same as the corresponding figure.)

grain structure and solute distribution in the final microstructure can hardly be analyzed or predicted according to the established theory based on the equilibrium assumption. The same challenges remain in numerical modeling. Despite the maturity of the phase-field method in solidification simulation, the coupling of the phase field to the concentration field during rapid growth remains controversial even to date [63, 64, 22]. The simulation of the high-speed interface in alloy solidification is still an unsolved issue in the industry, as the most popular software suites [47, 48] are not yet able to function well for the rapid interface. The third task in this work is to tackle the challenge of rapid solidification through phase-field modeling with the hope of accurate modeling of the non-equilibrium microstructure.

1.3 Outline of This Study

The common physical processes underlying the three solidification cases in the last section are crystallographic anisotropy and solute redistribution, as shown in the conceptual map in Fig.1.6. The following content of this thesis has been organized in the same manner. The aim of this study is to facilitate the control of the solidification microstructure of some industrially important materials through conducting phase-field simulations. The content of each chapter has been outlined below:

Chapter 2: Establishing a theoretical foundation is important for developing and applying numerical models. In the chapter, the sharp and diffuse interface models have been rigorously compared in terms of formulation, efficiency, and accuracy. In the formulation, the physical effects, such as anisotropic surface energy, solute redistribution, and crystal orientation have been incorporated. In the numerical results, it has been verified that the diffuse interface model can approximate the

Figure 1.6: Conceptual map of this study.

sharp interface model, which is regarded to be analytically correct, under appropriate numerical conditions. The understanding of the diffuse interface models will facilitate applying the model to realistic solidification cases in chapters 3 and 4. It should be noted that the numerical result of the diffuse interface is dependent on the width of the diffuse interface, which is usually enlarged to reduce computational cost. The width effect has been pointed out to justify the need for developing a numerical scheme for quantitative simulation, which is the task in Chapter 5. Lastly, the phase-field-crystal method has been introduced briefly to showcase its capability of atomic-level simulation based on the concept of diffuse interface.

Chapter 3: The anisotropy of surface properties of the silicon crystals is responsible for the formation of the gain structure of multi-crystalline silicon, which has been prevalently used in the solar cell industry. The phenomenon of the grain boundary extension remains largely unclear and a deep understanding is required to develop advanced crystal growth technology. In this chapter, the multi-phase-field model is built based on the formulation in Chapter 2. The anisotropic surface properties of faceted silicon crystal in the phase-field model have been verified by comparing to the experimental observations of both single crystal growth and grain boundary extension. The interplay between the anisotropic surface energy and anisotropic kinetic coefficient has been proven to be the key reason for various extension directions of the grain boundaries. The developed phase-field model is believed to be an accurate tool for predicting the grain structure of faceted silicon.

Chapter 4: The solidification microstructure becomes much more complex as the growing solid consists of two different phases with faceted properties. The formation mechanism of the eutectic structure of $MoSi_2/Mo_5Si_3$, which is a promising candidate for ultra-high temperature material, remains mysterious. By taking reference to the simple case of Al-Si eutectic, the instability of the solid-liquid

interface has been proposed to be the possible reason for the discontinuity of the pattern. On the other hand, the experimental observation of the atomic arrangement at the interphase boundary has revealed the ledge-terrace structure, which corresponds to the inclination of the Mo_5Si_3 rods in the $MoSi_2$ matrix. The two possible factors have been incorporated into the phase-field model through the incorporation of nucleation on the solid-liquid interface and anisotropy of the interphase boundary energy. The simulation results compared with experimental observations shed light on the formation mechanism of the complex eutectic structure.

Chapter 5: As noted in Chapter 2, the accuracy of the phase-field model is limited by the artificial width of the diffuse interface, especially when the phase field is coupled to the concentration field. Thus, in addition to the application in practical problems, the phase-filed method itself needs to be improved to be more accurate and efficient for simulating complex microstructure problems. Additionally, with the development of additive manufacturing in recent years, non-equilibrium solute partitioning becomes prominent when the solidification rate is as high as 0.1 m/s and gives rise to microstructures completely different from those in conventional casting. In the chapter, a new phase-field methodology has been proposed to achieve accuracy under both equilibrium and non-equilibrium conditions. Through the so-called middle-obstacle approach, the width effect of the diffuse interface has significantly diminished. The accurate and efficient model is expected to facilitate the understanding and control of solidification microstructure for the development of new and advanced materials.

In the concluding remark, the methodology, achievements, and implications of the present study will be briefly reviewed.

References

[1] W. D. Callister and D. G. Rethwisch, *Materials science and engineering: an introduction*, vol. 7. John wiley & sons New York, 2007. 1

[2] A. Goetzberger, C. Hebling, and H.-W. Schock, "Photovoltaic materials, history, status and outlook," *Materials science and engineering: R: Reports*, vol. 40, no. 1, pp. 1–46, 2003. 1

[3] R. C. Reed, *The superalloys: fundamentals and applications*. Cambridge university press, 2008. 1

[4] K. V. Wong and A. Hernandez, "A review of additive manufacturing," *International scholarly research notices*, vol. 2012, 2012. 1

[5] I. Gibson, D. Rosen, B. Stucker, M. Khorasani, D. Rosen, B. Stucker, and M. Khorasani, *Additive manufacturing technologies*, vol. 17. Springer, 2021. 1

[6] D. A. Porter, K. E. Easterling, and M. Y. Sherif, *Phase transformations in metals and alloys*. CRC press, 2009. 1, 2.2.1, 2.3.4, 3

[7] P. Atkins, P. W. Atkins, and J. de Paula, *Atkins' physical chemistry*. Oxford university press, 2010. 1

[8] W. Kurz and D. Fisher, *Fundamentals of solidification*. Trans Tech Publications, 1986. 1, 1.2.2, 2.2.1, 4.1, 5.1

[9] J. A. Dantzig and M. Rappaz, *Solidification*. EPFL Press, 2009. 1, 2, 2.2.1, 2.2.4, 3, 4.2.1, 5.1

[10] K. Jackson, "Solidification," *American Society for Metals: Metals Park, OH*, p. 141, 1971. 1.1, 1.1

[11] B. Caroli, C. Caroli, G. Faivre, and J. Mergy, "Lamellar eutectic growth of CBr_4-C_2Cl_6: effect of crystal anisotropy on lamellar orientations and wavelength dispersion," *Journal of crystal growth*, vol. 118, no. 1-2, pp. 135–150, 1992. 1.1, 1.1

[12] H. Chikama, H. Shibata, T. Emi, and M. Suzuki, " "in-situ" real time observation of planar to cellular and cellular to dendritic transition of crystals growing in fe–c alloy melts," *Materials Transactions*, vol. 37, no. 4, pp. 620–626, 1996. 1.1

[13] K. Fujiwara, Y. Obinata, T. Ujihara, N. Usami, G. Sazaki, and K. Nakajima, "In-situ observations of melt growth behavior of polycrystalline silicon," *Journal of Crystal Growth*, vol. 262, no. 1-4, pp. 124–129, 2004. 1.1

[14] R. H. Mathiesen, L. Arnberg, F. Mo, T. Weitkamp, and A. Snigirev, "Time resolved x-ray imaging of dendritic growth in binary alloys," *Physical Review Letters*, vol. 83, no. 24, p. 5062, 1999. 1.1

[15] A. Tandjaoui, N. Mangelinck-Noel, G. Reinhart, B. Billia, T. Lafford, and J. Baruchel, "Investigation of grain boundary grooves at the solid–liquid interface during directional solidification of multi-crystalline silicon: in situ

characterization by x-ray imaging," *Journal of crystal growth*, vol. 377, pp. 203–211, 2013. 1.1, 3.1

[16] H. Yasuda, K. Morishita, N. Nakatsuka, T. Nishimura, M. Yoshiya, A. Sugiyama, K. Uesugi, and A. Takeuchi, "Dendrite fragmentation induced by massive-like δ–γ transformation in fe–c alloys," *Nature communications*, vol. 10, no. 1, p. 3183, 2019. 1.1

[17] J. T. McKeown, K. Zweiacker, C. Liu, D. R. Coughlin, A. J. Clarke, J. K. Baldwin, J. W. Gibbs, J. D. Roehling, S. D. Imhoff, P. J. Gibbs, *et al.*, "Time-resolved in situ measurements during rapid alloy solidification: Experimental insight for additive manufacturing," *JOM*, vol. 68, pp. 985–999, 2016. 1.1, 1.5

[18] E. Van Der Giessen, P. A. Schultz, N. Bertin, V. V. Bulatov, W. Cai, G. Csányi, S. M. Foiles, M. G. Geers, C. González, M. Hütter, *et al.*, "Roadmap on multiscale materials modeling," *Modelling and Simulation in Materials Science and Engineering*, vol. 28, no. 4, p. 043001, 2020. 1.1

[19] N. Provatas and K. Elder, *Phase-field methods in materials science and engineering*. John Wiley & Sons, 2011. 1.1

[20] S. B. Biner, *Programming phase-field modeling*. Springer, 2017. 1.1

[21] M. Gururajan, "Noc:phase field modelling: the materials science, mathematics and computational aspects," 2018. 1.1, 2.1

[22] I. Steinbach, *Lectures on Phase Field*. Springer, 2023. 1.1, 1.2.3, 2.2.1, 2.2.2, 2.3.3

[23] L.-Q. Chen and Y. Zhao, "From classical thermodynamics to phase-field method," *Progress in Materials Science*, vol. 124, p. 100868, 2022. 1.1

[24] L.-Q. Chen, "Phase-field models for microstructure evolution," *Annual review of materials research*, vol. 32, no. 1, pp. 113–140, 2002. 1.1, 2

[25] S.-L. Wang, R. Sekerka, A. Wheeler, B. Murray, S. Coriell, R. Braun, and G. McFadden, "Thermodynamically-consistent phase-field models for solidification," *Physica D: Nonlinear Phenomena*, vol. 69, no. 1-2, pp. 189–200, 1993. 1.1

[26] O. Penrose and P. C. Fife, "Thermodynamically consistent models of phase-field type for the kinetic of phase transitions," *Physica D: Nonlinear Phenomena*, vol. 43, no. 1, pp. 44–62, 1990. 1.1

[27] O. Penrose and P. C. Fife, "On the relation between the standard phase-field model and a "thermodynamically consistent" phase-field model," *Physica D: Nonlinear Phenomena*, vol. 69, no. 1-2, pp. 107–113, 1993. 1.1

[28] M. Rappaz and C.-A. Gandin, "Probabilistic modelling of microstructure formation in solidification processes," *Acta metallurgica et materialia*, vol. 41, no. 2, pp. 345–360, 1993. 1.1

[29] D. Tourret and A. Karma, "Three-dimensional dendritic needle network model for alloy solidification," *Acta Materialia*, vol. 120, pp. 240–254, 2016. 1.1

[30] R. Kobayashi, "Modeling and numerical simulations of dendritic crystal growth," *Physica D: Nonlinear Phenomena*, vol. 63, no. 3-4, pp. 410–423, 1993. 1.1

[31] R. Kobayashi, "A numerical approach to three-dimensional dendritic solidification," *Experimental mathematics*, vol. 3, no. 1, pp. 59–81, 1994. 1.1

[32] T. Takaki, "Phase-field modeling and simulations of dendrite growth," *ISIJ international*, vol. 54, no. 2, pp. 437–444, 2014. 1.1, 2.2.4, 2.3.1

[33] G. Demange, H. Zapolsky, R. Patte, and M. Brunel, "A phase field model for snow crystal growth in three dimensions," *npj Computational Materials*, vol. 3, no. 1, p. 15, 2017. 1.1

[34] K. G. Libbrecht, "Physical dynamics of ice crystal growth," *Annual Review of Materials Research*, vol. 47, pp. 271–295, 2017. 1.1, 2.2.4

[35] J. W. Cahn and J. E. Hilliard, "Free energy of a nonuniform system. i. interfacial free energy," *The Journal of chemical physics*, vol. 28, no. 2, pp. 258–267, 1958. 1.1, 2.2.2

[36] J. W. Cahn, "On spinodal decomposition," *Acta metallurgica*, vol. 9, no. 9, pp. 795–801, 1961. 1.1, 2.2.3

[37] W. J. Boettinger, J. A. Warren, C. Beckermann, and A. Karma, "Phase-field simulation of solidification," *Annual review of materials research*, vol. 32, no. 1, pp. 163–194, 2002. 1.1, 2.2.3, 5.2.1, 5.2.1

[38] L. Mikheev and A. Chernov, "Mobility of a diffuse simple crystal—melt interface," *Journal of Crystal Growth*, vol. 112, no. 2-3, pp. 591–596, 1991. 1.1, 2.2.6

[39] I. Steinbach, "Phase-field models in materials science," *Modelling and simulation in materials science and engineering*, vol. 17, no. 7, p. 073001, 2009. 1.1, 2, 2.2.1, 2.2.2, 2.2.5, 3.1, 3.2.1, 3.2.3, 4.2.2, 5.2.1, 5.5

[40] D. Tourret, H. Liu, and J. LLorca, "Phase-field modeling of microstructure evolution: Recent applications, perspectives and challenges," *Progress in Materials Science*, vol. 123, p. 100810, 2022. 1.1

[41] M. Ambati, T. Gerasimov, and L. De Lorenzis, "A review on phase-field models of brittle fracture and a new fast hybrid formulation," *Computational Mechanics*, vol. 55, pp. 383–405, 2015. 1.1

[42] J.-Y. Wu, V. P. Nguyen, C. T. Nguyen, D. Sutula, S. Sinaie, and S. P. Bordas, "Phase-field modeling of fracture," *Advances in applied mechanics*, vol. 53, pp. 1–183, 2020. 1.1

[43] T. Q. Bui and X. Hu, "A review of phase-field models, fundamentals and their applications to composite laminates," *Engineering Fracture Mechanics*, vol. 248, p. 107705, 2021. 1.1

[44] Y. Zhao, "Understanding and design of metallic alloys guided by phase-field simulations," *npj Computational Materials*, vol. 9, no. 1, p. 94, 2023. 1.1

[45] L. Gránásy, L. Rátkai, A. Szállás, B. Korbuly, G. I. Tóth, L. Környei, and T. Pusztai, "Phase-field modeling of polycrystalline solidification: from needle crystals to spherulites—a review," *Metallurgical and Materials Transactions A*, vol. 45, pp. 1694–1719, 2014. 1.1

[46] W. Kurz, M. Rappaz, and R. Trivedi, "Progress in modelling solidification microstructures in metals and alloys. part ii: dendrites from 2001 to 2018," *International Materials Reviews*, vol. 66, no. 1, pp. 30–76, 2021. 1.1

[47] MICRESS©, "The microstructure evolution simulation software," 2007. 1.1, 1.2.3, 4.2.2

[48] M. Tegeler, O. Shchyglo, R. D. Kamachali, A. Monas, I. Steinbach, and G. Sutmann, "Parallel multiphase field simulations with openphase," *Computer physics communications*, vol. 215, pp. 173–187, 2017. 1.1, 1.2.3

[49] A. Polman, M. Knight, E. C. Garnett, B. Ehrler, and W. C. Sinke, "Photovoltaic materials: Present efficiencies and future challenges," *Science*, vol. 352, no. 6283, p. aad4424, 2016. 1.2.1

[50] K. Fujiwara, L.-C. Chuang, and K. Maeda, "Dynamics at crystal/melt interface during solidification of multicrystalline silicon," *High Temperature Materials and Processes*, vol. 41, no. 1, pp. 31–47, 2022. 1.2.1, 3.1, 3.2.3

[51] P. Wang, C. Cui, D. Yang, and X. Yu, "Seed-assisted growth of cast-mono silicon for photovoltaic application: challenges and strategies," *Solar Rrl*, vol. 4, no. 5, p. 1900486, 2020. 1.2.1, 3.1

[52] K. Fujiwara, H. Matsunoshita, Y. Sasai, K. Kishida, and H. Inui, "Effects of ternary additions on the microstructure and thermal stability of directionally-solidified $mosi_2/mo_5si_3$ eutectic composites," *Intermetallics*, vol. 52, pp. 72–85, 2014. 1.4, 1.2.2, 4.1, 4.4.1, 4.8, 4.4.2

[53] Y. Arai, R. Inoue, K. Goto, and Y. Kogo, "Carbon fiber reinforced ultra-high temperature ceramic matrix composites: A review," *Ceramics International*, vol. 45, no. 12, pp. 14481–14489, 2019. 1.2.2

[54] I. Akande, O. Oluwole, O. Fayomi, and O. Odunlami, "Overview of mechanical, microstructural, oxidation properties and high-temperature applications of superalloys," *Materials Today: Proceedings*, vol. 43, pp. 2222–2231, 2021. 1.2.2

[55] B. Chen and L. Zhuo, "Latest progress on refractory high entropy alloys: Composition, fabrication, post processing, performance, simulation and prospect," *International Journal of Refractory Metals and Hard Materials*, p. 105993, 2022. 1.2.2

[56] Y. Kok, X. P. Tan, P. Wang, M. Nai, N. H. Loh, E. Liu, and S. B. Tor, "Anisotropy and heterogeneity of microstructure and mechanical properties in metal additive manufacturing: A critical review," *Materials & Design*, vol. 139, pp. 565–586, 2018. 1.2.3

[57] V. Bathula, C. Liu, K. Zweiacker, J. McKeown, and J. M. Wiezorek, "Interface velocity dependent solute trapping and phase selection during rapid solidification of laser melted hypo-eutectic al-11at.% cu alloy," *Acta Materialia*, vol. 195, pp. 341–357, 2020. 1.2.3

[58] K. Karayagiz, L. Johnson, R. Seede, V. Attari, B. Zhang, X. Huang, S. Ghosh, T. Duong, I. Karaman, A. Elwany, *et al.*, "Finite interface dissipation phase field modeling of ni–nb under additive manufacturing conditions," *Acta Materialia*, vol. 185, pp. 320–339, 2020. 1.2.3

[59] D. Tourret, J. Klemm-Toole, A. E. Castellanos, B. Rodgers, G. Becker, A. Saville, B. Ellyson, C. Johnson, B. Milligan, J. Copley, *et al.*, "Morphological stability of solid-liquid interfaces under additive manufacturing conditions," *Acta Materialia*, vol. 250, p. 118858, 2023. 1.2.3

[60] M. Yang, L. Wang, and W. Yan, "Phase-field modeling of grain evolutions in additive manufacturing from nucleation, growth, to coarsening," *Npj Computational Materials*, vol. 7, no. 1, p. 56, 2021. 1.2.3

[61] A. F. Chadwick and P. W. Voorhees, "The development of grain structure during additive manufacturing," *Acta Materialia*, vol. 211, p. 116862, 2021. 1.2.3

[62] R. Trivedi and W. Kurz, "Dendritic growth," *International Materials Reviews*, vol. 39, no. 2, pp. 49–74, 1994. 1.2.3, 2.1, 5.3.1, 5.3.2

[63] T. Pinomaa and N. Provatas, "Quantitative phase field modeling of solute trapping and continuous growth kinetics in quasi-rapid solidification," *Acta Materialia*, vol. 168, pp. 167–177, 2019. 1.2.3, 5.1

[64] S. Kavousi and M. A. Zaeem, "Quantitative phase-field modeling of solute trapping in rapid solidification," *Acta Materialia*, vol. 205, p. 116562, 2021. 1.2.3, 5.1

Chapter 2

Idea of Diffuse Interface Model

All the microstructure problems in solidification can be reduced to the description of the moving solid-liquid interface. On the basis of kinetic theory, the velocity of the interface is linearly proportional to the thermodynamic driving force. The atomic nature of the interface can then be neglected and assumed to be a sharp plane without thickness. This sharp interface model is regarded as analytically correct as the interface motion is governed by the thermal and mass transport processes separated by the moving boundary. It is also well known as the free boundary problem or Stefan problem [1]. However, the idea of a smoothly transitioned interface with a finite thickness is actually more consistent with physical reality as there is always a variation of crystallographic symmetry (atomic density) across the interface between two phases. The assumption of a *diffuse interface* is also numerically efficient as the position and morphology of the interface can be implicitly obtained from the diffuse profile across the interface region rather than explicitly tracking a sharp interface without thickness [2, 3, 4].

The utilization of the concept of the diffuse interface in numerical modeling led to the advent of the *phase field method*, which nowadays has been developed to be a mature tool for simulating microstructures evolution mostly involved with long-range transport fields (concentration and temperature), anisotropy of surface

properties, and multiple misoriented grains. [5, 6]. In this chapter, the governing equation of the diffuse interface will be derived from the energy perspective in comparison with the sharp interface model from the kinetic perspective. The simulation results of the former will be compared with the analytical results of the latter to verify the conditions for obtaining correct numerical results. Last but not least, it is cost-effective in practice to choose an artificially larger width for the diffuse interface rather than the nano-scale width so that the interface width and the characteristic length of microstructures (on the micrometer scale) can be simultaneously resolved with much less computer memory. The side effect of the artificial interface width will be noted to suggest the need to develop a numerical scheme for quantitative simulation, which is the topic in Chapter 5.

2.1 Sharp and Diffuse Interface Models

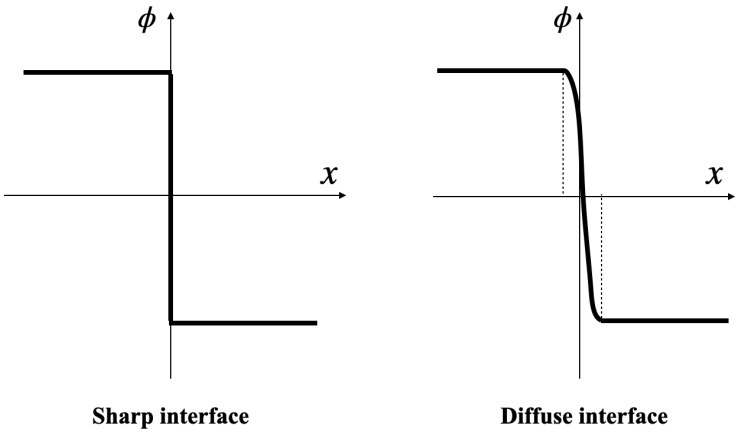

Figure 2.1: sharp (left) and diffuse (right) descriptions of the interface.

In the process of solidification, the liquid phase densifies to become the solid phase and the motion of the solid-liquid interface can be characterized by the evolution of the phase field, which is a mathematical description of the phase

density. Accordingly, there are two different assumptions for the interface between the solid and liquid phases as shown in Fig.2.1. One is the sharp interface model, in which the phase field changes abruptly at the interface and the interface has no thickness. Another one is the diffuse interface model, which exhibits a smooth transition in the interface region. Corresponding to the sharp and diffuse interface models, the governing equations of the phase field can be derived from the kinetic and energy perspectives, respectively.

From a kinetic point of view, a sharp interface is more likely to be assumed and the velocity of the interface is related to the driving force. The motion interface arises from the net flux of atoms migrating forward (solid to liquid) and backward (liquid to solid). During solidification, as the solid grows into the liquid, the number of atoms attaching to the solid is greater than the number of atoms leaving it. According to the reaction rate theory [7, 8] the interface velocity is linearly proportional to the difference in Gibbs free energy between the solid and liquid phases. Therefore, the interface velocity v is expressed by the following kinetic equation:

$$v \approx M\Delta G \tag{2.1}$$

The coefficient M is the interface mobility. The free energy difference ΔG can alternatively be expressed by the deviation from the equilibrium temperature and the entropy change for the solid-liquid phase transformation. These two quantities are known as undercooling ΔT and fusion entropy S_{f}, respectively. If the undercooling is sufficiently small, the driving force can be linearly approximated as:

$$\Delta G \approx S_{\mathrm{f}}\Delta T. \tag{2.2}$$

Considering temperature is a more convenient variable than free energy, the kinetic equation Eq.(2.1) can be re-expressed as,

$$v = \mu \Delta T \tag{2.3}$$

in which the kinetic coefficient μ contains the interface mobility and the fusion entropy. The equation above is the so-called undercooling-velocity response equation, which is widely adopted in the field of crystal growth [9].

From the energy point of view, the evolution of microstructure is accompanied by the decrease in the total free energy. Thus, the phase field ϕ should be a continuous field with the diffuse interface profile to formulate the free energy density f considering the excessive energy of the interface. The system's total free energy F has a functional expression and can be obtained by integrating local free energy density:

$$F = \int_V f[\phi(x,t)]\ dv \tag{2.4}$$

To obtain the profile of the phase field that gives rise to the minimal free energy of the non-uniform system with interface region, the derivative of the free energy functional is performed according to the Euler-Lagrange formula,

$$\psi = \frac{\delta F}{\delta \phi} = \frac{\partial f}{\partial \phi} - \nabla \frac{\partial f}{\partial \nabla \phi} \tag{2.5}$$

If the functional derivative above is non-zero, the system′s free energy is not minimal. The evolution of the phase field is then hypothetically governed by the time-dependent equation with the following dissipative form:

$$\frac{\partial \phi}{\partial t} = -L\psi \tag{2.6}$$

in which L is the dissipation coefficient and the functional derivative ψ is the generalized driving force. The equation is also called Allen-Cahn equation that describes the order-disorder phase transformation [10, 11].

The two types of governing equations Eq.(2.3) and Eq.(2.6) from different perspectives share a similar mathematical form. They express the rate of change to be linearly proportional to the driving force by a coefficient, which is assumed to be a constant material property for now. The rate of change of phase field in Eq.(2.6) corresponds to the rate of change of interface location in Eq.(2.3). The functional derivative in Eq.(2.6) acts as the role of the undercooling in Eq.(2.3). The distinct feature of the kinetic equation is that the quantities (v, ΔT) are measurable in experiments and more relevant to the microstructure evolution on the micrometer scale. Additionally, the interface motion during the solid-liquid transformation is accompanied by a series of physical processes, such as thermal, chemical, and curvature effects, which contribute to the driving force in the governing equations. Thus, it seems more convenient to incorporate these effects into the equation of the kinetic perspective. However, it is challenging to solve the sharp interface model analytically or numerically because interface tracking is required. In contrast, the equation derived from the energy perspective, which retains the idea of a diffuse interface, is much easier to be solved through numerical methods because the location of the interface can be implicitly obtained from the spatial derivative of the diffuse profile.

The so-called phase-field method adopts the idea of the diffuse interface model. In order to develop the numerically efficient and analytically correct model for solidification, the mathematical formulation can be started from the kinetic perspective, which can easily incorporate multiple physics effects. The corresponding phase field model can then be correlated to its sharp interface counterpart and solved by numerical methods to obtain the solution of the moving interface.

2.2 Formulation

The content of this section has been organized as follows: (I) The free boundary problem, which is the sharp interface model involved with solute transport and curvature effect, has been elaborated to lay the physical foundation for pattern formation in solidification; (II) the parameters in the energy-based phase-field model has been related to the physical parameters in the kinetic-based sharp interface model; (III) the anisotropic interface energy, which is responsible for preferential growth of the crystal in the solidification, has been incorporated into the phase-field model; (IV) the phase field equation has been coupled with the diffusion equation to demonstrate the solidification of binary alloys; (V) a more practical multi-phase-field method has been presented to showcase its capability of modeling multiple independent grains with arbitrary orientations; (VI) the phase-field-crystal method, which can describe the interface on the atomic length scale, has been briefly introduced.

2.2.1 Free boundary problem

The growth of a solid in a liquid is always accompanied by the transport of heat or solute released from the growth front. In a dilute binary alloy system, in which the second element has limited solubility in the primary element, the liquidus of the equilibrium phase diagram of the alloy system denotes the freezing point of the liquid. As a result, the undercooling for the transformation of the primary solid in the liquid can be linearly approximated [12] by:

$$\Delta T = T_{\mathrm{m}} + m_{\mathrm{L}} c_{i\mathrm{L}} - T \tag{2.7}$$

in which $c_{i\mathrm{L}}$ is the solute (second element) concentration at the interface on the liquid side and the coefficient m_{L} corresponds to the negative slope of the liquidus

in the linearized phase diagram (Fig.2.2).

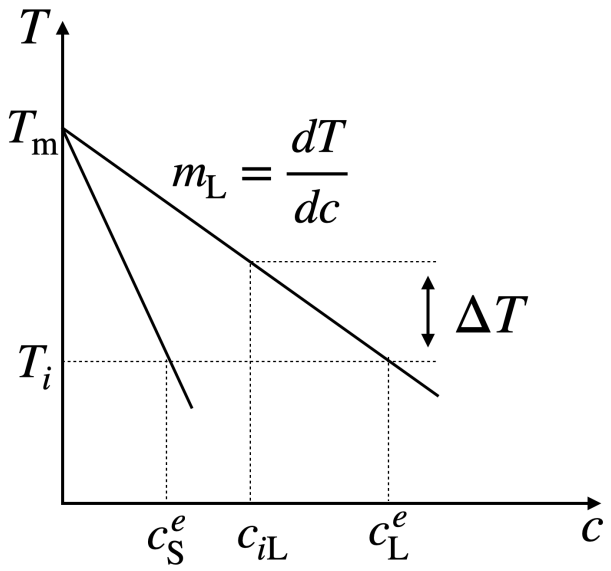

Figure 2.2: Linear approximation of the interface undercooling in the dilute binary alloy system.

Due to the limited solubility of the solute in the solid phase, the concentration of the newly formed solid is lower than that of its previous liquid state. The motion of the solid-liquid interface is accompanied by the rejection of solute into the liquid, resulting in the buildup of the diffusion layer ahead of the interface. The mass conservation of the solute atoms at the moving interface is expressed by:

$$v(c_{i\mathrm{L}} - c_{i\mathrm{S}}) = -D_{\mathrm{L}} \frac{\partial c_{i\mathrm{L}}}{\partial x} \tag{2.8}$$

The left-hand side of Eq.(2.8) represents the flux of rejected solute, while the right-hand side represents the flux of transported solute in the liquid. The solute diffusion in the solid has been neglected considering the much lower diffusion coefficient in the ordered solid phase.

The process of solute rejection is related to the solute partitioning between the solid and liquid phases. The partition coefficient characterizes the ratio of solid to liquid concentrations and remains constant within a range of temperatures for the linearized phase diagram. The coexisting solid and liquid in a domain can attain equilibrium concentrations according to the phase diagram if sufficient time is given and the solidification rate is extremely low. However, in a realistic solidification process, the time for solute transport is often limited when the interface moves at a finite speed in regular solidification processing, resulting in an inhomogeneous solute distribution in the bulk phases. Thus, only local equilibrium within the interface can be assumed [13]. Consequently, the concentrations of solid and liquid on the two sides of a steady-state moving interface have the following relation:

$$k_{\mathrm{e}} = \frac{c^{e}_{i\mathrm{S}}}{c^{e}_{i\mathrm{L}}} \tag{2.9}$$

in which the letter "e" in the variables refers to the equilibrium partitioning at the steady-state interface. The resulting one-dimensional (1D) concentration profile is depicted in Fig.2.3. At the steady state, the liquid concentration almost rests on the liquidus and the driving force that drives the motion of the 1D planar interface arises from the deviation from the liquidus owing to the solute diffusion in the liquid. As a result, the motion of the interface is controlled by the solute diffusion in the bulk liquid ahead of the interface, which is governed by the following one-sided diffusion equation if the solute diffusion in the solid is neglected.

$$\frac{\partial c_{\mathrm{L}}}{\partial t} = \nabla(D_{\mathrm{L}} \nabla c_{\mathrm{L}}) \tag{2.10}$$

For the motion of a curved solid-liquid interface, in addition to the undercooling that drives the growth of the solid, a pressure in the concave direction that

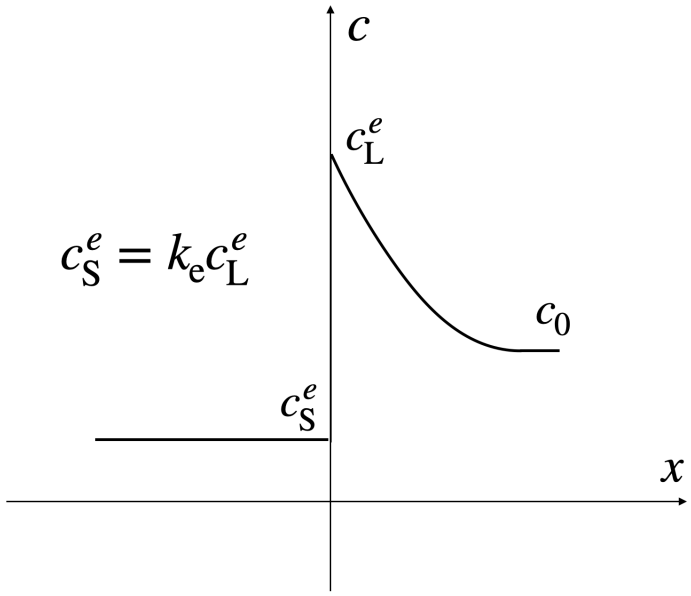

Figure 2.3: Schematic one-dimensional (1D) steady-state concentration profile near the interface during the solidification of a binary alloy. Note the equilibrium values of concentrations on the two sides of the interface. The motion of the interface is controlled by the diffusion process in the liquid.

counters the growth of the solid must be included in kinetic equation Eq.(2.3). The pressure is described by the Gibbs-Thomson effect [7] and is generated by surface tension, which arises from the imbalanced attraction between atoms with dangling bonds on the curved surface. While the resulting pressure is non-zero for a curved surface, it is zero for the planar surface since the anti-parallel surface tensions cancel each other. As undercooling with the unit of temperature is taken as the driving force in Eq.(2.3), the surface pressure is not restricted to be a Newtonian force and can be a thermodynamic force with the unit of temperature. As depicted in Fig.2.4, the tangential arrows represent the surface tension, which is characterized by the Gibbs-Thomson coefficient Γ. If the arc length is infinitesimal, the pressure P caused by the surface tensions Γ equals to:

$$P = \frac{\Gamma}{R} = \Gamma\kappa \tag{2.11}$$

in which the reciprocal of the radius, also known as the curvature κ, characterizes the shape of the curved surface. As a result, Eq.(2.3) can be expanded to incorporate the surface pressure. It has the following form:

$$\boxed{v = \mu(\Delta T - \Gamma\kappa)} \tag{2.12}$$

which is the kinetic equation that describes the interface velocity driven by both bulk and interfacial undercooling [14]. This relation is the so-called "Gibbs-Thomson equation" in phase field modeling [4, 6, 15]. Originally, the Gibbs-Thomson equation formulates only the interfacial undercooling caused by the surface pressure[1, 7]. Instead of the geometrical approach considering the surface pressure above, the interface effect on the surface undercooling can also be derived through an energetic approach considering the departure from the thermodynamic equilibrium caused by excessive energy of the surface [1].

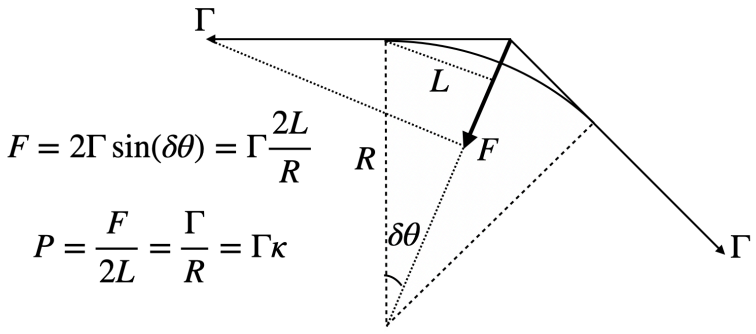

Figure 2.4: Surface pressure caused by surface tensions.

The set of equations (Eq.(2.7-2.12)) that describe the sharp interface motion and the solute redistribution constitute the so-called free boundary problem, which

is the sharp interface model and can hardly be solved analytically despite its firm physical ground. The remaining work is to relate this sharp interface model to the numerically efficient diffuse interface model.

2.2.2 Correlation of diffuse and sharp interface models

The following example[1] illustrates the relationship between the equations of the diffuse and sharp interface models. In the diffuse interface model, the free energy density is expressed as a function of the phase field in the following form,

$$f = h(\phi)G_{\mathrm{S}} + [1 - h(\phi)]G_{\mathrm{L}} + \frac{1}{2}\epsilon|\nabla\phi|^2 + \frac{1}{2}\omega\phi(1-\phi) \tag{2.13}$$

The first two terms constitute the weighted free energy density of the bulk solid and liquid through the interpolation function of $h(\phi)$, which should vary from 1 to 0 from solid to liquid. The excessive energy due to the structural variation across the interface is formulated by the gradient (third) and the quadratic (fourth) terms. Note the quadratic term has two minima when ϕ equals 1 and 0. Instead of having a double-well form as in [17], a double-obstacle originally proposed by I. Steinbach [6] is used here. Through Eq.(2.5), the functional derivative that acts as the driving force in the dissipative equation (Eq.(2.14)) is given as:

$$\psi = -h'(\phi)(G_{\mathrm{L}} - G_{\mathrm{S}}) - \epsilon\nabla^2\phi + w(\frac{1}{2} - \phi) \tag{2.14}$$

The governing equation of the phase field is given as:

$$\frac{1}{L}\frac{\partial\phi}{\partial t} = \epsilon\nabla^2\phi + w(\phi - \frac{1}{2}) + h'(\phi)(G_{\mathrm{L}} - G_{\mathrm{S}}) \tag{2.15}$$

The first two terms on the right-hand side of the equation above are the

[1] The original derivation comes from the manual in the openphase package [16].

diffusion and reaction terms leading to the formation of a diffuse interface profile [18]. The third term is the free energy difference between the solid and liquid that drives the interface motion. For the case of a stationary interface in one dimension, the free energy difference is zero and the governing equation is reduced to be

$$\epsilon\nabla^2\phi + w(\phi - \frac{1}{2}) = 0 \tag{2.16}$$

The stationary solution can be found to have a diffuse profile, which is expressed as:

$$\phi(x,t) = \frac{1}{2} - \frac{1}{2}\sin\frac{\pi}{\eta}x, -\frac{\eta}{2} \leq x \leq \frac{\eta}{2} \tag{2.17}$$

of which the width of the diffuse region is η. The phase field out of the range of the diffuse region keeps constant and has values of 1 and 0 in the solid and liquid phases, respectively. It can be examined that the spatial derivatives of the solution can be related to the solution itself,

$$\frac{\partial\phi}{\partial x} = \frac{\pi}{\eta}\sqrt{\phi(1-\phi)} \tag{2.18}$$

$$\frac{\partial^2\phi}{\partial x^2} = \frac{\pi^2}{\eta^2}(\frac{1}{2} - \phi) \tag{2.19}$$

By substituting the laplacian term in Eq.(2.16) with Eq.(2.19), the interface width can be related to the parameters ϵ and ω by,

$$\eta = \pi\sqrt{\frac{\epsilon}{\omega}} \tag{2.20}$$

The interface energy σ is the excess energy caused by the structural variation across the interface. It can be written by the integration of the free energy density across the interface when the difference of the bulk free energy is zero:

$$\begin{aligned}\gamma &= \int \left[\frac{1}{2}\epsilon|\nabla\phi|^2 + \frac{1}{2}\omega\phi(1-\phi)\right]dx \\ &= \omega\int \phi(1-\phi)dx \\ &= \frac{\omega}{8}\int_{-\eta/2}^{\eta/2}[1+\cos(\frac{2\pi}{\eta}x)]dx \\ &= \frac{\omega\eta}{8}\end{aligned} \tag{2.21}$$

The Gibbs-Thomson coefficient is given as the ratio of the interface energy to the fusion entropy:

$$\Gamma = \frac{\gamma}{\Delta S} = \frac{\omega\eta}{8\Delta S} \tag{2.22}$$

If the interface is moving, the free energy difference should be non-zero. Assuming the moving interface has the same profile as the stationary profile in Eq.(2.17), the first two terms of the governing equation Eq.(2.15)) can be truncated and it becomes,

$$\frac{1}{L}\frac{\partial\phi}{\partial t} = h'(\phi)(G_{\mathrm{L}} - G_{\mathrm{S}}) \tag{2.23}$$

The solution of the moving interface is shifted from its initial position by the traveled distance and becomes:

$$\phi(x,t) = \frac{1}{2} - \frac{1}{2}\sin\frac{\pi}{\eta}(x-vt), -\frac{\eta}{2} + vt \le x \le \frac{\eta}{2} + vt \tag{2.24}$$

The temporal derivative of the solution is:

$$\frac{\partial\phi}{\partial t} = v\frac{\partial\phi}{\partial x} \tag{2.25}$$

Consequently, the governing equation Eq.(2.23) becomes

$$v\frac{\partial\phi}{\partial x} = Lh'(\phi)(G_{\mathrm{L}} - G_{\mathrm{S}}) \tag{2.26}$$

It is clear that the equation above can be an equivalent of the equation from the kinetic perspective (Eq.(2.1)) if the spatial derivative $\partial\phi/\partial x$ (Eq.(2.18)) on the left-hand-side can be canceled by $h'(\phi)$ on the right-hand side. By choosing an interpolation function with the following form [15],

$$h(\phi) = \frac{1}{\pi}\left[(4\phi - 2)\sqrt{\phi(1-\phi)} + \arcsin(2\phi - 1)\right] + \frac{1}{2} \tag{2.27}$$

of which the derivative to ϕ is

$$h'(\phi) = \frac{8}{\pi}\sqrt{\phi(1-\phi)} \tag{2.28}$$

Consequently, Eq.(2.26) is reduced to have the kinetic form of the sharp interface model,

$$v = \frac{8\eta L}{\pi^2}(G_{\mathrm{L}} - G_{\mathrm{S}}) = \frac{8\eta L\Delta S}{\pi^2}\Delta T \tag{2.29}$$

The kinetic coefficient μ can then be related to the dissipation coefficient L,

$$\mu = \frac{8\eta\Delta S}{\pi^2}L \tag{2.30}$$

With the relations (Eq.(2.20, 2.21, 2.30)) derived above, the parameters in the dissipative equation can all be replaced by the physical parameters of the kinetic equation. It then becomes,

$$\boxed{\frac{\partial\phi}{\partial t} = \mu\left\{\Gamma\left[\nabla^2\phi + \frac{\pi^2}{\eta^2}\left(\phi - \frac{1}{2}\right)\right] + \frac{\pi\sqrt{\phi(1-\phi)}}{\eta}\Delta T\right\}} \tag{2.31}$$

The phase-field equation above is derived from the minimization of the total

free energy but correlated with the physical parameters of the kinetic equation. In a more concise way, the curvature and velocity of the diffuse interface can be directly determined from the diffuse profile of the phase field, which is known as the geometrical approach proposed by C. Beckermann [14]. The curvature of the local surface can be expressed by the divergence of the normal vector of the local surface:

$$\kappa = \nabla \cdot \left(- \frac{\nabla \phi}{|\nabla \phi|} \right) \tag{2.32}$$

In the context of fluid flow, the divergence of the fluid velocity characterizes the expanding rate of the local flux. Analogously, the divergence of a vector with unit length characterizes the expanding rate of the surface area, which is consistent with the definition of curvature in Eq.(2.11) and Fig.2.4. In a similar geometric way (Fig.2.5), the velocity of the diffuse interface can be implicitly determined through spatial and temporal derivatives of the continuous phase field:

$$v = \frac{1}{|\nabla \phi|} \frac{\partial \phi}{\partial t} \tag{2.33}$$

By replacing the interface velocity and surface curvature in Eq.(2.12), the kinetic equation can be rewritten as:

$$\frac{1}{|\nabla \phi|} \frac{\partial \phi}{\partial t} = \mu \left[\Delta T - \Gamma \nabla \cdot \left(- \frac{\nabla \phi}{|\nabla \phi|} \right) \right] \tag{2.34}$$

With the solution of the traveling diffuse profile in Eq.(2.24), Eq.(2.34) can be expanded and turn out to be identical to Eq.(2.31). It suggests that the kinetic and dissipative equations are essentially related. The resulting phase-field equation is firmly founded on the fundamental kinetic and thermodynamic principles. As long as the physical parameters are known, the diffuse interface model can be easily implemented through numerical techniques, such as the finite

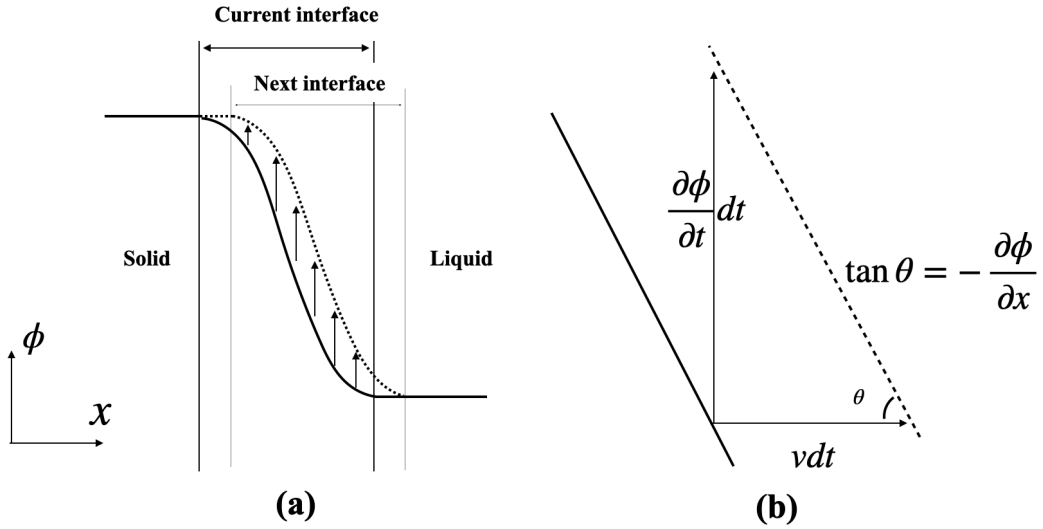

Figure 2.5: Derive the velocity of the interface from the local change of order parameter.

difference method, to quantitatively simulate interface morphology in two- or three-dimensional space. As Eq.(2.34 and 2.31) represent the simplest case of pure substance under isothermal condition, the coupling of heat or solute transport will be specified in the next step.

2.2.3 Coupling with concentration field

When the phase field is coupled with the concentration field, the model can be expected to describe alloy solidification, which is a great concern in the field of metallurgy and motivated the development of alloy phase field models by early pioneers [19, 20, 21, 22]. In the free boundary problem (Sec.2.2.1), the solute atoms are rejected by the growing solid and accumulate ahead of the solid front, the steady state of the moving interface should be controlled by the solute diffusion in the bulk liquid. The redistribution of solute element during solidification is governed by two processes: one is the solute partitioning between the coexisting

solid and liquid within the interface; the other is the solute diffusion in the bulk solid and liquid phases. In the conventional alloy phase-field model, the governing equation that describes these two processes is derived from the variational derivative of the free energy functional. The classic example is the Cahn-Hilliard equation [23] for spinodal decomposition. In the present study, the equations that govern the solute redistribution are derived from a non-variational approach, in which the solute partitioning and diffusion are implemented consecutively and separately after the local phase fraction (indicated by the phase field) is updated by the phase-field equation.

The solute partitioning happens just after the change of the local phase fractions. The total amount of the local solute is conserved and it can be expressed by,

$$c = (1 - \phi)c_{\mathrm{L}} + \phi c_{\mathrm{S}} \tag{2.35}$$

Knowing the updated phase field ϕ and the conserved concentration c, the liquid concentration c_{L} can be calculated if its relation with c_{S} is known. Conventionally, this relation is obtained by assuming equilibrium within the interface, which can be realized by two main approaches. One of them is the equality of the chemical potential [22] according to the common tangent construction on the free energy landscape, and another one is the ratio of the solid to liquid concentrations [14, 24] that can be directly found on the equilibrium phase diagram. To some degree, both of them retains the thermodynamic process during the solute redistribution between the solid and liquid phase.

In this chapter, the solid and liquid concentrations in the interface are determined by fixing the solid concentration in the interface on the solidus of the phase diagram for simplicity at the initial stage (A more realistic calculation of

the solute partitioning will be discussed in Chapter 5). As a result, the liquid concentration in the interface is then obtained by subtracting the solute in the solid from the total amount of local solute according to solute conservation. They are expressed as,

$$c_{\mathrm{S}}^{i} = c_{\mathrm{Se}} \tag{2.36}$$

$$c_{\mathrm{L}}^{i} = \frac{c - \phi c_{\mathrm{Se}}}{1 - \phi} \tag{2.37}$$

This approach emulates the solute rejection process during the solute partitioning by assuming the solid always holds the equilibrium concentration. The liquid concentration deviates from the liquidus until the realization of the steady state when there is a balance between the rejected and transported solutes in the liquid ahead of the interface.

As for the solute diffusion in the bulk phases, governing equation of the concentration field should have a conserved form rather than the dissipation form. It is expressed as,

$$\frac{\partial c}{\partial t} = \nabla(-J) \tag{2.38}$$

in which J is the flux of solute. Following Fick′s first law, the flux should be proportional to the gradient of concentration and have a coefficient named diffusivity. Because the liquid or solid phase fractions are less than 1 in the interface, the flux in the interface should be weighted by the local phase fractions. If only the solute diffusion in the liquid phase is considered, the flux is then written as,

$$J = -(1 - \phi) D_{\mathrm{L}} \nabla c_{\mathrm{L}} \tag{2.39}$$

The governing equation of solute diffusion is expanded to be,

$$\frac{\partial c}{\partial t} = \nabla\big[(1-\phi)D_{\mathrm{L}}\nabla c_{\mathrm{L}})\big] = D_{\mathrm{L}}\big[-\nabla\phi\nabla c_{\mathrm{L}} + (1-\phi)\nabla^2 c_{\mathrm{L}}\big] \tag{2.40}$$

As a result of phase change→solute partitioning→solute diffusion, the steady state similar to Fig.2.3 in the sharp interface model can be realized in the diffuse interface model. Unlike the sharp interface model (Eq.(2.7-2.12)), in which the solute redistribution is realized by tracking the motion of the sharp interface, the solute redistribution process described by Eq.(2.37, 2.40) can be easily coupled to the phase-field equation (Eq.(2.31)).

2.2.4 Anisotropic interface properties

In addition to the thermal effect, the solidification of crystalline solid is involved with the anisotropic interface properties [25], which are responsible for the formation of complex morphologies, such as dendritic [26, 27] and faceted growth [28, 29]. The pressure caused by the curved surface is not only related to the surface shape (curvature) and also to the surface energy, which is anisotropic and dependent on the crystallographic orientation. For anisotropic interface energy, the interfacial term in the kinetic equation should be modified as:

$$v = \frac{\mu}{\Delta S}(\Delta g - \gamma^*\kappa) \tag{2.41}$$

γ^* is the so-called surface stiffness [1], and $\gamma^*\kappa$ is the modified pressure when the surface energy varies with the orientation. Under the isothermal condition, the surface in the direction with smaller stiffness tends to grow faster. For the cubic symmetry in two dimensions, the surface energy and stiffness are given by the following expressions,

$$\gamma = \gamma_0(1 + \epsilon \cos\theta) \tag{2.42}$$

$$\gamma^* = \gamma + \gamma'' = \gamma_0(1 - 15\epsilon \cos 4\theta) \tag{2.43}$$

For crystals with ordered atomic structures, the surface of the close-packed plane is atomically smooth, of which the growth is quite different from that of the atomically rough surface. As a result, the kinetic coefficient is also orientation-dependent and should be taken as a function of the orientation angle in numerical simulation.

2.2.5 Multi-phase-field model

In practice, the solidification process mostly involves multiple grains with arbitrary crystallographic orientations. The preferential growth direction of each grain is independent of the other. In the previous diffuse interface model, only one phase field and one solid grain are included in the whole domain. The incorporation of multiple grains takes multiple phase fields that can represent grains with independent surface properties and orientations [30, 31, 32]. The formulation of the phase-field model that can incorporate multiple phase fields has been reviewed as follows.

The primary restriction for these phase fields is that their local sum should be unity,

$$\sum_{i=1}^{N} \phi_i = 1 \tag{2.44}$$

in which N is the local number of phase fields. Accordingly, in addition to the bulk free energy density, which is weighted by the bulk free energy density G_i of

each phase field according to its local phase fraction ϕ_i, the interface formed by two adjacent phases ϕ_i and ϕ_j contributes to local free energy density f. It can be written as,

$$f = \sum_{i=1}^{N} h(\phi_i) G_i + \sum_{i=1}^{N} \sum_{j=1}^{N} \left(\frac{1}{2} \epsilon_{ij} \nabla \phi_i \nabla \phi_j + \frac{1}{2} \omega_{ij} \phi_i \phi_j \right) \tag{2.45}$$

The functional derivative for each phase is given as,

$$\begin{aligned} \frac{\delta F}{\delta \phi_i} &= \frac{\partial f}{\partial \phi_i} - \nabla \frac{\partial f}{\partial \nabla \phi_i} \\ &= h'(\phi_i) G_i + \sum_{k=1}^{N} \left(\frac{1}{2} \epsilon_{ik} \nabla^2 \phi_k + \frac{1}{2} \omega_{ik} \phi_k \right) \end{aligned} \tag{2.46}$$

The evolution of each phase is driven by the locally superimposed functional derivatives. The change of one phase is accompanied by the inverse change of the counter phase. Accordingly, the governing equation has the form of

$$\frac{\delta F}{\delta \phi_i} = -L_{ij} \frac{2}{N} \sum_{j=1}^{N} \left(\frac{\delta F}{\delta \phi_i} - \frac{\delta F}{\delta \phi_j} \right) \tag{2.47}$$

The factor of 2 in the numerator is added for consistency with two-phase change, in which the phase number N at the interface is 2. The governing equation of multiple phases can be expanded as,

$$\begin{aligned} \frac{\delta F}{\delta \phi_i} = &- L_{ij} \frac{2}{N} \sum_{j=1}^{N} \left\{ \sum_{k=1}^{N} \left[\frac{1}{2} (\epsilon_{ik} - \epsilon_{jk}) \nabla^2 \phi_k + \frac{1}{2} (\omega_{ik} - \omega_{jk}) \ \phi_k \right] \right. \\ &\left. + h'(\phi_i) G_i - h'(\phi_j) G_j \right\} \end{aligned} \tag{2.48}$$

In the case of two-phase change, the interpolation function ahead of the $G_{i/j}$ can be taken as the one in Eq.(2.27). However, it is hardly possible to find such an

interpolation function for the multi-phase junction [6]. Conventionally, the terms of the free energy difference in the multi-phase-field model resign from the full consistency of thermodynamics at the places where the phase number is greater than two. The equation turns out to be:

$$\begin{aligned}\frac{\delta F}{\delta \phi_i} = &- L_{ij}\frac{2}{N}\sum_{j=1}^{N}\left\{\sum_{k=1}^{N}\left[\frac{1}{2}(\epsilon_{ik}-\epsilon_{jk})\nabla^2\phi_k + \frac{1}{2}(\omega_{ik}-\omega_{jk})\ \phi_k\right]\right. \\ &\left. + \frac{8}{\pi}\sqrt{\phi_i\phi_j}(G_i - G_j)\right\}\end{aligned} \tag{2.49}$$

The interface properties in the multi-phase-field model are expressed by the interaction of phase pairs. They can be expressed by the following matrix form,

$$L_{ij} = \begin{bmatrix} L_{00} & L_{01} & L_{02} \\ - & L_{11} & L_{12} \\ - & - & L_{22} \end{bmatrix} \tag{2.50}$$

$$\epsilon_{ij} = \begin{bmatrix} \epsilon_{00} & \epsilon_{01} & \epsilon_{02} \\ - & \epsilon_{11} & \epsilon_{12} \\ - & - & \epsilon_{22} \end{bmatrix} \tag{2.51}$$

If the interface energy is anisotropic, the ϵ coefficient is taken to be anisotropic [25] and set as a function of the orientation of the interface normal. Thus, the $\epsilon_{ij}^2\nabla^2\phi_j$ terms are replaced by the following expression,

$$\begin{aligned}\epsilon_{ij}^2\nabla^2\phi_j \rightarrow \nabla(\epsilon_{ij}^2\nabla\phi_j) &+ \frac{\partial}{\partial x}(\epsilon_{ij}\frac{\partial\epsilon_{ij}}{\partial(\frac{\partial\phi}{\partial x})}|\nabla\phi|^2) \\ &+ \frac{\partial}{\partial y}(\epsilon_{ij}\frac{\partial\epsilon_{ij}}{\partial(\frac{\partial\phi}{\partial y})}|\nabla\phi|^2) \\ &+ \frac{\partial}{\partial z}(\epsilon_{ij}\frac{\partial\epsilon_{ij}}{\partial(\frac{\partial\phi}{\partial z})}|\nabla\phi|^2)\end{aligned} \tag{2.52}$$

For deriving the diffusion equation for multiple phases, the multi-phase system can be regarded as a mixture of multiple phases [33, 34, 35, 36]. In the bulk phase, the number of phases is 1, whereas in the interfaces or triple junctions the number of phases is 2 or 3. It can be assumed that the diffusion flux is governed by Fick′s first law, which takes the gradient of concentration as the driving term. The total flux for a local position is the summation of contributions from coexisting phases, which can be given as,

$$J = -\sum_{i=1}^{N} D_i(\phi_i \nabla c_i) \tag{2.53}$$

The order parameter ϕ_i is the local fraction of phase i, ∇c_i is the concentration gradient in phase i, D_i is the diffusion coefficient in phase i. The diffusion equation for the multi-phase system can be simply given as

$$\frac{\partial c}{\partial t} = \nabla\left(\sum_{i=1}^{N} \phi_i D_i \nabla c_i\right) \tag{2.54}$$

2.2.6 Phase-field-crystal model

In the above-mentioned diffuse interface model, the anisotropic properties of the solid-liquid interface are incorporated by the orientation-dependent function because of the neglect of the atomic description of the interface, which can only be achieved by discrete methods, such as Molecular Dynamics and Monte Carlo method. The so-called Phase-field-crystal (PFC) method [37] has its appealing feature in describing phase transformation phenomena, such as solidification and precipitation, on the atomic length scale and diffusive time scale, filling the gap between the Molecular Dynamic (MD) method and conventional Phase Field (PF) method [38, 39]. It is expected that deeper insights can be drawn out of the simulation result via this unique modeling approach.

In PFC model, the free energy functional is written in the following form,

$$F = \int \left[\epsilon \frac{\phi^2}{2} + \frac{\phi^4}{4} + \frac{\phi}{2}(q_0^2 + \nabla^2)^2 \phi \right] d\vec{r} \tag{2.55}$$

which is called Swift-Hohenberg free energy. It can also be derived through the simplification of the Classical Density Functional Theory (CDFT) [40]. The equilibrium order parameter profile for this free energy functional has the feature of a periodic wave [41], being able to represent the symmetry of the crystal lattices, such as hexagon (or triangle) in 2D and BCC in 3D. The one-mode density wave approximation of hexagonal lattice in two dimensional space is written by

$$n = n_0 - A_1 \cos(q_0 x) \cos(q_0 y/\sqrt{3}) + A_1 \cos(2q_0 y/\sqrt{3}) \tag{2.56}$$

The parameters n_0 is the average density and A_1 is the amplitude of the periodic wave. The parameter ϵ in Eq.2.55 can be regarded as the characteristic temperature and is related to the stability of equilibrium density. The coefficient q_0 has an inverse relation to the planar distance $a_{hex_{10}}$ of the hexagonal lattice structure

$$q_0 = \frac{2\pi}{a_{hex10}} \tag{2.57}$$

The original model above demonstrates the key features of the PFC methodology but has its limitation in producing realistic phase diagrams and stabilizing a variety of crystallographic structures. Based on the original formulation, the free energy functional in XPFC (structural phase field crystal [42]) has been derived as,

$$F = \int \left\{ \frac{1}{2} n^2 - \frac{\eta}{6} n^3 + \frac{\chi}{12} n^4 - \frac{1}{2} n \int [C^2(r - r')n] dr' \right\} dr \tag{2.58}$$

The fourth-order polynomial in the integrand represents the entropy part of the

free energy which increases with the amplification of the wave amplitude. The other term characterizes the enthalpy part of the free energy and varies in an opposite way to the entropy part as the wave density profile emerges from the uniform density. As a result of the balance between these two parts of free energy, the density wave corresponding to a specific lattice structure can be stabilized. The advantage of XPFC formulation is that the desired crystal symmetry and properties can be obtained by customizing the features of the two-point correlation function $C^2(r - r')$, making it possible to realistically simulate structural phase transformation between different lattices which is prevalent during the thermal and mechanical processing of engineering alloy materials.

Starting with the density approximation of the desired lattice structure, while the one mode expansion (Eq.(2.56)) is sufficient for triangle lattice, two modes are required for approximating the square lattice, which consists of two primary lattice planes,

$$n = n_0 + 2A_1[\cos(q_0 y) + \cos(q_0 x)] + 4A_2 \cos(q_0 x)\cos(q_0 y) \tag{2.59}$$

Consequently, this expression shows that two amplitude parameters A_1 and A_2 modulate the wave density profile. Then, the correlation function needs to be specified corresponding to the approximation density. In the Fourier space, the correlation function is comprised of multiple peaks which can be approximated by the summation of Gaussian distributions,

$$c_2(k) = \sum_i \exp\left[-\frac{(\sigma/\sigma_i)^2 k_i^2}{2\rho_i\beta_i}\right] \exp\left[-\frac{(k-k_i)^2}{2\alpha_i^2}\right] \tag{2.60}$$

The peak i corresponds to the lattice plane distanced by the value of k_i in the Fourier space. Although there is actually an infinite number of lattice planes in a crystal lattice, only the peaks for primary planes of the lattice should be consid-

ered for being consistent with the modes in the density approximation. For each peak of the correlation function, while the second exponent specified its position by k_i and curvature by α_i, the first exponent adjust its height by parameter σ. The parameters ρ_i, β_i are the atomic density and number of symmetry in the lattice plane. The features of the Gaussian curve have physical meanings related to the crystal lattice. The curvature is related to energy contribution due to lattice displacement and the height relates directly to the amount of excessive energy. Thus, the elastic property and stability of the crystal can be adjusted by changing these features, making it possible to produce a crystal that can respond to mechanical and thermal changes.

In order to incorporate the chemical contribution in the free energy, the foregoing XPFC model of single component has been expanded to a version for binary alloy (see details in [43]). The general expression of the free energy functional can be written as,

$$F = \int \left\{ \frac{1}{2}n^2 - \frac{\eta}{6}n^3 + \frac{\chi}{12}n^4 + \omega \Delta F_{\text{mix}} + \frac{\alpha}{2}|\nabla c|^2 - \frac{1}{2}n \int [C^2(r-r')n']dr' \right\} dr \tag{2.61}$$

in which the contribution of mixing ΔF_{mix} is expanded as,

$$\Delta F_{\text{mix}} = (1+n)\left[c \ln\left(\frac{c}{c_0}\right) + (1-c)\ln\left(\frac{1-c}{1-c_0}\right)\right] + \frac{1}{2}\epsilon(c-c_0)^2 \tag{2.62}$$

The first and second terms are entropy and enthalpy contributions, respectively. The coefficient ω and ϵ are used for fitting the ideal free energy away from the reference concentration c_0. Typically, the enthalpy energy varies with the temperature and ϵ is given as its linear function [44],

$$\epsilon(T) = -4 + \epsilon_0(T - T_c) \tag{2.63}$$

in which the critical temperature T_c indicates the effect of de-mixing starts as the temperature goes down below it. By combining with the second-order concentration gradient $|\nabla c|^2$, the ideal free energy resembles the Cahn-Hilliard free energy functional which describes the spinodal decomposition.

The effective correlation function C_{eff} is expressed by the interpolation of those for each component using the interpolation functions (X_1, X_2) between 0 and 1,

$$C_{\text{eff}} = X_1 C_{\text{AA}} + X_2 C_{\text{BB}} \tag{2.64}$$

$$X_1(c) = 1 - 3c^2 + 2c^3, X_2(c) = 1 - 3(1-c)^2 + 2(1-c)^3 \tag{2.65}$$

in which C_{AA} gives rise to type A lattice structure when concentration is low, while C_{BB} controls the type B lattice when concentration is high. The enthalpy contribution of mixing is generated when the composition is between 0 and 1.

The equilibrium density n and concentration c profile can be solved according to the Euler- Lagrange equation. The total free energy F is minimized and the dynamics can be expressed by the following evolution equations,

$$\frac{\partial n}{\partial t} = \nabla M_n \nabla \left[n - \frac{\eta}{2} n^2 + \frac{\chi}{3} n^3 + \omega \frac{\delta(\Delta F_{\text{mix}})}{\delta n} - C_{\text{eff}}(r - r') n' \right] \tag{2.66}$$

$$\frac{\partial c}{\partial t} = \nabla M_c \nabla \left[\omega \frac{\delta(\Delta F_{\text{mix}})}{\delta c} - \frac{n}{2} \frac{\delta C_{\text{eff}}}{\delta c} n' - \alpha \nabla^2 c \right] \tag{2.67}$$

2.3 Verification

2.3.1 Interface kinetics

The numerical results of the kinetics of the diffuse interface model have been directly compared with the analytical solution of the sharp interface model. Fig.2.6a shows the moving interface with a diffuse profile, which is resolved by 5 grids. The kinetic coefficient is 10^{-4} m/(s·K). The velocities of diffuse interfaces under a range of undercooling were measured and scattered in Fig.2.6b against the linear plot of the analytical solution, of which the slope is the kinetic coefficient. It is apparent that the numerical results agree well with the analytical solution for low undercooling and deviate from the analytical line when undercooling becomes large. As formulated previously, the linear proportionality of the undercooling and the velocity is only possible when the moving diffuse profile is the same as the stationary one. For relatively high undercooling, the diffuse profile may deviate from the stationary one and cause spurious effects in Eq.(2.15). This suggests that there is a limit for the diffuse interface model in approximating the sharp interface model.

During numerical implementation, the phase-field equation, which has both diffusion and reaction terms, requires two types of criteria for obtaining an accurate solution. For finite differentiation in one or two dimensions, the stability criteria for the diffusion term is

$$\mu\Gamma\frac{\Delta t}{(\Delta x)^2} < 0.2 \tag{2.68}$$

Empirically, the number should be smaller than 0.15 in three-dimensional computation. The stability criterion for the reaction terms requires [26] that

$$\frac{\eta\sqrt{\phi(1-\phi)}}{\pi\Gamma}\Delta T < 0.5 \tag{2.69}$$

which can be reduced to be,

$$\eta\Delta T < \pi\Gamma \tag{2.70}$$

Therefore, the multiplication of the interface width and undercooling is limited by the Gibbs-Thomson coefficient in the diffuse interface model. In the result of Fig.2.6, the G-T coefficient is 2.0×10^{-4} Km and the interface width is 10^{-4} m. Thus, the undercooling is limited to be lower than 6 K, which is consistent with Fig.2.6b.

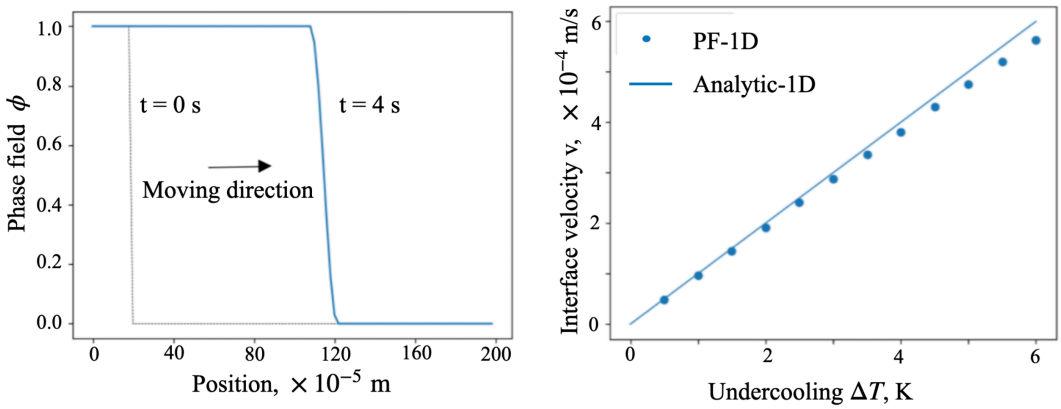

Figure 2.6: (a) phase field of the solid phase shows the moving diffuse interface; (b) comparison of interface kinetics of diffuse and sharp interface models.

The effect of surface pressure needs to be considered for interface kinetics in the two-dimensional domain. The surface pressure is the multiplication of curvature and the surface tension. For the simple case of circular grain, the curvature is the reciprocal of the radius, thus, the surface pressure is inversely proportional to the radius of the grain. As the grain grows to a larger size under constant undercooling, the interface velocity should not be constant because the

surface pressure decreases as the grain expands in its size. So the interface velocity is linearly proportional to the reciprocal of the radius. As Fig.2.7a shows, the previous 1D simulation is extended to two dimensions, the circular solid phase is growing in the liquid phase. The change of the interface velocity with the reciprocal of radius has been plotted in Fig.2.7b. For undercooling as low as 1K, the plot of the simulation result is nearly linear and agrees well with the analytical solution. As the undercooling increases, the plots at higher velocities become oscillatory and deviate progressively from the analytical solution. The same instability and inaccuracy also occurred in the previous 1D result. This suggests that the numerical solution of the diffuse interface model can be accurate when the undercooling is low for a certain interface width. For simulation under larger undercooling, the interface width needs to be reduced to meet the criterion in Eq.(2.70).

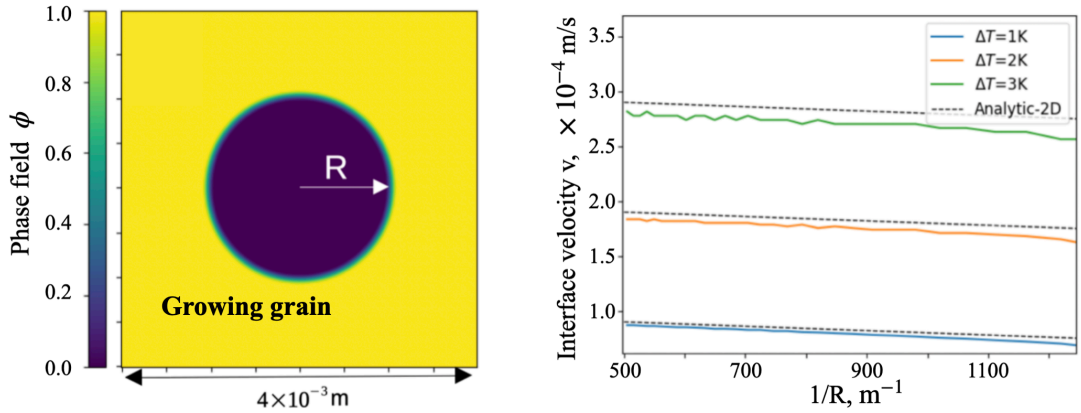

Figure 2.7: (a) phase field of the liquid phase shows the growing circular ball in the liquid phase ; (b) the plots of the variation of interface velocity with the radius reciprocal. The solid lines are simulation results and the dashed lines are the corresponding analytical solutions.

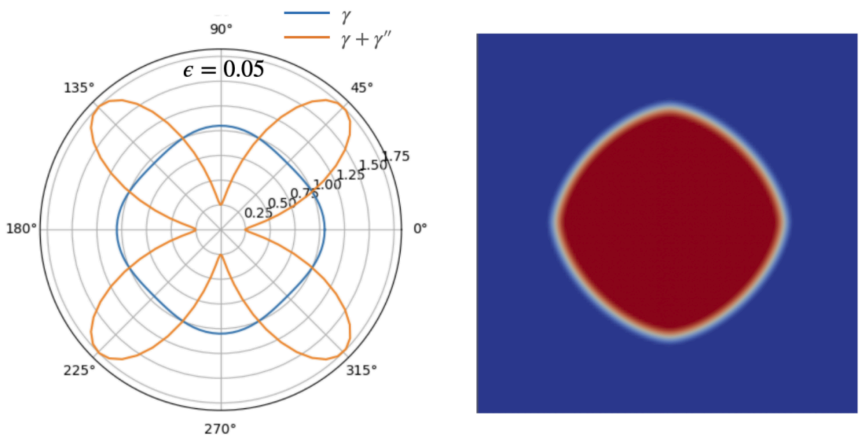

Figure 2.8: (a) polar plot of anisotropic surface energy and the stiffness. The strength of the anisotropy is 0.05; (b) the resulting growth shape with preferential growth directions.

2.3.2 Anisotropic shape

With the incorporation of the anisotropic surface energy in the diffuse interface model, the crystal will no longer be a simple circular or spherical shape but tends to have preferential growth directions. Accordingly, the surface pressure is no longer the multiplication of the curvature and surface energy but turns to be related to the surface stiffness with the consideration of the variation of surface energy with the crystallographic orientation. Fig.2.8 shows the plots of cubic anisotropic function and the simulated morphology using the corresponding anisotropic interface energy. For the anisotropic strength as low as 0.05, the shape shows its preferential expansion in {10} directions. This can be understood from either force or energy perspectives. The surface stiffness, which is the acting force on the surface, shows deep cusps in the {10} directions. Thus, the surface grows to have tips on the low-pressure surface. In other words, the surface energy is relatively large in the {10} direction, the formation of tips on these surfaces

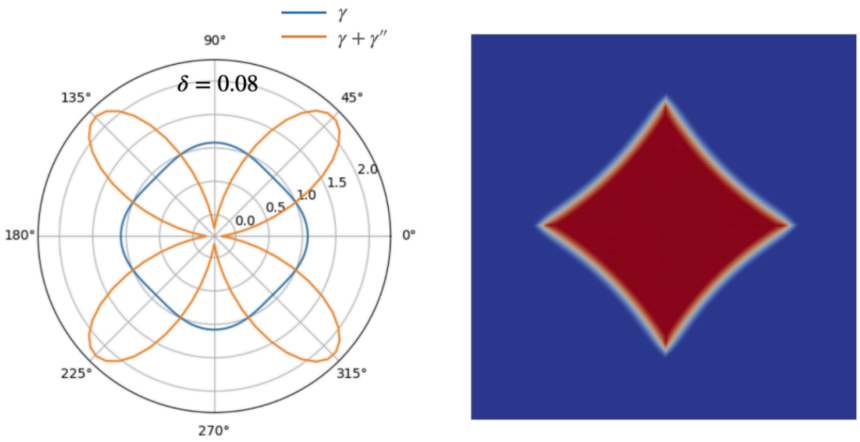

Figure 2.9: (a) polar plot of anisotropic surface energy and the stiffness. The strength of the anisotropy is 0.08; (b) the negative stiffness gives rise to the abnormal shape with missing orientations.

causes less surface energy.

As the anisotropic strength increase to be as large as 0.08, which gives rise to negative surface stiffness in some orientations, the grain is supposed to have a morphology with missing orientations. The simulation result in Fig.2.9 shows the shape with needles near the $\{10\}$ direction. The abnormal shape suggests some numerical instability in these orientations, corresponding to the missing orientations as analytically predicted.

2.3.3 Alloy solidification

As stated in the free boundary problem, the motion of the interface in alloy solidification is controlled by the diffusion process when the solid and liquid concentrations reach equilibrium values. It is expected that the diffuse interface model can reproduce this phenomenon. The 1D simulation result of the evolving concentration profiles is plotted in Fig.2.10a. As we can see, the concentration jump

becomes progressively larger until it reaches a relatively steady state. Fig.2.10b shows the temporal variation of front velocity corresponding to the front growth. The front velocity decreases quickly in the beginning and then reaches a steady state in accordance with the variation of concentration profiles in Fig.2.10a. Additionally, the increase in interface width does not cause a notable change of interface velocity after 0.8×10^{-6} s. The two plots of different interface widths almost overlap after the initial transition.

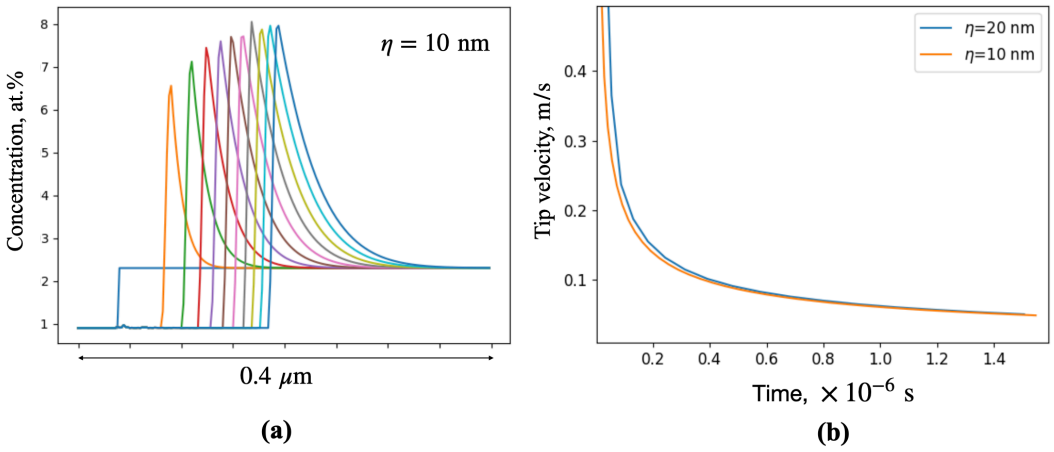

Figure 2.10: 1D simulation of alloy solidification. (a) the progressive profiles of concentration; (b) the front velocity changing with time.

The 2D simulations (Fig.2.11) were conducted by expanding the previous 1D simulations without changing other conditions. The tip velocity was measured along the bottom lines of the simulation domains. Unlike the 1D result, the front velocities, as well as the grain morphology, are significantly affected by the interface width. The front with larger interface width moves at a higher velocity. In the 1D simulation, the solute diffusion is restricted in the direction normal to the growth front, whereas, in the 2D simulation, the solute atoms are transported in both normal and lateral directions. The resulting solute diffusion along the arc length of the diffuse interface alters the liquid concentration, namely the free

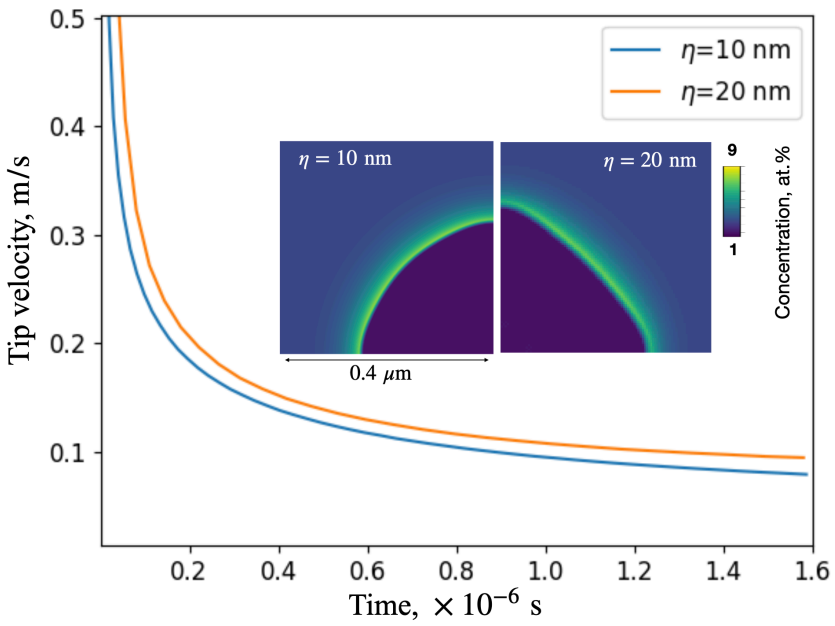

Figure 2.11: 2D simulation of alloy solidification. In contrast to the previous 1D result, The tip velocities and grain morphology are affected by interface width.

energy difference (or undercooling) that drives the interface motion. The alternation of interface concentration varies with the interface width. Consequently, the simulation results of alloy solidification in 2D are dependent on the interface width. One can imagine the usage of a very thin interface, even close to the physical size of 1 nm, may reduce the effect of the arc length diffusion and produce 2D results that are consistent with the analytical results. But this may require a great amount of computational cost. It is challenging to obtain accurate simulation results when concentration fields are coupled with the phase field.

The grain number has been expanded to multiple grains with independent orientations to test the applicability of the multi-phase-field model. As shown in Fig.2.12, four initial grains with the same size but different orientations grew in the liquid until the impingement happened. The diffusion layer emerges in the beginning and the grains grew in the preferential direction because of the incorpo-

rated anisotropic interface energy and mobility. The concentration in the liquid between the impinging grains is higher than the concentration far away from the solid front. As a result, the solid grains grow slower towards each other and tend to intrude into the liquid with lower concentration. In the maps of interface contours (b2), the formation of the grain boundaries between some grains is noticeable. The solid-solid-liquid triple junction behaves quite well as the solid front accumulated with solute has a concave shape. Although the driving force at the triple junction does not possess full consistency with thermodynamics (Eq.(2.49)), the multi-phase-field model can still be expected to showcase the growth of the grains with multiple junctions(Fig.6.2 in [15]). Last but not least, the velocity of the growth front is about 0.1 m/s, which is quite fast in the realistic processing of solidification. For such high speed, the solute partitioning may be far from equilibrium. The solid and liquid concentrations should deviate from the equilibrium phase diagram. The assumption of the equilibrium in simulations of Fig.2.10, 2.11 and 2.12 is made to demonstrate the diffusion-controlled growth as discussed in the sharp interface model. In the next chapter, the effect of the interface width on the growth kinetics will be tackled for the purpose of accurate simulation of the alloy solidification. Additionally, non-equilibrium solute partitioning will be introduced to simulate the realistic propagation of solid-liquid interface in rapid solidification.

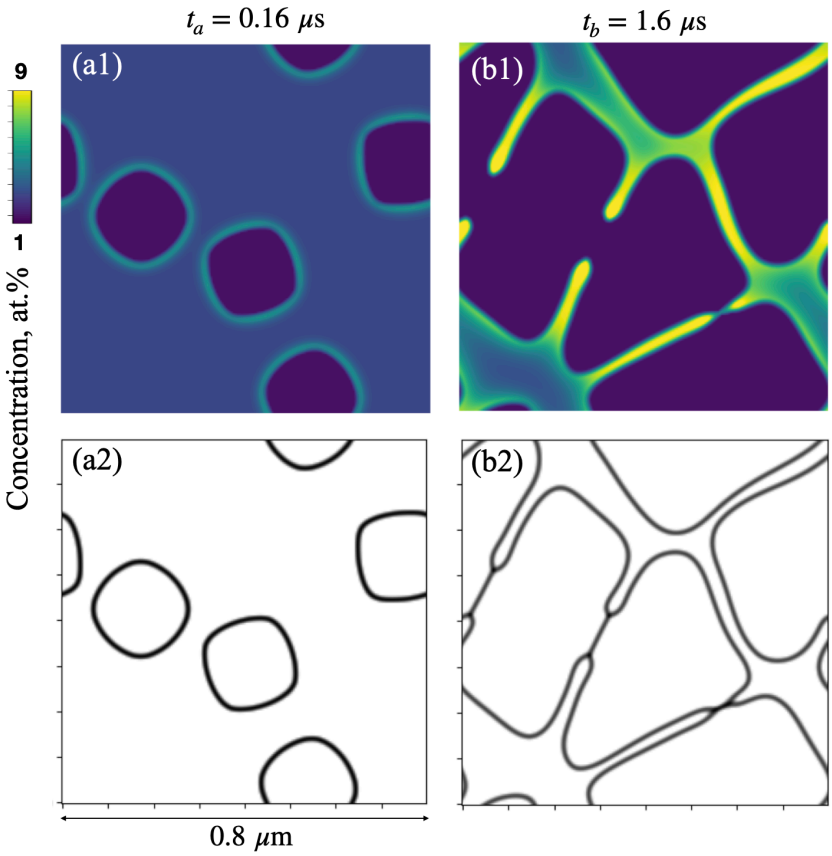

Figure 2.12: The concentration maps (upper) and contours of the interface (lower) of the growth of multiple grains with independent crystallographic orientations.

2.3.4 Solidification on the atomic scale

Crystal shape

In the theoretical perspective of crystal shape, when the interface energy changes from isotropic to anisotropic characteristic, the equilibrium morphology of crystallite turns from spherical to faceted shape. Each faceted plane corresponds to a minimum or cusp of interface energy for a specific crystal orientation. Fig.2.13 shows how the morphology of crystallites is adjusted in the PFC model. By changing the peak width ratio of the correlation function for the square phase, the morphologies are changed from a sphere to cubic without alteration of their lattice symmetry. In the insets on the right corners, it can be seen that the interfaces vary from rough to flat type. For the former type, the atoms are attached to the interface in its normal direction. For the latter one, the atoms move laterally on the flat interface and the interface grows layer by layer. The interface morphology and growth mode in the PFC model are consistent with crystallization theory [45].

Grain boundary

For the symmetric grain boundary, the mode of variation for the grain boundary energy changes as the misorientation angle increases. For small angle grain boundary (<15°), the energy-angle relation can be expressed by the Read-Shockley formula, $\mathrm{E} = \mathrm{E}_0(A - \ln\theta)$, in which E_0 and A reflects the material properties. The sources of the excessive energy are the elastic strain energy caused by the defects in the lattice and core energy due to the dangling bonding of atoms near the defects. As the misorientation angle increases, the increasing tendency of energy is almost monotonous along with the multiplication of defects. However, for large angle grain boundary (>15°), instead of increasing the number of defects, the coherency between the lattices can be significantly increased by the formation of coincident site lattices (CSL), which gives rise to the decrease of grain boundary

energy. In the square symmetry, two of the CSL grain boundaries are Σ13 and Σ5 corresponding to the misorientation angle of 22.62° and 36.87° [46]. Since the equilibrium solid phase in PFC model has the crystalline symmetry, the defects and CSL at the grain boundary can naturally arise when two grains with misorientation impinge with each other. Subsequently, the PFC result of grain boundary varying with the misorientation angle is shown in Fig.2.14. The grain boundary energy increases as the RS reaction for small angle grain boundary and exhibit cusps at CSL for larger angle grain boundaries. The result is well consistent with the theoretical analysis above. It could be anticipated that the PFC model is able to produce more complex CSL grain boundaries for other types of lattice symmetry.

Binary alloy

The simulation of crystal growth of binary alloy starts with analyzing the phase stability, which involves the calculation of free energy curves for each phase with a particular lattice structure. By substituting the density approximation and the correlation function which are constructed based on the lattice structures, such as triangle and square, the total free energy in the volume of a unit cell can be expressed as a function of temperature σ, concentration c, and amplitude A, A_1, A_2. Thus, for a set of σ and c, the free energy can be minimized by equilibrium amplitudes in the density approximation function. By repeating this process for different concentration c, the free energy curve as a function of concentration at a temperature can be obtained, as shown in Fig.2.15a. The coexistence and transformation can be known by doing the common tangent construction between the free energy curves of liquid and different crystal lattices. Then, more coexistence information is obtained by repeating the above process at different temperatures. The eutectic phase diagram is drawn in Fig.2.15b, which shows the stability information of liquid, square, and triangle.

Solute segregation

Segregation of solute atoms at the grain boundary is normal in alloy materials. The main reason for this is that lattice strain caused by defects at the grain boundary can be relaxed by the interstitial atoms. This effect is the so-called chemo-mechanical interaction [13]. The isomorphous system of the PFC model has been used to model the effect of grain boundary defect on solute segregation. The lattice is initialized by density approximation, and the initial temperature and concentration are determined to be ($\sigma = 0.1$, c = 0.2), which is in the solid region of the phase diagram. Then, the bicrystal is prepared with small and large misorientation angles, of which the values are 10° and 36°, respectively. As the results in Fig. 2.17 shown, for low angle grain boundary (LAGB), the solute atoms are concentrated near the dislocation; for high angle grain boundary (HAGB), since the features of coincident site lattice, the concentration is relatively uniformly concentrated along the boundary line. To compare the amount of segregation, the concentration profiles are plotted in Fig. 2.18. As it shows, the concentration has a higher peak for HAGB than that for LAGB. It is consistent with theoretical expectations since the atoms at HAGB are arranged in a more disordered way than those of LAGB with an array of dislocations.

Grain selection

During the solidification process, multiple grains nucleate and undergo selection when they are growing into the liquid under the temperature gradient. The chance of survival for a grain depends on its initial orientation, morphological anisotropy, interaction with neighbor grains, solute diffusion, and cooling condition. As shown in the foregoing examples, the multi-physics during polycrystalline solidification can be inherently incorporated into the PFC model. The alloy model should be appropriate for simulating the grain selection from the liquid and providing insights on the atomic length scale and diffusive time scale. As shown in Fig.2.19.

At the beginning of the simulation, one hundred initial seeds with random orientation are put at the bottom of the domain. After cooling the temperature under the solidus line in the phase diagram, the seeds started to grow into the liquid. As a result, only part of the grains survives, which tends to align their {11} orientation to the cooled liquid. As the {11} tips grow into the liquid, the solute atoms are easily rejected and accumulate in the grooves beside. The low concentration and high undercooling near the {11} tips facilitate their growth. In addition, the grain boundary energy may also act as a factor for grain selection. Since the {11} tip is the preferential growth direction, the low-angle grain boundary can hardly form between neighbor grains. Instead, the CSL grain boundary with lower energy should form during the growth. To confirm this hypothesis, the misorientation between the grains is measured in the density field of Fig.2.19. The grain boundaries labeled from (1) to (4) have the misorientation angle of 36°, 43°, 35°, and 36°, respectively. These values are almost consistent with the Σ5 CSL, as indicated in Fig. 2.14. Overall, in the PFC model, both the solute undercooling and the grain boundary energy play roles during the grain selection process. The relationship between them under different cooling conditions can be further explored in the future.

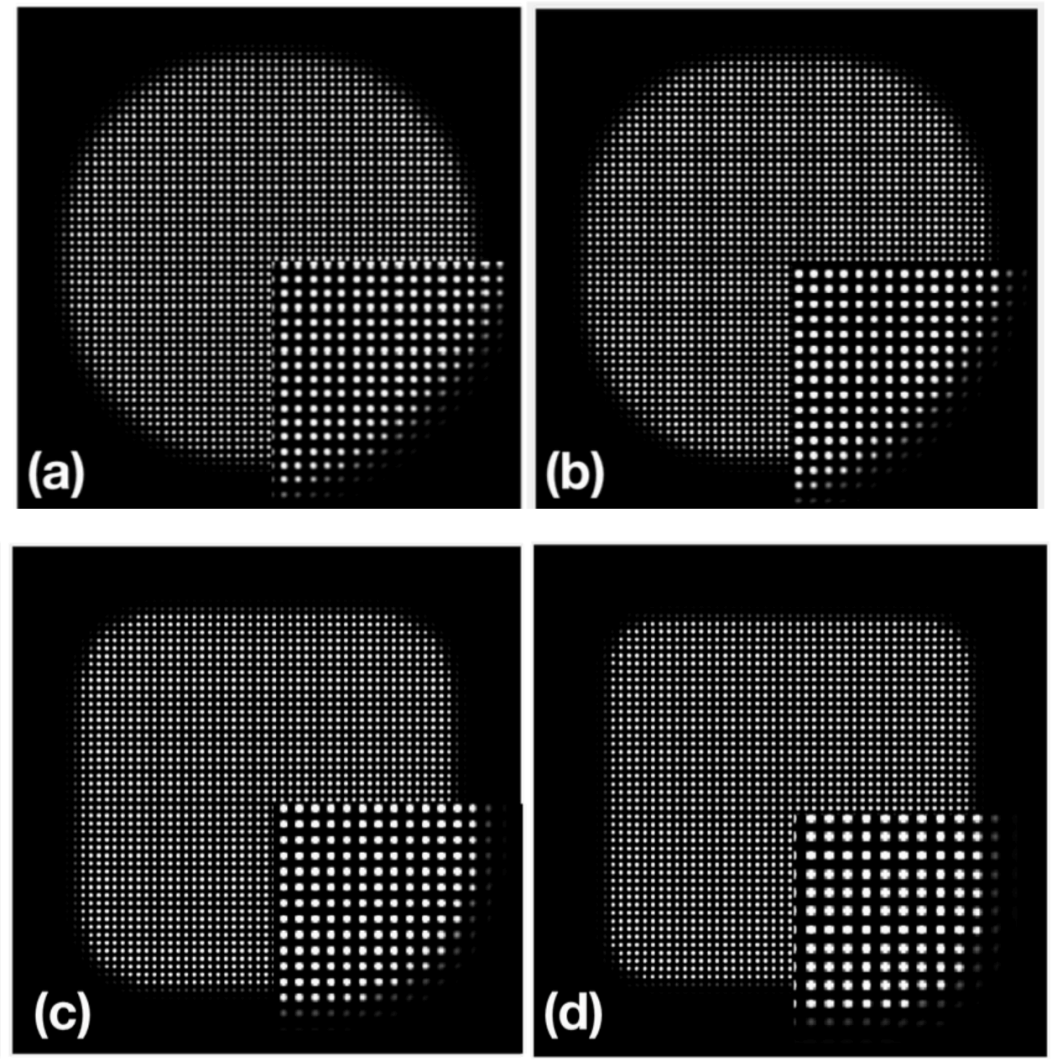

Figure 2.13: Crystallite morphologies for different ratios of peak curvature α_1/α_2. (a) 1.0/0.8 (b) 1.0/1.0 (c) 1.0/1.5 (d) 1.0/2.0

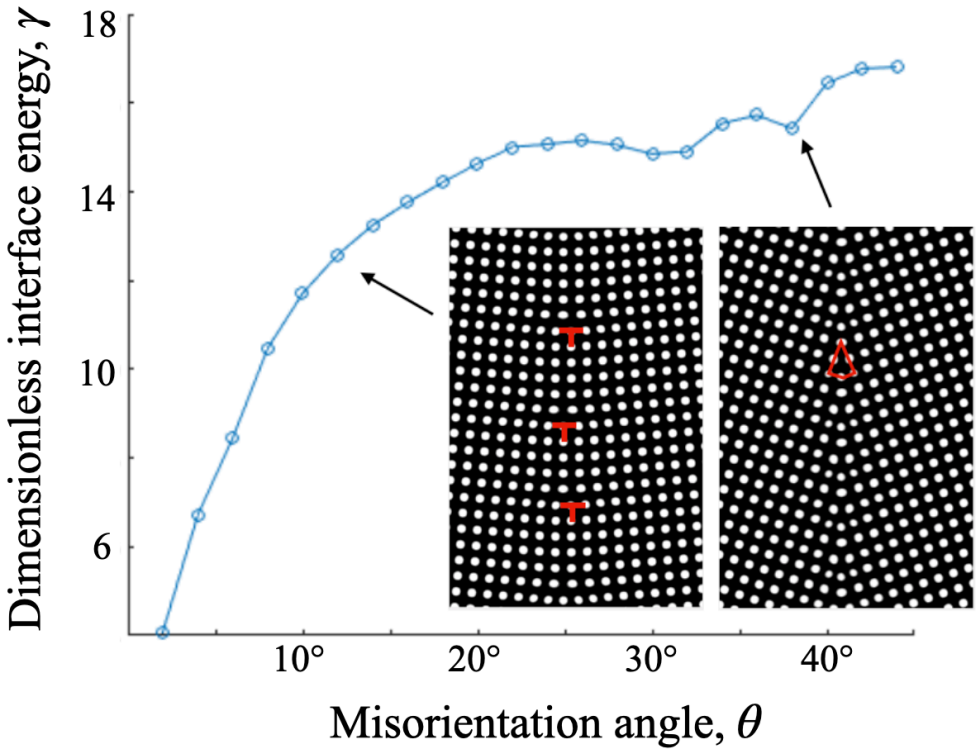

Figure 2.14: Energy and atomic arrangement of symmetric grain boundaries varying with the misorientation angle.

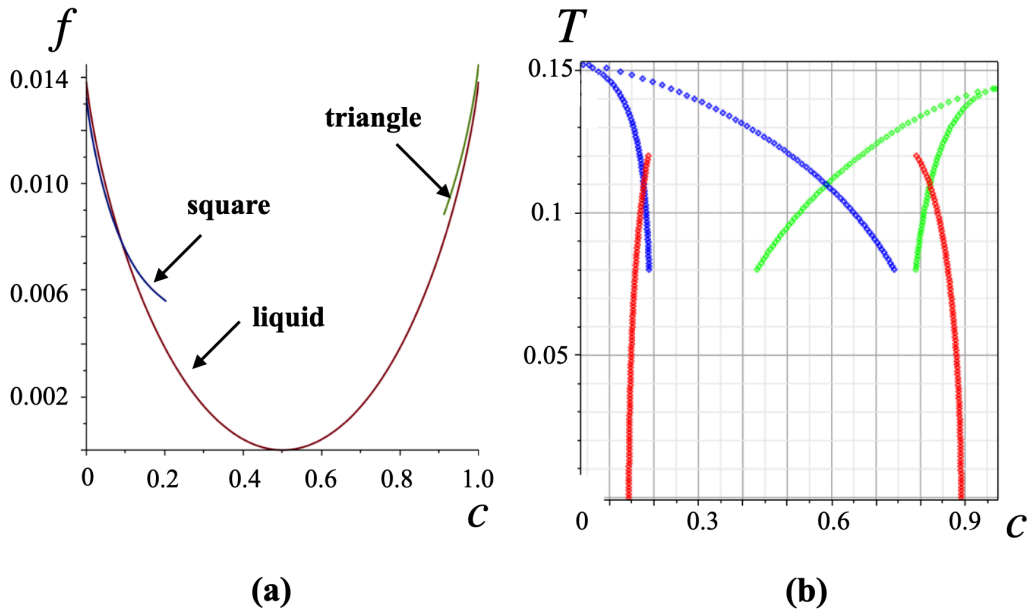

Figure 2.15: Stability analysis (a) and phase diagram (b) of square-triangle eutectic system

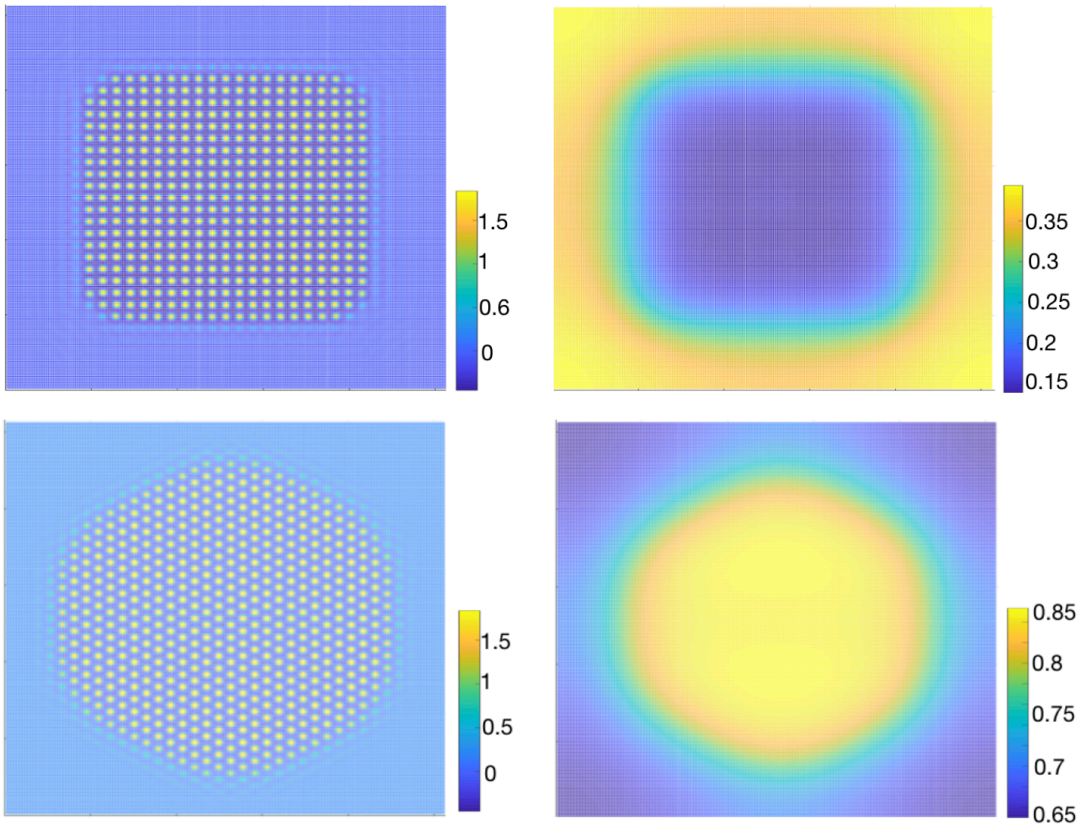

Figure 2.16: Density and concentration fields for square (a, b) and triangle (c,d) lattice crystallization. The computation domain size is 256×256.

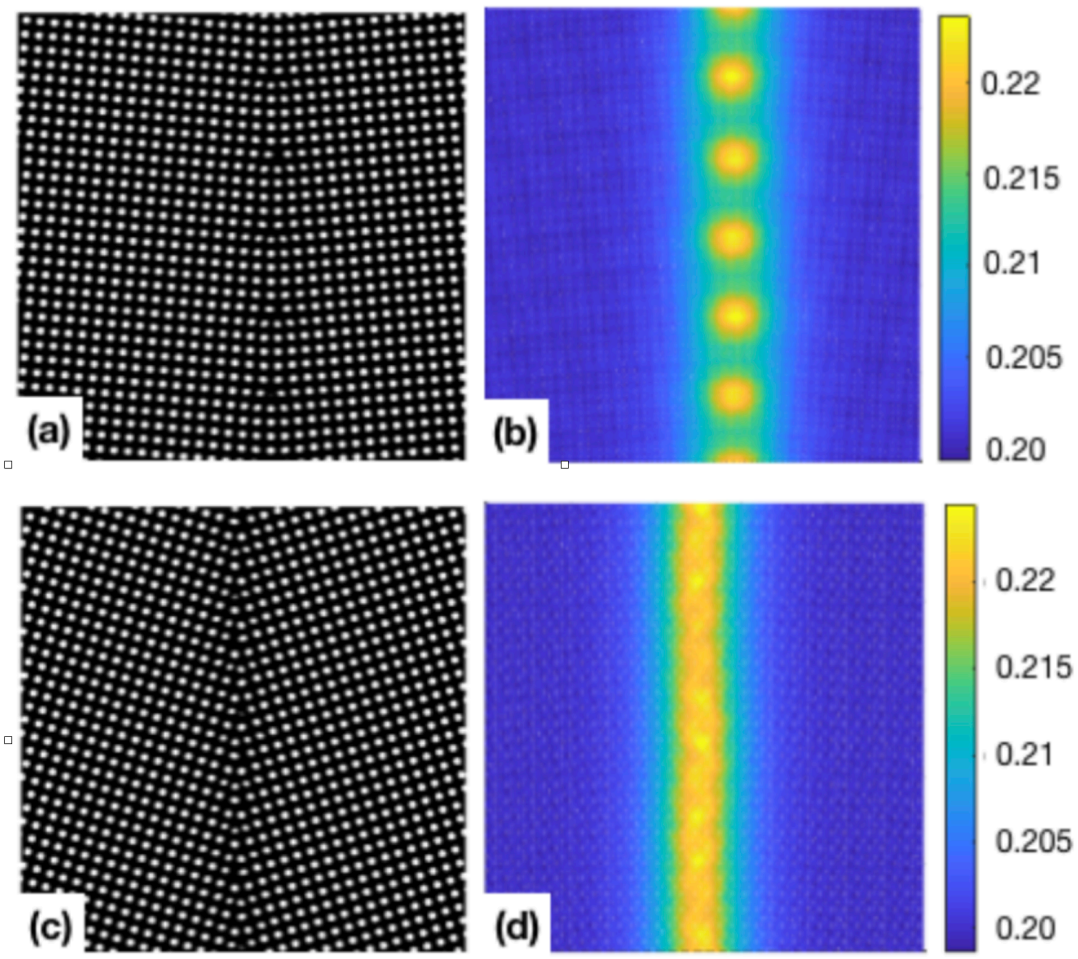

Figure 2.17: Atomic structure and concentration map of low (a, b) and high (c, d) angle grain boundary.

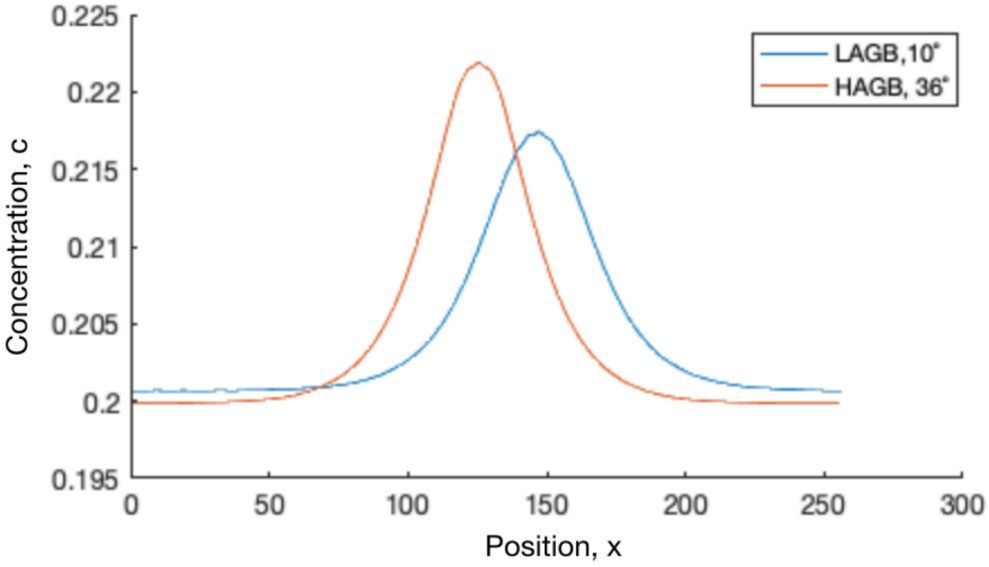

Figure 2.18: Concentration profiles across the boundary lines with defects for low and high angle grain boundaries.

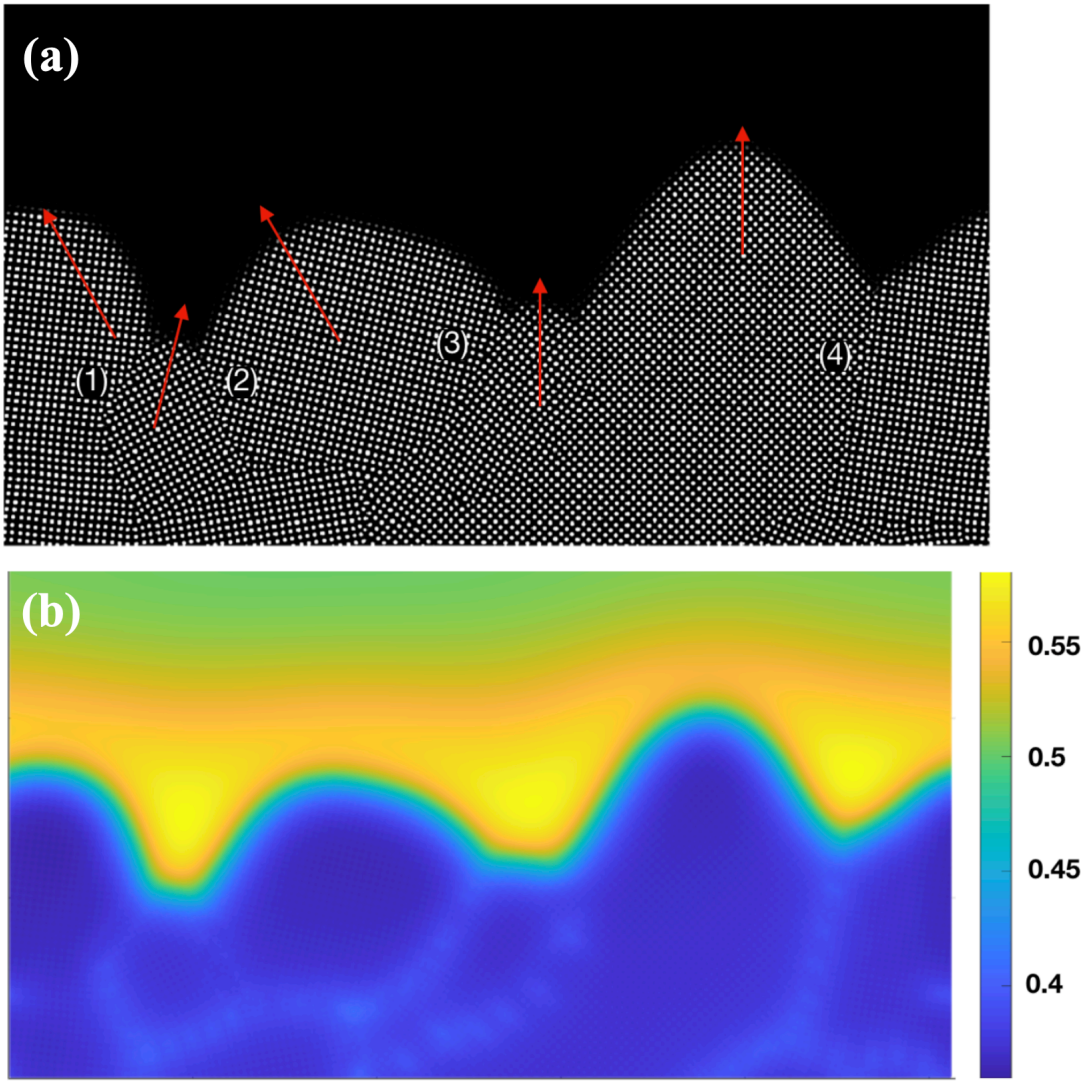

Figure 2.19: Density and concentration fields of polycrystalline solidification with random initial nuclei at the bottom. The red arrows the <11> direction of the square lattice.

2.4 Conclusions

In this chapter, a diffuse interface model that can describe the solid-liquid phase transformation involved with multiple physical processes, such curvature effect, anisotropic interface properties, crystallographic orientation, and solute redistribution, has been elaborated. The correlation of the diffuse interface model with its sharp interface counterpart has been demonstrated by deriving the governing equations and the parameters systematically. The simulation results have been rigorously compared with the analytical solution of the sharp interface model. It has been shown that the diffuse interface model can approximate the sharp interface model very well under certain limitations, which are primarily related to the artificial width of the diffuse interface. Especially, the 2D results of alloy solidification depend on the interface width. Further work is required to find a way of coupling different fields to obtain the correct numerical solution for solidification microstructures. Finally, the examples of the PFC model demonstrate its capacity of modeling nano-scale processes in crystalline materials, including anisotropic growth in crystallization, grain boundary structures and energetics, defect-induced solute segregation, and grain selection during polycrystalline solidification.

References

[1] J. A. Dantzig and M. Rappaz, *Solidification*. EPFL Press, 2009. 1, 2, 2.2.1, 2.2.4, 3, 4.2.1, 5.1

[2] J. B. Collins and H. Levine, "Diffuse interface model of diffusion-limited crystal growth," *Physical Review B*, vol. 31, no. 9, p. 6119, 1985. 2

[3] J. Langer, "Models of pattern formation in first-order phase transitions," in *Directions in condensed matter physics: Memorial volume in honor of shang-keng ma*, pp. 165–186, World Scientific, 1986. 2

[4] G. Caginalp and P. Fife, "Phase-field methods for interfacial boundaries," *Physical Review B*, vol. 33, no. 11, p. 7792, 1986. 2, 2.2.1

[5] L.-Q. Chen, "Phase-field models for microstructure evolution," *Annual review of materials research*, vol. 32, no. 1, pp. 113–140, 2002. 1.1, 2

[6] I. Steinbach, "Phase-field models in materials science," *Modelling and simulation in materials science and engineering*, vol. 17, no. 7, p. 073001, 2009. 1.1, 2, 2.2.1, 2.2.2, 2.2.5, 3.1, 3.2.1, 3.2.3, 4.2.2, 5.2.1, 5.5

[7] R. W. Balluffi, S. M. Allen, and W. C. Carter, *Kinetics of materials*. John Wiley & Sons, 2005. 2.1, 2.2.1, 2.2.1

[8] R. Trivedi and W. Kurz, "Dendritic growth," *International Materials Reviews*, vol. 39, no. 2, pp. 49–74, 1994. 1.2.3, 2.1, 5.3.1, 5.3.2

[9] T. Duffar and A. Nadri, "The grain–grain–liquid triple phase line during solidification of multi-crystalline silicon," *Comptes Rendus Physique*, vol. 14, no. 2-3, pp. 185–191, 2013. 2.1, 3.1, 3.3.2

[10] S. M. Allen and J. W. Cahn, "Ground state structures in ordered binary alloys with second neighbor interactions," *Acta Metallurgica*, vol. 20, no. 3, pp. 423–433, 1972. 2.1

[11] M. Gururajan, "Noc:phase field modelling: the materials science, mathematics and computational aspects," 2018. 1.1, 2.1

[12] W. Kurz and D. Fisher, *Fundamentals of solidification*. Trans Tech Publications, 1986. 1, 1.2.2, 2.2.1, 4.1, 5.1

[13] D. A. Porter, K. E. Easterling, and M. Y. Sherif, *Phase transformations in metals and alloys*. CRC press, 2009. 1, 2.2.1, 2.3.4, 3

[14] C. Beckermann, H.-J. Diepers, I. Steinbach, A. Karma, and X. Tong, "Modeling melt convection in phase-field simulations of solidification," *Journal of Computational Physics*, vol. 154, no. 2, pp. 468–496, 1999. 2.2.1, 2.2.2, 2.2.3, 5.2.1, 5.2.1

[15] I. Steinbach, *Lectures on Phase Field*. Springer, 2023. 1.1, 1.2.3, 2.2.1, 2.2.2, 2.3.3

[16] OpenPhase, "Open source package for phase-field modeling," 2023. 1

[17] J. W. Cahn and J. E. Hilliard, "Free energy of a nonuniform system. i. interfacial free energy," *The Journal of chemical physics*, vol. 28, no. 2, pp. 258–267, 1958. 1.1, 2.2.2

[18] R. A. Fisher, "The wave of advance of advantageous genes," *Annals of eugenics*, vol. 7, no. 4, pp. 355–369, 1937. 2.2.2

[19] A. A. Wheeler, W. J. Boettinger, and G. B. McFadden, "Phase-field model for isothermal phase transitions in binary alloys," *Physical Review A*, vol. 45, no. 10, p. 7424, 1992. 2.2.3

[20] A. A. Wheeler, W. J. Boettinger, and G. B. McFadden, "Phase-field model of solute trapping during solidification," *Physical Review E*, vol. 47, no. 3, p. 1893, 1993. 2.2.3, 5

[21] A. A. Wheeler, G. B. McFadden, and W. J. Boettinger, "Phase-field model for solidification of a eutectic alloy," *Proceedings of the Royal Society of London. Series A: Mathematical, Physical and Engineering Sciences*, vol. 452, no. 1946, pp. 495–525, 1996. 2.2.3

[22] S. G. Kim, W. T. Kim, and T. Suzuki, "Phase-field model for binary alloys," *Physical review e*, vol. 60, no. 6, p. 7186, 1999. 2.2.3, 2.2.3, 5.1, 5.2.2

[23] J. W. Cahn, "On spinodal decomposition," *Acta metallurgica*, vol. 9, no. 9, pp. 795–801, 1961. 1.1, 2.2.3

[24] W. J. Boettinger, J. A. Warren, C. Beckermann, and A. Karma, "Phase-field simulation of solidification," *Annual review of materials research*, vol. 32, no. 1, pp. 163–194, 2002. 1.1, 2.2.3, 5.2.1, 5.2.1

[25] O. Tschukin, A. Silberzahn, M. Selzer, P. G. Amos, D. Schneider, and B. Nestler, "Concepts of modeling surface energy anisotropy in phase-field approaches," *Geothermal Energy*, vol. 5, pp. 1–21, 2017. 2.2.4, 2.2.5

[26] T. Takaki, "Phase-field modeling and simulations of dendrite growth," *ISIJ international*, vol. 54, no. 2, pp. 437–444, 2014. 1.1, 2.2.4, 2.3.1

[27] K. G. Libbrecht, "Physical dynamics of ice crystal growth," *Annual Review of Materials Research*, vol. 47, pp. 271–295, 2017. 1.1, 2.2.4

[28] A. K. Boukellal, A. K. S. Elvalli, and J.-M. Debierre, "Equilibrium and growth facetted shapes in isothermal solidification of silicon: 3d phase-field simulations," *Journal of Crystal Growth*, vol. 522, pp. 37–44, 2019. 2.2.4, 3.1, 3.2.2

[29] J. Debierre, A. Karma, F. Celestini, and R. Guérin, "Phase-field approach for faceted solidification," *Physical Review E*, vol. 68, no. 4, p. 041604, 2003. 2.2.4, 3.2.2

[30] I. Steinbach, F. Pezzolla, B. Nestler, M. Seeßelberg, R. Prieler, G. J. Schmitz, and J. L. Rezende, "A phase field concept for multiphase systems," *Physica D: Nonlinear Phenomena*, vol. 94, no. 3, pp. 135–147, 1996. 2.2.5

[31] I. Steinbach and F. Pezzolla, "A generalized field method for multiphase transformations using interface fields," *Physica D: Nonlinear Phenomena*, vol. 134, no. 4, pp. 385–393, 1999. 2.2.5

[32] N. Moelans, "A quantitative and thermodynamically consistent phase-field interpolation function for multi-phase systems," *Acta Materialia*, vol. 59, no. 3, pp. 1077–1086, 2011. 2.2.5

[33] J. Tiaden, B. Nestler, H.-J. Diepers, and I. Steinbach, "The multiphase-field model with an integrated concept for modelling solute diffusion," *Physica D: Nonlinear Phenomena*, vol. 115, no. 1-2, pp. 73–86, 1998. 2.2.5

[34] B. Nestler and A. A. Wheeler, "A multi-phase-field model of eutectic and peritectic alloys: numerical simulation of growth structures," *Physica D:*

Nonlinear Phenomena, vol. 138, no. 1-2, pp. 114–133, 2000. 2.2.5, 4.3.2, 4.4.1

[35] B. Nestler, H. Garcke, and B. Stinner, "Multicomponent alloy solidification: phase-field modeling and simulations," *Physical Review E*, vol. 71, no. 4, p. 041609, 2005. 2.2.5

[36] J. Eiken, B. Böttger, and I. Steinbach, "Multiphase-field approach for multicomponent alloys with extrapolation scheme for numerical application," *Physical review E*, vol. 73, no. 6, p. 066122, 2006. 2.2.5

[37] I. Starodumov, V. Ankudinov, and I. Nizovtseva, "A review of continuous modeling of periodic pattern formation with modified phase-field crystal models," *The European Physical Journal Special Topics*, vol. 231, no. 6, pp. 1135–1145, 2022. 2.2.6

[38] N. Provatas, J. Dantzig, B. Athreya, P. Chan, P. Stefanovic, N. Goldenfeld, and K. Elder, "Using the phase-field crystal method in the multi-scale modeling of microstructure evolution," *Jom*, vol. 59, pp. 83–90, 2007. 2.2.6

[39] P. K. Galenko and D. V. Alexandrov, "From atomistic interfaces to dendritic patterns," 2018. 2.2.6

[40] K. R. Elder, N. Provatas, J. Berry, P. Stefanovic, and M. Grant, "Phase-field crystal modeling and classical density functional theory of freezing," *Physical Review B*, vol. 75, no. 6, p. 064107, 2007. 2.2.6

[41] L. Mikheev and A. Chernov, "Mobility of a diffuse simple crystal—melt interface," *Journal of Crystal Growth*, vol. 112, no. 2-3, pp. 591–596, 1991. 1.1, 2.2.6

[42] M. Greenwood, J. Rottler, and N. Provatas, "Phase-field-crystal methodology for modeling of structural transformations," *Physical review e*, vol. 83, no. 3, p. 031601, 2011. 2.2.6

[43] M. Greenwood, N. Ofori-Opoku, J. Rottler, and N. Provatas, "Modeling structural transformations in binary alloys with phase field crystals," *Physical Review B*, vol. 84, no. 6, p. 064104, 2011. 2.2.6

[44] N. Smith and N. Provatas, "Generalization of the binary structural phase field crystal model," *Physical Review Materials*, vol. 1, no. 5, p. 053407, 2017. 2.2.6

[45] J. W. Mullin, *Crystallization*. Elsevier, 2001. 2.3.4

[46] A. Jaatinen, C. Achim, K. Elder, and T. Ala-Nissila, "Phase field crystal study of symmetric tilt grain boundaries of iron," *arXiv preprint arXiv:1006.5405*, 2010. 2.3.4

Chapter 3

Faceted Crystal Growth

The applications of the phase-field models derived in the last chapter start with the faceted growth of silicon, which is the most important material in the solar cell industry. Basically, the crystal of silicon has a diamond lattice structure, consisting of two "interpenetrating" face-centered cubic primitive lattices. The close-packed planes are in {111} orientations and have the lowest surface energy and kinetic coefficient [1, 2]. As the covalent bonds between silicon atoms are highly directional compared to the bonds in metallic crystals, the anisotropy of the surface properties of silicon crystal is stronger and exhibits cusps in the orientations of the close-packed planes. Consequently, the silicon grains in solidification have faceted surfaces, which are flat and grow at slower velocities. When multiple such grains grow in directional solidification, the impingement of growing grains gives rise to the grain boundaries. Owing to the highly preferential growth of the faceted silicon crystal, most of the grain boundaries may not be aligned with the temperature gradient and may choose inclined directions according to the orientation relationship and cooling rate. This leads to the emergence/overgrowth of grains and the final solidified microstructure with inhomogeneous grains. The understanding of grain boundary development is needed for regulating the microstructure of directionally solidified silicon ingots.

In this chapter, the phase-field model has been applied to study the development process of grain boundaries (GBs) during the solidification of multi-crystalline silicon. The utilization of the phase-field model with anisotropic surface energy and anisotropic attachment kinetic coefficient accurately reproduces the observed silicon crystal shape, aligning well with experimental findings. By simulating the growth of multiple silicon grains, it has been discovered that the development of GBs is influenced by the growth mode exhibited by the groove surfaces. This growth mode alternates between the kinetic mode and energetic mode, dependent on the orientation relationship and cooling conditions. Furthermore, the three-dimensional simulation of three grains provides a comprehensive perspective on the grain structure, including the grain-grain-grain triple line, which is unobservable in two-dimensional observations. The phase-field model presented in this study has the potential for predicting GB development and the formation of the grain structure in multi-crystalline silicon. The knowledge and insights obtained from the simulation contribute to the production of cost-effective, high-efficiency solar cells.

3.1 Solidification of Multi-crystalline Silicon

Improving the quality of silicon ingots used for solar cells requires effective control of the grain structure in multi-crystalline silicon manufactured by directional solidification [3]. The grain structure in multi-crystalline silicon ingots is characterized by the grain size, grain orientation, grain boundary (GB) and the crystal defects [4]. During the directional solidification process, most GBs deviate from the temperature gradient or the overall growth direction. The extension and interaction of these inclined GBs have a significant impact on the distribution of grain size and orientation along the growth direction [5, 6, 7, 8]. The random

orientation of silicon grains at the initial nucleation stage gives rise to the final grain structure with a large variety of GBs [9]. Consequently, understanding the development of GBs under specific growth conditions becomes imperative in order to exert control of the grain structure.

The development of grain boundaries (GBs) in silicon grains initiates at the junction where two or more grains meet the silicon melt. In a simple scenario involving two solid grains with misorientation growing into the melt under a temperature gradient, a triple junction forms where two solid-liquid interfaces and one GB converge. The progression of the GB is influenced not only by the crystallographic interaction between the solid grains but also by the behavior of the growth front surfaces. The GB tends to select the boundary plane with the lowest lattice misfit, which corresponds to the coincidence site lattice (CSL) [10]. Additionally, a force equilibrium can be reached at the triple junction between the GB and two solid-liquid front surfaces with anisotropic surface energy [11]. It is crucial to consider the influence of the growth rate as well, as the attachment of silicon atoms from the melt to the solid surface is highly dependent on the crystallographic orientation. This dependency is evident in the faceted morphology observed in silicon grains [12]. Overall, the phenomenon occurring at the triple junction is complex, posing challenges in predicting GB behavior due to the intricate interplay of factors involved.

In recent decades, significant advancements have been made in understanding the crystal growth process during silicon solidification. These progresses have been realized by theoretical, experimental, and computational studies. In-situ observations conducted by Yang et al. [12] revealed that growing silicon crystals exhibit an octahedral shape with faceted surfaces oriented in the {111} directions. Boukellal et al. [13] successfully reproduced the faceted shape of silicon crystals under isothermal conditions using the phase-field method. Their model

accounted for the anisotropic surface energy and attachment kinetic coefficient, both of which exhibited cusps in the {111} orientations. It was confirmed that these anisotropic surface properties are crucial for the formation of faceted morphology. In contrast to single grain growth, the growth of multiple grains involves grain boundaries (GBs). In-situ observations by Fujiwara et al. [14] revealed that GBs between silicon grains with <111> and <100> orientations parallel to the temperature gradient incline in opposite directions under low (1 K/min) and high (30 K/min) cooling rates. This behavior can be attributed to the effects of attachment kinetics and surface tension, which vary with the growth rate. Duffar [5] proposed the classification of groove surfaces formed by two growing grains into facet-facet, rough-rough, and facet-rough types. For facet-facet grooves, the GB is expected to follow the bisector of the two facets. The analysis of the experimental data [15] showed that only for the sample grown at high growth velocity (6 mm/min) the non-coherent GB may follow one of the bisector planes between two grains. This suggests that for most GBs, the grooves may not be a simple facet-facet type and the coherency of the GBs should be important in determining the GB direction. In a series of computational works [16, 17, 18], the phase-field simulation demonstrates the growth front formed by two misoriented silicon grains has a morphology similar to the one observed in the experiment [19], which shows a typical facet-facet groove. They also investigated the influence of coincidence site lattice (CSL) GBs. However, these simulations were limited by computational costs and were restricted to two dimensions with only two grains. Jain et al. [8] conducted phase-field simulations in three dimensions (3D), considering multiple silicon grains and exploring the interaction between GBs and their network evolution. Nevertheless, their model incorporated only pure tilt and screw CSL GBs, without considering the effects of the solid-liquid growth front surfaces.

While previous studies have shed light on the principles underlying the de-

velopment of grain boundaries (GBs) in silicon, predicting the grain structure of multi-crystalline silicon remains challenging due to several factors: (1) Limited understanding of 3D grain structure: in-situ observations and most numerical simulations have focused on the grain structure in 2D, while the actual grain structure exists in three dimensions. The evolution process of the grain structure in 3D remains largely unexplored; (2) Simultaneous influence of multiple factors: various factors such as crystallographic interaction, surface tension, and attachment kinetics influence GB development. The influence of each factor and the dominant factor on GB development is usually uncertain; (3) Complex orientation relationships: the initial random orientation of multiple silicon grains results in a wide range of possible orientation relationships and a virtually infinite number of GB cases. To address these challenges, the present research proposes the use of phase-field modeling to simulate the directional solidification of multiple silicon grains in 3D. This approach allows for the selective and sequential incorporation of various factors that may affect GB development. Based on the multi-phase-field method [20], which is commonly applied to multi-phase and multi-component problems, the proposed model can incorporate an unlimited number of grains with arbitrary orientations and independent surface properties [21, 22].

The primary focus of this investigation is to examine the impact of growth front surfaces on the development of non-coherent grain boundaries (GBs). The current model assumes isotropic GB energy. The research was conducted through the following steps: (1) Simulation of single silicon grain growth: the phase-field model was employed to simulate the faceted growth shape of a single silicon grain under isothermal conditions in a three-dimensional (3D) setting. The simulation results were then compared with experimental observations to validate the accuracy and reliability of the phase-field model; (2) Investigation of coupled grains in 2D: the study involved examining coupled grains in a two-dimensional (2D) configuration

to gain insights into the influence of growth front surfaces on GB development under different cooling conditions; (3) Expansion to realistic 3D grain structure: to demonstrate the model's capability to generate a more realistic grain structure, the simulation domain was expanded to encompass a 3D setting. This expansion allowed for a comprehensive representation of the grain structure, providing a more accurate depiction of the growth and interaction of multiple silicon grains. Through these steps, the investigation aimed to enhance understanding of the role played by growth front surfaces in the development of non-coherent GBs, thereby contributing to the broader comprehension of multi-crystalline silicon grain structure formation.

3.2 Phase-Field Model of Silicon Solidification

3.2.1 Phase-field equation for multiple grains

The phase-field model used in this study is based on the multi-phase-field method derived in Sec.2.2.5, which describes the evolution of multiple phases. Other detailed derivations of the model are also available in [20, 21, 22]. The phase-field equation has the following form,

$$\frac{\partial \phi_i}{\partial t} = -\frac{2}{n}\sum_{j=1}^{n} m_{ij}\left\{\sum_{k=1}^{n}\left[\frac{1}{2}(\epsilon_{ik}^2 - \epsilon_{jk}^2)\nabla^2\phi_k + (w_{ik} - w_{jk})\phi_k\right] - \frac{8}{\pi}\sqrt{\phi_i\phi_j}\Delta g_{ij}\right\} \tag{3.1}$$

The subscripts i, j, and k are indexes representing local phases. A pair of indexes indicates the interface or interaction between two phases. The right-hand side of the equation consists of two components that correspond to the interfacial and bulk contributions to the local phase change. Specifically, the gradient coefficient ϵ

and the penalty coefficient w in the interfacial part can be related to the interface energy γ and the width η of the artificially wide diffuse interface through the following relations:

$$\epsilon = \sqrt{\frac{8\eta\gamma}{\pi^2}} \tag{3.2}$$

$$w = \frac{4\gamma}{\eta} \tag{3.3}$$

In the bulk contribution, the difference in free energy between the two local phases acts as the driving force Δg, which nearly equals the multiplication of the undercooling ΔT and the fusion entropy S_{f}:

$$\Delta g = \Delta T S_{\mathrm{f}} \tag{3.4}$$

Additionally, the attachment kinetic coefficient β can be related to the phase-field mobility m by

$$m = \frac{\pi^2 \beta}{8\eta} \tag{3.5}$$

3.2.2 Anisotropic surface properties of silicon crystal

Considering the anisotropy of surface energy and attachment kinetic coefficient, the gradient coefficient ϵ and the phase-field mobility m should be associated with some anisotropic functions, which vary with the normal vector of the local surface. Thus, they should have the following forms,

$$\epsilon(\theta) = \epsilon_0 a(\theta) \tag{3.6}$$

$$m(\theta) = m_0 b(\theta) \tag{3.7}$$

In phase-field modeling, mild anisotropic surface properties can be incorporated using the cubic function ([23, 24]) as in Fig. 2.8. When the anisotropic strength is strong, special treatments [25, 26, 27, 28] on the cubic function are required to maintain the computation stability. For faceted anisotropic properties, one can choose a different approach including the functions with cusps in the facet orientations. The angle θ is the angle between the normal vector $\vec{n}$ of the local surface and the normal vector $\vec{n}_{111}$ of an atomically smooth $\{111\}$ surface. The parameters of ϵ_0 and m_0 are the values corresponding to the surface energy and attachment kinetic coefficient in $\{100\}$ directions, which are atomically rough. The anisotropic functions $a(\theta)$ and $b(\theta)$ should have minimums when θ is equal to zero, indicating the lowest surface energy and attachment kinetic coefficient of the surfaces in $\{111\}$ directions. To meet the above requirement, the functions are chosen to have the following forms,

$$a(\theta) = \chi\left[1 + \delta(\cos\theta + \tan\alpha_0 \sin\theta)\right] \tag{3.8}$$

$$b(\theta) = \xi + (1-\xi)\tan(\omega\theta)\tanh\left[\frac{1}{\tan(\omega\theta)}\right] \tag{3.9}$$

The coefficients inside these two functions (listed in Table 3.1) are adjusted to match the physical values of the surface energy of silicon [29] and experimental observation [12]. The plots are shown in Fig.3.1. Adapted from the broken bond model, Eq. 3.8 has been originally used in numerical simulation to model the facet growth in [30]. It has been recently used to model the growth of single silicon grain in [13] and the facets in nanowire growth in [31]. The coefficient χ outside the square brackets is used for normalizing the maximum value of the function. The angle α_0 and coefficient δ regulate the width and depth of the cusp in the plot of $a(\theta)$. In [13], α_0 is set to 35° to separate the faceted and

non-faceted surfaces. For the deviation angle larger than α_0, the surface energy keeps unchanged. However, the piece-wise function for surface energy causes the discontinuity of the surface stiffness, which is not appropriate for the simulation of multiple silicon grains with arbitrary orientations. In this work, α_0 is chosen to be 54.7°, giving rise to a smooth increase of surface energy until the {100} direction. As a result, the surface energy stiffness has a peak in <111> orientation and keeps almost constant in the range of rough surfaces, facilitating the appearance of the faceted surface and the steady transition to the rough surfaces. The faceted and non-faceted surfaces are separated through the anisotropic function for the kinetic coefficient (Eq.3.9, [32]), in which width and depth of the cusp can be regulated independently. The angle of the end of the cusp is set to be 10° in the present work although its actual value is still unknown. The implementation of the anisotropic kinetic coefficient in the phase-field model is straightforward, whereas incorporating the anisotropic surface energy is cumbersome. The mathematical procedures are detailed in the Appendix.

3.2.3 Numerical implementation

The current model does not include latent heat and thermal conduction. The temperature in the simulation is either in an isothermal condition or has a linear gradient, although it has been reported that thermal field may have a significant effect on the solidification microstructure [33]. This simplification in this study is based on the assumption that the growth rate in the simulation is lower than 40 μm/s, for which the latent heat has a negligible effect on the temperature ahead of the solid-melt surface. Studies have shown that instability of the <100> surface caused by a negative temperature gradient [34] occurs only when the growth rate surface exceeds a critical value (130 μm/s for a single grain and >37 μm/s for two-grain surface) [3]. By neglecting the latent heat effect, the model achieves

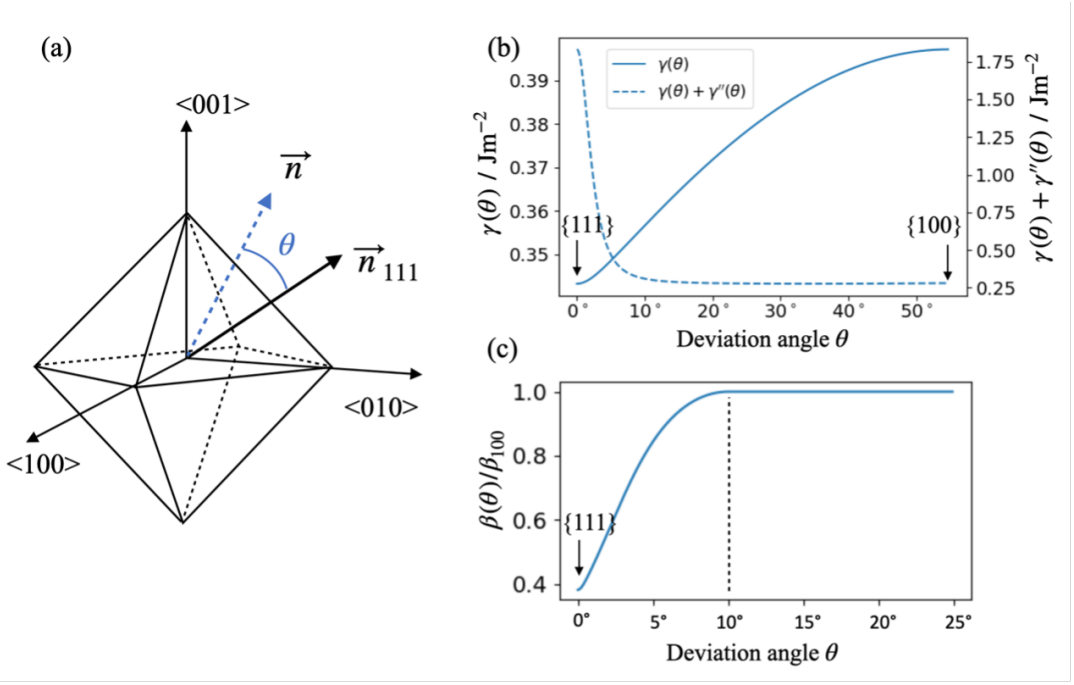

Figure 3.1: Plots of anisotropic surface properties. (a) the angle θ between the normal vectors of local and a {111} surface; (b) The surface energy (solid line) and stiffness (dashed line) change with the deviation angle of the local surface from the {111} orientation. The surface energy reaches its maximum at the angle of 54.7° in the {100} orientation; (c) The ratio of attachment kinetic coefficient of the local surface to the one in {100} orientation varies with the deviation angle from {111} orientation. The end of the cusp is chosen to be 10°.

Table 3.1: Physical properties, model parameters, and coefficients in current phase field model for silicon growth.

Names of Quantities	Symbols	Values
Grid length	Δx	2.0×10^{-5} m
Time step	Δt	2.0×10^{-3} s
Melting temperature for silicon	T_m	1687.0 K
Interface energy in 100 orientations	γ_{100}	0.44 J/m^2
Interface energy on 111 orientations	γ_{111}	0.32 J/m^2
Coefficient for regulating cusp shape in $a(\theta)$	δ	54.7°
Amplitude coefficient for $a(\theta)$	μ	0.6156
Grain boundary energy	γ_{GB}	0.6 J/m^2
Fusion entropy	S_f	2.12×10^4 J/(Km^3)
Kinetic coefficient in <100> direction	β_{100}	4.62×10^{-4} m^4/(Js)
Kinetic coefficient of grain boundary	β_{GB}	$0.05\beta_{100}$
Coefficient for cusp depth in $b(\theta)$	ζ	0.30
Coefficient for cusp width in $b(\theta)$	ω	10°
Rounding parameters	ρ	0.05

improved efficiency and stability, enabling the use of a relatively large time step. because the kinetic of the diffuse interface does not need to be coupled with the transportation of another long-range field [20]. The current model, with a grid number of 200×200×200, requires 2750 steps to produce results that match experimental observations of a single silicon grain. This efficient modeling approach paves the way for simulating the growth of multiple grains in 3D.

3.3 Simulation of Silicon Solidification

3.3.1 Growth of single silicon grain

Fig.3.2a-d show the experimental results [1] [12] of the silicon grain observed from <110> orientation at an undercooling of 4 K. The contour lines are from the

[1]Permission received from John Wiley and Sons. License number: 5410031434245.

simulation results, presented below. The grain grows to have faceted surfaces in {111} orientations at 2.0 s. At 5.5 s, these faceted surfaces meet and form sharp corners. At this moment, the temperature is slightly increased. As the growth proceeds, the sharp corners turn to be curved ones and the faceted surfaces are separated by these curved surfaces at 10.0 s. In Fig.3.2e-h, the 2D simulation results are aligned in the same time order for comparison with the experimental results above. It should be noted that the simulation results have been slightly enlarged to avoid overlapping. As can be seen, the contours of the simulation results match well with the shape of the real silicon grain both in time and length scale. It can be noticed that the aspect ratios of the contours and the grains are different because the observation direction in the experiment may not be parallel to the <110> direction. This can be verified by the elliptical shape of the initial grain in Fig.3.2a. The match between the two sets of results validates that the phase-field model can emulate the surface energy and the attachment kinetic of real silicon crystal. The 3D simulation results in Fig.3.2i-k show a more complete visualization of the growth of single silicon grain. Because both the 2D and 3D simulations use 200 grids to resolve each side of the domain. The cross-sections of the 3D results (denoted in Fig.3.2i) correspond to the 2D results above. The current model of single grain growth will act as the benchmark model and the growth of multiple grains can be simulated by simply multiplying the grid number of the domain.

3.3.2 Growth of two misoriented grains

Based on the findings of Fujiwara et al. [14], it is anticipated that the phase-field model will replicate the distinct behavior of grain boundaries (GBs) that incline in opposite directions under varying cooling rates. The initial orientation relationship and cooling conditions in the simulation have been aligned with the

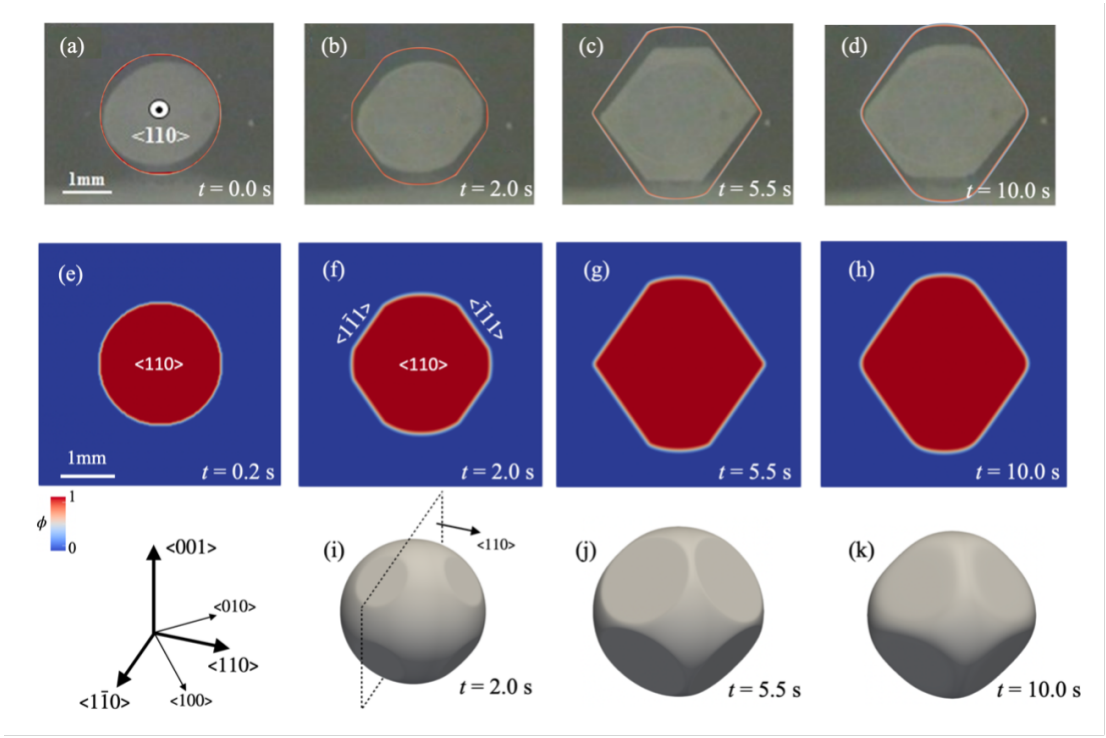

Figure 3.2: Comparison between experiment [12] and simulation results of the growth of single silicon grain. (a-d) In-situ observation at an undercooling of 4 K (after X. Yang et al. [10], reproduced with permission from Wiley.). The <110> orientation of the crystal is nearly perpendicular to the paper. The contours lines are from the simulation results below; (e-h) two-dimensional simulation results viewed from <110> orientation. The grid number is 200×200. The simulation results are slightly enlarged to avoid overlapping with the experimental results above; (i-k) three-dimensional simulation results with the same input parameters as those in the 2D ones.

experimental setup. In Fig.3.3a, the orientation of two grains with facets at the bottom of the simulation domain is depicted. The grain on the left side exhibits a <001> orientation, while the one on the right side has a $<1\bar{1}1>$ orientation. Both of them are aligned vertically. Fig.3.3b and d show two coupled rectangles (indicated by horizontal white dashed lines) as the initial grains positioned at the domain's bottom. The orientation relationship of these grains is the same as shown in Fig.3.3a. The red and blue colors represent the <001> and $<1\bar{1}1>$ orientations parallel to the temperature gradient, respectively, following a convention similar to the colorization of inverse pole figure orientation maps generated from EBSD. This coloring scheme is consistently used in the subsequent 2D and 3D simulation results. Fig.3.3c and e display the phase-field mobility map, allowing for easy identification of surface roughness. Atomically smooth surfaces are depicted in light blue, while rough surfaces are represented in red. The bulk solid and liquid phases are indicated in blue, denoting zero mobility. The mobility of the surface junction is assumed to be non-zero, except in this representation where it has been set to zero to emphasize the difference between the growth front surfaces on either side. Multiple sets of surfaces at different time steps are combined in each phase-field mobility map to illustrate the growth process.

In Fig.3.3b, a positive temperature gradient of 2500 K/m is applied from the bottom to the top, and the temperature decreases at a rate of 0.1 K/s. This corresponds to a steady-state growth rate of approximately 40 μm/s, the same as the simulation in Fig.3.2. The initial temperature at the growth front is set 4 K below the melting temperature to quickly reach a steady state. In Fig.3.3b, the simulation has been running for 22500 steps, and the <001> grain is about to cover the $<1\bar{1}1>$ grain. The presence of faceted surfaces on either side confirms the existence of a groove between the two grains (Fig.3.3c). Fig.3.3d shows the simulation result under a temperature gradient (10000 K/m) and cooling rate

(0.01 K/s), resulting in a steady-state growth rate of 1 μm/s. Accordingly, the initial temperature at the growth front is set to 0.1 K. The simulation has been run for 900000 steps. Although the growth front has traveled the same distance as in Fig.3.3b, it exhibits a flat morphology with a shallow groove. The GB inclines towards the left side, with the <1$\bar{1}$1> grain tending to cover the <001> grain. The phase-field mobility map in Fig.3.3e indicates that the shallow groove has rough surfaces on both sides. These simulation results under two different cooling conditions are consistent with experimental observations [14].

Apart from the cooling condition, changing the orientation of the initial grains can also influence the development of grain boundaries (GBs). In Fig.3.4b and e, the <1$\bar{1}$1> grain has been tilted 10° counterclockwise and 20° clockwise, respectively. The growth conditions remain the same as in Fig.3.3b. The presence of flat surfaces in the groove indicates a facet-facet characteristic. According to the bisector rule [5], the GB under a facet-facet groove should follow the bisector of the two facets. To validate this rule in the simulation, the bisectors of the facet pairs in the groove are plotted in Fig.3.3a, 3.4a, and 3.4d. They are then compared with the GB lines in Fig.3.3b, 3.4b, and 3.4e. It is important to note that the grooves in Fig.3.4b and e are formed by facets with different orientations, resulting in different types of bisectors. The bisector formed by the <$\bar{1}$11> <1$\bar{1}$1> facets is designated as type 1, while the one formed by <$\bar{1}$11><$\bar{1}$11> is designated as type 2. As a result, all the GB lines exhibit slight deviations from the bisectors. Fig.3.4c and f present simulation results with identical conditions to Fig.3.4b and e, except that the surface energy of the two grains is isotropic. The results clearly demonstrate that the GB lines align more closely with the bisectors.

Additional data regarding the inclination of grain boundaries (GBs) are presented in Fig.3.5. The inclination angle is defined as the angle between the tem-

perature gradient and the GB line, with positive values indicating right inclination and negative values indicating left inclination. In Fig.3.5a, the coupled grains exhibit the same orientation relationship (<001>//<1$\bar{1}$1>) as shown in Fig.3.3b. The GB inclination increases with the steady-state growth rate until it approaches the inclination angle of 27.35°, which is close to the bisector of the faceted groove surfaces. Fig.3.5b displays the inclination angles of coupled grains with varying orientation relationships growing at a steady-state rate of 40 μm/s. The grain on the right-hand side undergoes rotations ranging from -50° to 50°. The plots reveal that most GBs of the groove surfaces with anisotropic surface energy deviate from the bisectors, and removing the anisotropic surface energy in the simulation brings the GB lines closer to the bisectors.

3.3.3 Growth of multiple misoriented grains

The previous simulation with two misoriented grains offers a limited perspective on the potential grain boundaries (GBs) between silicon grains. In real solidification processes, multiple silicon grains can exhibit random orientations within two- or three-dimensional domains. The subsequent two-dimensional simulation results present the progression of grain structures, showcasing a wider range of GB types and illustrating the intricate development of grain boundaries.

The simulation results depicted in Fig.3.6a and 3.7a involve 10 grains with the <110> orientation perpendicular to the plane, along with random rotation angles about the <110> axis. The rotation angles (positive for clockwise rotation) and identification numbers (1-10) assigned to the grains are indicated at the bottom of Fig.3.6a. The domain size has been expanded to 20×10 mm^2 based on the benchmark model presented in Fig.3.2. The lateral sides have periodic boundary conditions, enabling the formation of a grain boundary between the left-most and right-most grains. Similar to the coloring rule in Fig.3.3 and 3.4, the colors red,

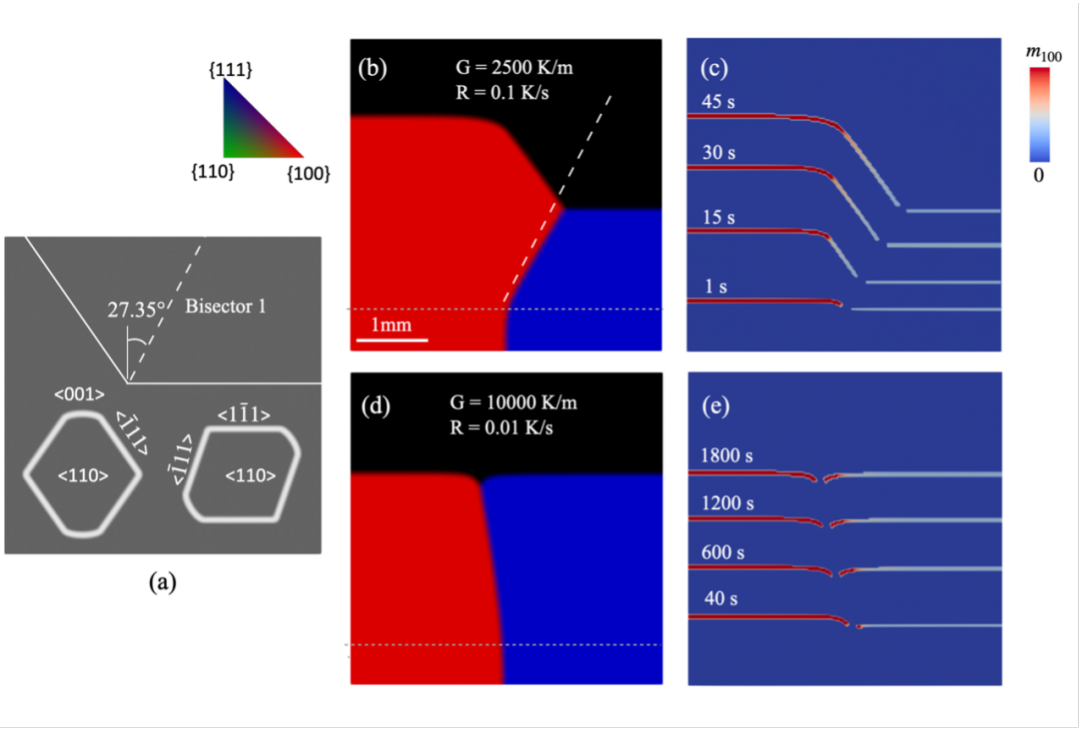

Figure 3.3: Simulation results of the grain boundary development of coupled grains with their <001> and <1$\bar{1}$1> axes parallel to the temperature gradient. (a) separate grains growing under the isothermal condition demonstrate the orientation relationship; grain couples growing at steady state growth rates of (b) 40 μm/s and (d) 1 μm/s. The color shows the orientation with respect to the positive temperature gradient from bottom to top; (c) and (e) show the distribution of phase-field mobility of (b) and (d), respectively.

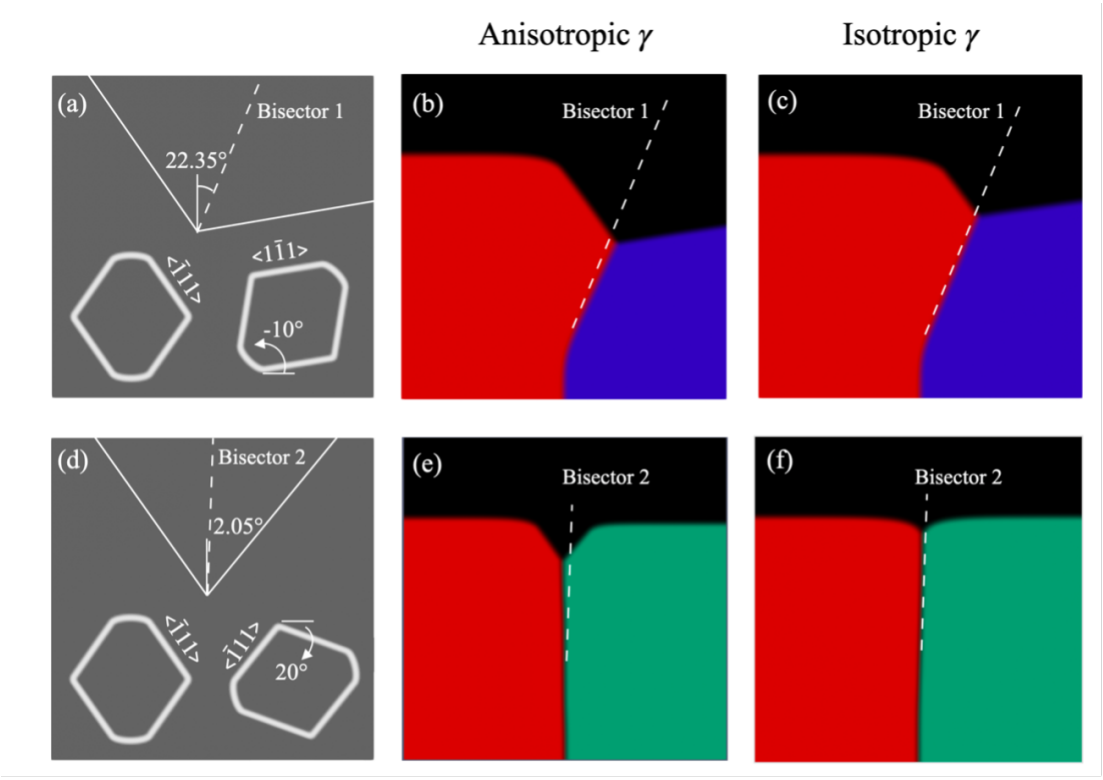

Figure 3.4: Continual simulation results of Fig.3b after rotating grains on the right-hand side about the <110> axis for (a-c) -10.0° and (d-f) 20°. The grains couples have grown under the cooling rate of 0.1 K/s and the temperature gradient of 2500 K/m (i.e., the growth rate of 40 μm/s).

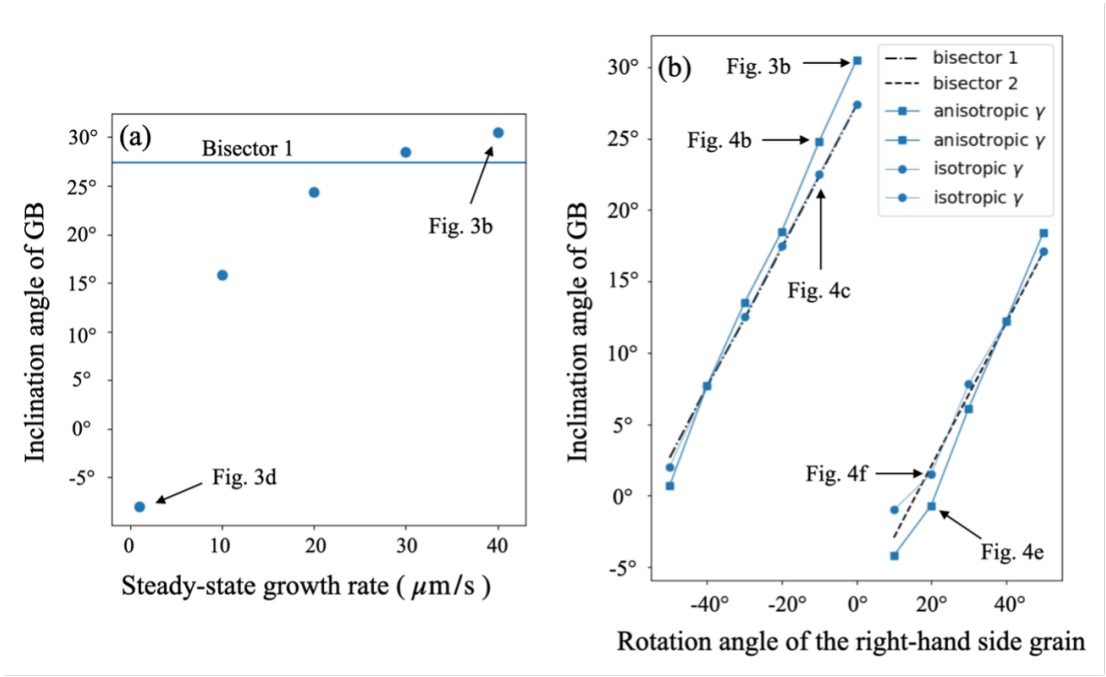

Figure 3.5: The inclination angles of the GBs vary with the (a) steady-state growth rate and (b) the orientation relationship. The grain couples in (a) have the same orientation relationship as that in Fig.3.3. For those in (b) growing at a steady-state rate of 40 μm/s, the grain on the right-hand side rotates about its <110> axis. Bisectors 1 and 2 are favored for counterclockwise and clockwise rotation angles, respectively.

green, and blue represent grains with {100}, {110}, and {111} orientations parallel to the temperature gradient. The phase-field mobility maps in Fig.3.6b and 3.7b provide clear visualization of the roughness of the growth front surfaces. In the domains of Fig.3.6 and Fig.3.7, the temperature gradient is set at 5000 K/m, and the cooling rates are 0.2 K/s and 0.05 K/s, respectively. Notably, the total number of grains tends to decrease as growth progresses due to the inclination of the grain boundaries, a commonly observed phenomenon in experiments [9]. This trend arises because most grooves exhibit faceted surfaces (Fig.3.6b), causing straight grain boundaries to incline away from the temperature gradient towards either side. However, a rough-rough groove can be observed between grains (3) and (5), with their grain boundary line exhibiting minimal inclination. Of particular interest is the curved grain boundary between grains (9) and (1). By examining the phase-field mobility map in Fig.3.6b and c, it becomes evident that the surfaces of this groove undergo continuous changes during growth. In contrast to the grain structure under high cooling rates, the pattern observed in Fig.3.7, grown under low cooling rates, displays a distinct characteristic. The overall growth front appears nearly flat, with shallow grooves. More grooves exhibit rough surfaces, and grain boundaries tend to be less inclined.

3.3.4 Three-dimensional simulation

The grain growth simulation of silicon in 3D has been rarely conducted because of the high computation cost and the difficulty in dealing with complicated orientation relationships. As Fig.3.3 shows, the current model has successfully reproduced the growth of 3D single silicon grain in both length and time scales, it is straightforward to expand the model to include multiple grains with arbitrary orientations. Fig.3.8 shows two cases of the growth of three grains in 3D. The temperature gradient is 5000 K/m and the cooling rate is 0.2 K/s in both

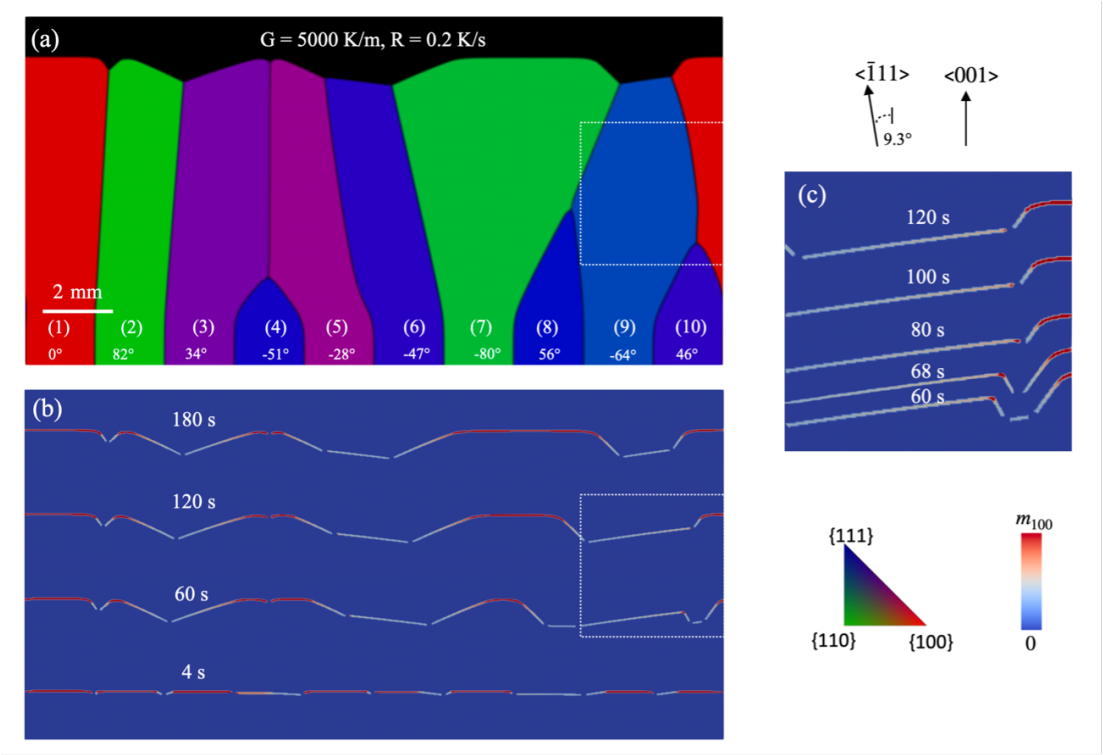

Figure 3.6: Simulation results of multiple grains with random rotation angles about the <110> axis. The steady-state growth rate is 40 μm/s. (a) orientation map; (b) phase-field mobility map; (c) a series of phase-field mobility maps showing the change of growth front surfaces of a curved grain boundary.

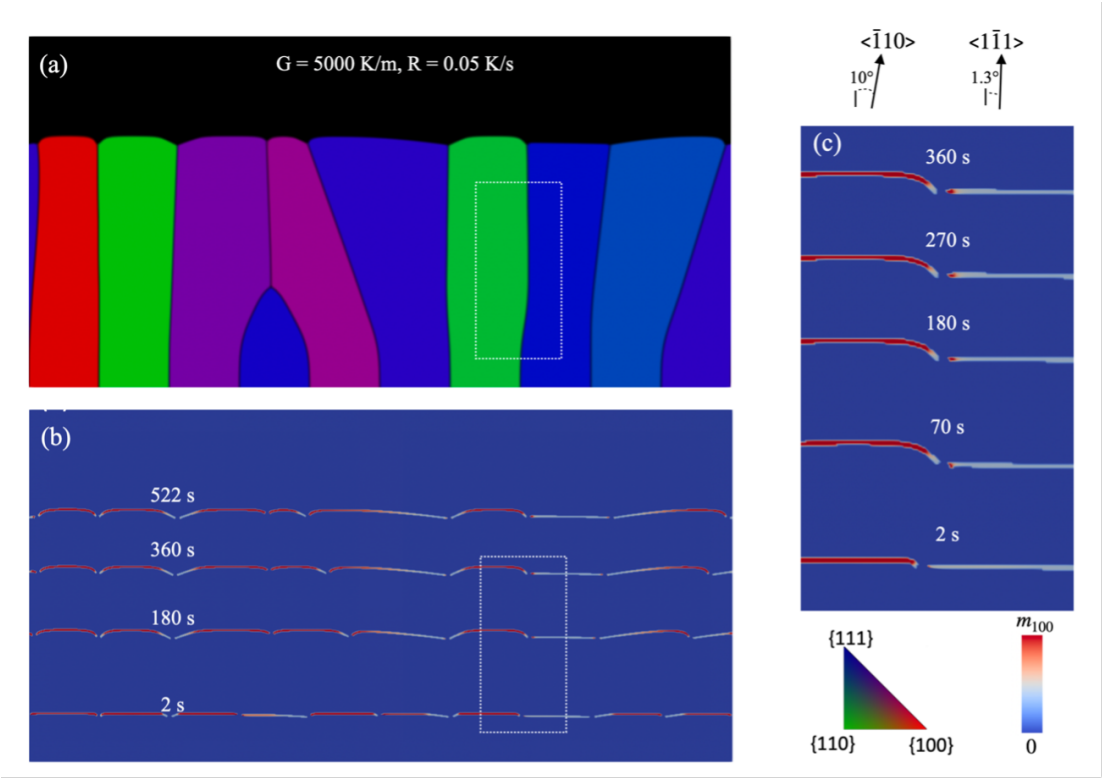

Figure 3.7: Continual simulation results of Fig.3.6. The steady-state growth rate is reduced to 10 μm/s. (a) orientation map; (b) phase-field mobility map; (c) phase-field mobility maps showing the change of growth front surfaces of a curved grain boundary.

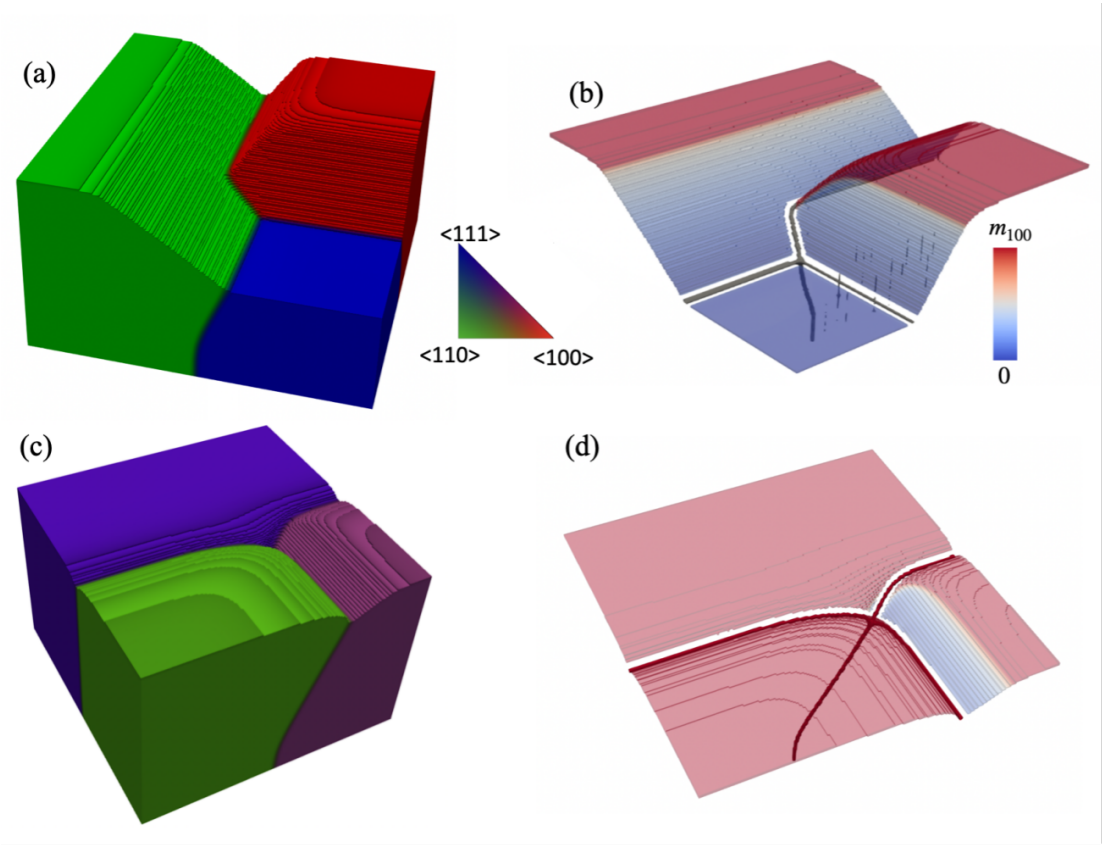

Figure 3.8: Simulation results of the growth in 3D for silicon grains with (a, b) regular and (c, d) random orientations. The growth front morphology and orientations are visualized in (a, c). The roughness of the growth front surfaces is manifested by phase-field mobility in (b) and (d), which include the grain-grain-liquid and grain-grain-grain triple lines.

cases. The grains in Fig.3.8a orients their <100>, <110>, and <111> axes to the positive temperature gradient from the bottom to the top side. The boundary condition on the lateral sides is symmetric so that the grain boundaries in the middle of the domain can be more clearly manifested. The RGB color has been used to make it easy to distinguish the orientation.

The orientation of the grains in Fig.3.8c is randomly assigned to act as the comparison to the above case with regular orientations. Fig.3.8b and d show the phase-field mobility maps of the growth front surfaces and the triple lines (grain-grain-grain and grain-grain-liquid). The color of the phase-field mobility maps has been made transparent to make the triple lines visible. These results show that the grain structure in 3D is remarkably different from those in two dimensions, as the GBs are on longer 2D lines but 3D planes. The triple junction (point) between two solid grains and the melt in 2D becomes a grain-grain-liquid triple line in 3D. Moreover, the grain-grain-grain triple lines do not exist in 2D simulation and can hardly be observed even in the in-situ experiments.

3.4 Mechanisms of Grain Boundary Extension

To predict and control grain boundary (GB) development in multi-crystalline silicon, this study has developed a phase-field model capable of simulating the octahedral morphology of silicon grains and their growth with arbitrary orientations in both 2D and 3D. The simulated morphology of a single silicon grain (Fig.3.2) has been compared to experimental observations, yielding good agreement. Results in Fig.3.3 and 3.5 demonstrate how GB lines vary with steady-state growth rates. Additionally, Fig.3.4 and 3.5b showcase the response of GB lines to changes in the orientation relationship between two grains. By examining high (Fig.3.6) and low (Fig.3.7) growth rates, more types of GBs and resulting grain structures are

revealed. Furthermore, Fig.3.8 presents the growth of three grains in 3D, offering detailed insights into the realistic growth process of multi-crystalline silicon.

It is important to note that the current simulations focus on the influence of growth front surfaces on GB development, without considering the crystallographic interaction between grains, which is also significant in determining GB behavior. Nevertheless, the results indicate that growth front surfaces with anisotropic properties have a profound impact on GB development, as further discussed below.

3.4.1 Kinetic and energetic effects

As depicted in Fig.3.2 and 3.3, the growth behavior of both single grains and coupled grains can be significantly influenced by the cooling conditions. In the case of a single silicon grain (Fig.3.2), experimental and simulation results demonstrate that as the temperature increases and undercooling decreases, the faceted surfaces undergo a transition at sharp corners, turning out to be curved surfaces. Before 5.5 s, when the undercooling is high, the migration speed of the atomically smooth surfaces is considerably slower than that of the atomically rough surfaces. Consequently, the facets expand their flat regions and converge at sharp corners. However, as the undercooling decreases at 5.5 s, rough surfaces emerge on the silicon grain due to the diminishing difference in migration speed between rough and smooth surfaces. From an energetic perspective, the high-specific-energy sharp corner is replaced by a low-specific-energy curved surface. Thus, the morphology of the single silicon grain is primarily controlled by the kinetic effect initially and subsequently by the energetic effect. Similarly, in the case of GB development depicted in Fig.3.3 and 3.5a, there is a transition from kinetic-controlled growth to energetic-controlled growth, which consequently affects the extension direction of the GB. When the growth rate is high, the GB line almost follows the bisector

of the two facets of the groove. When the growth rate is low, the groove is shallow and has two rough surfaces. Because the left rough surface in the groove is close to the <001> orientation and the right rough surface is close to the $<11\bar{1}>$ orientation, the interface energy of the left surface is larger than that of the right one. The extension direction of the GB is then dragged to the left side according to the force balance between the two front surfaces.

Fig.3.4 and 3.5b show the GB lines change with the orientation relationship between the coupled gains. They have been compared with the bisectors of the groove facets. The bisectors come from the vector sum of the surface velocity by assuming the magnitudes of the velocities of the two facets are equal. Since the bisector rule simply considers the kinetic effect of the front surfaces, the slight deviation from the bisector suggests that the energetic effect may still play a role even when the growth is controlled by the kinetic effect. It has been affirmed by the results in Fig.3.4c, f and Fig.3.5b, in which most GB lines can match with the bisectors when the anisotropic surface energy is removed in the simulation. It should be noted that for the rotation angle of 10° in Fig.3.5b, the one with isotropic surface energy also deviates from the bisector. In this case, the groove is shallow and the facet does not appear. The bisector rule is not applicable to this case because the magnitudes of the velocities of the two groove surfaces are not equal.

In summary, the bisector rule is not enough for predicting the development of GBs between two misoriented grains. The development of GBs can be estimated precisely only by considering the contributions from both kinetic and energetic effects, which vary with orientation as described by the anisotropic functions in Fig.3.1. Our phase-field model which intrinsically incorporates these two types of anisotropic surface properties is indispensable in predicting the development of the GB once the model parameters and coefficients in the anisotropic functions

can be further refined in future work.

3.4.2 Transformation of groove surfaces

As Fig. 3.6 and 3.7 show the 2D simulation results including 10 grains with random orientation, the grain structure evolution involves the development of more possible GBs, including the ones with curved boundary lines. Fig. 3.6c shows the phase-field mobility maps of the growth front of the curved GB line in Fig.3.6a at different growth heights. Just after the two grains meet at 68s, the surfaces of the groove are both faceted. The GB extends between these two facets and tends to align with the temperature gradient. However, the left faceted surface does not last long and disappears as the growth continues. A new groove consisting of rough (left) and faceted (right) surfaces forms. Subsequently, the GB turns to be inclined to the left side. In the other case, Fig.3.7c shows the growth process of the curved GB in Fig.3.7a. In the beginning (2.0 - 70.0 s), the groove surfaces shows the faceted feature and GB has a minor right inclination. At the late stage (180.0 - 360.0 s), the area of the left faceted surface shrinks and the right rough surface extends. Then the extension direction of the GB turns to have less inclination and is almost parallel to the temperature gradient.

It becomes clear that the curved GB line results from the transformation of groove surfaces during the growth of coupled grains. The properties of the surfaces in the groove are directly related to the extension direction of the GB. The grooves in Fig.3.6c and 3.7c appear to be the facet-facet type in the beginning and then transform into a groove with non-facet surfaces. Unlike the facet-facet groove (Fig.3.4b) dominated by the kinetic effect and the rough-rough groove (Fig.3.3d) controlled by the energetic effect, the surfaces in these grooves cannot be simply designated as a facet or rough type because there is a range of transition between the smooth and rough surfaces. The extension direction of the GBs is determined

by the combined kinetic and energetic effects in these grooves with surfaces in the middle range. As it can be understood, the transformation of the groove surfaces is dependent on the orientation relationship and the cooling condition. During the growth of multiple grains with random orientations, the groove surface transformation and the elusive change of GB line should be usual events. The phase-field model demonstrates its capability of reproducing this transformation process for a given cooling condition and an arbitrary orientation relationship between two silicon grains.

3.4.3 Extension to 3D

The kinetic and energetic effects during GB development observed in the previous 2D results can still be found in the 3D results. In Fig.3.8a and b, because of the regular orientation of each grain, all grains grow with faceted surfaces, which form facet-facet pairs with adjacent grains. The inclined GB planes lead to the overgrowth of the grain with <111> orientation. As shown in Fig.3.8c and d, only one facet surface appears on one of the grains and all the other surfaces show the feature of rough surfaces. The GB beneath the facet-rough groove inclines and those beneath the rough-rough grooves have less inclination.

The necessity of extending the simulation of grain structure evolution and GB development to 3D lies in the realistic orientation relationship between grains. Only one rotation axis exists in two dimensions, while three rotation axes need to be considered in 3D. As it has been observed in 2D simulation, the curved GB line is found to be caused by the transformation of the groove surfaces, which largely depends on the orientation relationship of adjacent grains. Once the simulation domain is expanded to 3D, more possible orientation relationships will give rise to some rarely elucidated transformation cases of the groove surfaces and the resulting GBs. This is expected to open the door to elucidating the elusive process

of grain structure evolution in multi-crystalline silicon.

3.4.4 Limitations of current model

In this work, heat conduction has been excluded to speed up the numerical computation and enable 3D simulation of multiple grains, however, the effect of the latent heat may play a subtle role in affecting the kinetic growth of grooves surface even under low growth rate. Due to the crystallographic arrangement between the silicon grains, the grain boundary energy, which is assumed to be non-coherent and isotropic, should have cusps for specific orientations relationship and interact with the growth front surfaces in affecting the GB extension. Last but not least, the occurrence of twins, which has been frequently observed in experiments, can reconfigure groove surfaces and alter the GB extension. Overall, future work is to incorporate these physical effects in the current model by referring to the experimental evidence for elucidating the complex phenomena in the grain structure evolution of multi-crystalline silicon.

3.5 Conclusions

A developed three-dimensional phase-field model accurately captures the faceted morphology of silicon grains, grain boundary (GB) extension, and evolution of the grain structure. Through this model, it is determined that the direction of GB extension is influenced by the growth mode of the front surfaces, alternating between kinetic and energetic modes depending on the cooling rate and orientation relationship. This understanding is considered crucial for predicting GBs and the grain structure of multi-crystalline silicon. The multi-phase-field model utilized in this study exhibits promising potential for simulating the realistic solidification process of multi-crystalline silicon.

3.6 Appendix: Derivation of faceted anisotropy in phase-field model

For the case of anisotropic interface energy, the quadratic term in the Eq.(3.1) turns out to be,

$$\epsilon^2\nabla^2\phi \rightarrow \nabla[(\epsilon(\theta)^2\nabla\phi] + \sum_{p=x,y,z}\frac{\partial}{\partial p}\left[\epsilon(\theta)\frac{\partial\epsilon(\theta)}{\phi_p}|\nabla\phi|^2\right] \tag{3.10}$$

The gradient coefficient $\epsilon(\theta)$ is a function of the deviation angle from the 111 facets as expressed by Eq.3.6 and 3.8. To avoid the singularity at the minimum of the cusp, Eq.3.8 is converted by adding a rounding parameter ρ to the trigonometric functions. It then turns to be a function with the following form,

$$a(\theta) = \mu[1 + \zeta(C + \tan(\alpha_0)S)] \tag{3.11}$$

$$C = \sqrt{\cos^2\theta + \rho^2} \tag{3.12}$$

$$S = \sqrt{\sin^2\theta + \rho^2} = \sqrt{1 - \cos^2\theta + \rho^2} \tag{3.13}$$

The angle between the normal vector of the faceted surface and the normal vector of a local surface can be determined by the cross-product of the unit vectors of these two normal vectors. Take the case of <111> faceted surface as an example, the unit vectors are,

$$\vec{n} = (n_x, n_y, n_z) = \frac{1}{|\nabla\phi|}(\phi_x, \phi_y, \phi_z) \tag{3.14}$$

$$\vec{n}_{111} = \frac{1}{\sqrt{3}}(1,1,1) \tag{3.15}$$

in which ϕ_x, ϕ_y, ϕ_z are the partial derivatives of phase field ϕ and the aliases of $\partial\phi/\partial x$, $\partial\phi/\partial y$, $\partial\phi/\partial z$.

The cosine of the angle between them is then obtained.

$$\cos\theta = \vec{n} \cdot \vec{n}_{111} = \frac{\phi_x + \phi_y + \phi_z}{\sqrt{3}|\nabla\phi|} \tag{3.16}$$

$$|\nabla\phi| = \sqrt{\phi_x^2 + \phi_y^2 + \phi_z^2} \tag{3.17}$$

If the crystal is rotated about a particular axis, the normal vector of the <111> faceted surface should also be rotated using Rodrigues' rotation formula:

$$\vec{n'}_{111} = \vec{n}_{111}\cos\Theta + (\vec{k} \times \vec{n}_{111})\sin\Theta + (\vec{k} \cdot \vec{n}_{111})\vec{k}(1 - \cos\Theta) \tag{3.18}$$

in which the $\vec{k}$ is the unit vector denoting the rotation axis and Θ is the rotation angle. Following the chain rule of derivative, the two terms in Eq.3.10 can be expanded as,

$$\nabla(\epsilon(\theta)^2\nabla\phi) = \epsilon(\theta)^2\nabla^2\phi + 2\epsilon(\theta)\sum_{p=x,y,z}(\frac{\partial\epsilon(\theta)}{\partial p}\frac{\partial\phi}{\partial p}) \tag{3.19}$$

$$\sum_{p=x,y,z}\frac{\partial}{\partial p}\left[\epsilon(\theta)\frac{\partial\epsilon(\theta)}{\phi_p}|\nabla\phi|^2\right]=\epsilon_0^2\sum_{p=x,y,z}\left\{\frac{\partial a(\theta)}{\partial p}\frac{\partial a(\theta)}{\partial\phi_p}|\nabla\phi|^2+ a(\theta)\frac{\partial}{\partial p}(\frac{\partial a(\theta)}{\phi_p})|\nabla\phi|^2+ a(\theta)\frac{\partial a(\theta)}{\partial\phi_p}\frac{\partial}{\partial p}(|\nabla\phi|^2)\right\} \tag{3.20}$$

The derivatives of $a(\theta)$ to p and ϕ_p can then be written as,

$$\frac{\partial a}{\partial p}=\mu\zeta(\frac{\partial C}{\partial p}+\tan\alpha_0\frac{\partial S}{\partial p}) \tag{3.21}$$

$$\frac{\partial a}{\partial\phi_p}=\mu\zeta(\frac{\partial C}{\partial\phi_p}+\tan\alpha_0\frac{\partial S}{\partial\phi_p}) \tag{3.22}$$

Also, the consecutive derivative to ϕ_p and p can be expanded as,

$$\frac{\partial}{\partial p}(\frac{\partial a}{\partial\phi_p})=\mu\zeta\frac{\partial}{\partial p}(\frac{\partial C}{\partial\phi_p}+\tan\alpha_0\frac{\partial S}{\partial\phi_p}) \tag{3.23}$$

$$\frac{\partial}{\partial p}(\frac{\partial C}{\partial\phi_p})=\frac{\partial}{\partial p}(\frac{\cos\theta}{C}\frac{\partial\cos\theta}{\partial\phi_p}) \tag{3.24}$$

$$\frac{\partial}{\partial p}(\frac{\partial S}{\partial\phi_p})=-\frac{\partial}{\partial p}(\frac{\cos\theta}{S}\frac{\partial\cos\theta}{\partial\phi_p}) \tag{3.25}$$

It can be figured out that all the derivatives in Eqs.3.23, 3.24, 3.25 can be related to the $\partial\cos\theta/\partial p$, $\partial\cos\theta/\partial\phi_p$. Thus, all the derivatives in Eq.3.10 can be replaced by the spatial derivatives of the phase field ϕ, which can be easily implemented in the numerical methods.

References

[1] J. A. Dantzig and M. Rappaz, *Solidification*. EPFL Press, 2009. 1, 2, 2.2.1, 2.2.4, 3, 4.2.1, 5.1

[2] D. A. Porter, K. E. Easterling, and M. Y. Sherif, *Phase transformations in metals and alloys*. CRC press, 2009. 1, 2.2.1, 2.3.4, 3

[3] K. Fujiwara, L.-C. Chuang, and K. Maeda, "Dynamics at crystal/melt interface during solidification of multicrystalline silicon," *High Temperature Materials and Processes*, vol. 41, no. 1, pp. 31–47, 2022. 1.2.1, 3.1, 3.2.3

[4] P. Wang, C. Cui, D. Yang, and X. Yu, "Seed-assisted growth of cast-mono silicon for photovoltaic application: challenges and strategies," *Solar Rrl*, vol. 4, no. 5, p. 1900486, 2020. 1.2.1, 3.1

[5] T. Duffar and A. Nadri, "The grain–grain–liquid triple phase line during solidification of multi-crystalline silicon," *Comptes Rendus Physique*, vol. 14, no. 2-3, pp. 185–191, 2013. 2.1, 3.1, 3.3.2

[6] K.-K. Hu, K. Maeda, H. Morito, K. Shiga, and K. Fujiwara, "In situ observation of grain-boundary development from a facet-facet groove during solidification of silicon," *Acta Materialia*, vol. 153, pp. 186–192, 2018. 3.1

[7] L.-C. Chuang, K. Maeda, H. Morito, K. Shiga, W. Miller, and K. Fujiwara, "Effect of misorientation angle of grain boundary on the interaction with $\sigma 3$ boundary at crystal/melt interface of multicrystalline silicon," *Materialia*, vol. 7, p. 100357, 2019. 3.1

[8] T. Jain, H. Lin, and C. Lan, "Three dimensional modelling of grain boundary interaction and evolution during directional solidification of multi-crystalline silicon," *Journal of Crystal Growth*, vol. 485, pp. 8–18, 2018. 3.1

[9] R. Prakash, K. Jiptner, J. Chen, Y. Miyamura, H. Harada, and T. Sekiguchi, "Grain boundary interactions in multicrystalline silicon grown from small randomly oriented seeds," *Applied Physics Express*, vol. 8, no. 3, p. 035502, 2015. 3.1, 3.3.3

[10] B. Gallien, T. Duffar, S. Lay, and F. Robaut, "Analysis of grain orientation in cold crucible continuous casting of photovoltaic si," *Journal of Crystal Growth*, vol. 318, no. 1, pp. 208–211, 2011. 3.1

[11] D. W. Hoffman and J. W. Cahn, "A vector thermodynamics for anisotropic surfaces: I. fundamentals and application to plane surface junctions," *Surface Science*, vol. 31, pp. 368–388, 1972. 3.1

[12] X. Yang, K. Fujiwara, K. Maeda, J. Nozawa, H. Koizumi, and S. Uda, "Crystal growth and equilibrium crystal shapes of silicon in the melt," *Progress in Photovoltaics: Research and Applications*, vol. 22, no. 5, pp. 574–580, 2014. 3.1, 3.2.2, 3.3.1, 3.2

[13] A. K. Boukellal, A. K. S. Elvalli, and J.-M. Debierre, "Equilibrium and growth facetted shapes in isothermal solidification of silicon: 3d phase-field simulations," *Journal of Crystal Growth*, vol. 522, pp. 37–44, 2019. 2.2.4, 3.1, 3.2.2

[14] K. Fujiwara, Y. Obinata, T. Ujihara, N. Usami, G. Sazaki, and K. Nakajima, "Grain growth behaviors of polycrystalline silicon during melt growth processes," *Journal of crystal growth*, vol. 266, no. 4, pp. 441–448, 2004. 3.1, 3.3.2

[15] H. Lin and C. Lan, "Revisiting the twinning mechanism in directional solidification of multi-crystalline silicon sheet," *Acta Materialia*, vol. 131, pp. 1–10, 2017. 3.1

[16] G. Cantù, A. Popescu, and W. Miller, "Grain growth of silicon," *Acta materialia*, vol. 60, no. 19, pp. 6755–6761, 2012. 3.1

[17] W. Miller, A. Popescu, and G. Cantù, "Solidification of multicrystalline silicon–simulation of micro-structures," *Journal of Crystal Growth*, vol. 385, pp. 127–133, 2014. 3.1

[18] W. Miller and A. Popescu, "Micro structures in the grain evolution during solidification of silicon: phase field calculations," *Acta Materialia*, vol. 140, pp. 1–9, 2017. 3.1

[19] A. Tandjaoui, N. Mangelinck-Noel, G. Reinhart, B. Billia, T. Lafford, and J. Baruchel, "Investigation of grain boundary grooves at the solid–liquid interface during directional solidification of multi-crystalline silicon: in situ characterization by x-ray imaging," *Journal of crystal growth*, vol. 377, pp. 203–211, 2013. 1.1, 3.1

[20] I. Steinbach, "Phase-field models in materials science," *Modelling and simulation in materials science and engineering*, vol. 17, no. 7, p. 073001, 2009. 1.1, 2, 2.2.1, 2.2.2, 2.2.5, 3.1, 3.2.1, 3.2.3, 4.2.2, 5.2.1, 5.5

[21] H. Salama, J. Kundin, O. Shchyglo, V. Mohles, K. Marquardt, and I. Steinbach, "Role of inclination dependence of grain boundary energy on the microstructure evolution during grain growth," *Acta Materialia*, vol. 188, pp. 641–651, 2020. 3.1, 3.2.1

[22] T. Takaki, T. Hirouchi, Y. Hisakuni, A. Yamanaka, and Y. Tomita, "Multi-phase-field model to simulate microstructure evolutions during dynamic recrystallization," *Materials transactions*, vol. 49, no. 11, pp. 2559–2565, 2008. 3.1, 3.2.1

[23] G. McFadden, A. Wheeler, R. Braun, S. Coriell, and R. Sekerka, "Phase-field models for anisotropic interfaces," *Physical Review E*, vol. 48, no. 3, p. 2016, 1993. 3.2.2

[24] R. Qin and H. K. D. H. Bhadeshia, "Phase-field model study of the effect of interface anisotropy on the crystal morphological evolution of cubic metals," *Acta Materialia*, vol. 57, pp. 2210–2216, 2009. 3.2.2, 4.4.2

[25] J. J. Eggleston, G. B. McFadden, and P. W. Voorhees, "A phase-field model for highly anisotropic interfacial energy," *Physica D: Nonlinear Phenomena*, vol. 150, no. 1-2, pp. 91–103, 2001. 3.2.2

[26] H. Lin, C. Chen, and C. Lan, "A simple anisotropic surface free energy function for three-dimensional phase field modeling of multi-crystalline crystal growth," *Journal of crystal growth*, vol. 362, pp. 62–65, 2013. 3.2.2

[27] S. Torabi, J. Lowengrub, A. Voigt, and S. Wise, "A new phase-field model for strongly anisotropic systems," *Proceedings of the Royal Society A: Mathematical, Physical and Engineering Sciences*, vol. 465, no. 2105, pp. 1337–1359, 2009. 3.2.2

[28] S. Torabi and J. Lowengrub, "Simulating interfacial anisotropy in thin-film growth using an extended cahn-hilliard model," *Physical Review E*, vol. 85, no. 4, p. 041603, 2012. 3.2.2

[29] P. Apte and X. Zeng, "Anisotropy of crystal-melt interfacial free energy of silicon by simulation," *Applied Physics Letters*, vol. 92, no. 22, p. 221903, 2008. 3.2.2

[30] J. Debierre, A. Karma, F. Celestini, and R. Guérin, "Phase-field approach for faceted solidification," *Physical Review E*, vol. 68, no. 4, p. 041604, 2003. 2.2.4, 3.2.2

[31] N. Wang, M. Upmanyu, and A. Karma, "Phase-field model of vapor-liquid-solid nanowire growth," *Physical Review Materials*, vol. 2, no. 3, p. 033402, 2018. 3.2.2

[32] J. Eiken, M. Apel, S. Liang, and R. Schmid-Fetzer, "Impact of p and sr on solidification sequence and morphology of hypoeutectic al–si alloys: Combined thermodynamic computation and phase-field simulation," *Acta Materialia*, vol. 98, pp. 152–163, 2015. 3.2.2

[33] Y. Song, D. Tourret, F. Mota, J. Pereda, B. Billia, N. Bergeon, R. Trivedi, and A. Karma, "Thermal-field effects on interface dynamics and microstructure selection during alloy directional solidification," *Acta Materialia*, vol. 150, pp. 139–152, 2018. 3.2.3

[34] M. Tokairin, K. Fujiwara, K. Kutsukake, N. Usami, and K. Nakajima, "Formation mechanism of a faceted interface: In situ observation of the si (100) crystal-melt interface during crystal growth," *Physical Review B*, vol. 80, no. 17, p. 174108, 2009. 3.2.3

Chapter 4

Complex Dual-phase Eutectic

The solidification of alloy materials is involved with the solute redistribution owing to the limited solubility in the solid solution. When the solute concentration of the liquid is large enough, the grains of both solute and solvent may appear and grow in the liquid. The so-called "eutectic" consists of two solid phases that are poor and rich in solute concentration. During solidification, the two phases grow in a coupled manner (Fig.1.1b), by which the solute is redistributed more efficiently. Typically, the microstructure of eutectic may either has a layer-by-layer (lamellar) or rod-in-matrix pattern, which mainly depends on the fractions of the two phases. The spacing or the fineness of the dual-phase structure can be controlled by regulating the cooling rate. As the cooling rate is high, the solid front grow at a high velocity. The time for the solute redistribution is short, as a result, the two solid phases may adapt to small spacing and a fine pattern may form. When the cooling rate is high, conversely, the dual-phase pattern should be coarse. The spacing of the eutectic pattern is a critical characteristic that is directly related to the material properties. The scaling rule of the lamellar spacing has been established by Jackson and Hunt [1]. Although the theory is for regular eutectic growth, it provides the foundation for understanding the pattern formation of irregular eutectic, of which at least one phase is comprised of faceted

crystal.

If the grains of one of the eutectic phases grow with faceted surfaces, the interaction between the crystallographic anisotropy and the solute distribution may give rise to complicated eutectic patterns, which can no longer be predicted by the classic theory. The numerical method plays a critical role in shedding light on the pattern formaiton of eutectic with faceted crystals. In this chapter, a phase-field study has been conducted to obtain an understanding of the formation mechanism of the script lamellar pattern of $MoSi_2/Mo_5Si_3$ eutectic composite, which is a promising candidate for high-temperature structural application. The spacing of the lamellar pattern in the simulation results shows good agreement with that of experimental observations and analytical solutions under three growth velocities: 10 mm/h, 50 mm/h, and 100 mm/h. The discontinuity of Mo_5Si_3 rods, in contrast to the regular eutectic with a continuous pattern, is claimed to be caused by the instability of the solid-liquid interface. In this study, the implementation of Mo_5Si_3 nucleation over the solid-liquid interface has been proposed and successfully reproduced the discontinuity characteristic. A highly random and intersected lamellar pattern similar to that observed in the ternary $MoSi_2/Mo_5Si_3$ eutectic alloyed with 0.1 at% Co has been obtained in simulation owing to the increase in the frequency of nucleation. In addition, it has been demonstrated that the inclination of the Mo_5Si_3 rod can be reproduced by taking into account the strong relaxation of lattice strain energy due to formation of ledge-terrace structure.

4.1 Script Lamellar Pattern of $MoSi_2/Mo_5Si_3$ Eutectic

$MoSi_2$-based alloys have been considered promising candidates for high-temperature structural applications owing to their high melting point, good oxidation resis-

tance, and relatively low density [2, 3, 4, 5]. Directionally-solidified $MoSi_2/Mo_5Si_3$ spontaneous composite is of particular interest because of its better creep property than other $MoSi_2$-based composites [6, 7]. However, its fracture toughness at room temperature is still insufficient for practical application. As this shortage is believed to be overcome by microstructure refinement and morphology control [7, 8], it is quite important to elucidate the formation mechanism of the $MoSi_2/Mo_5Si_3$ microstructure, which has an exotic eutectic pattern, the so-called script lamellar pattern (Fig.1.4a). In this study, the phase-field method has been firstly used to reveal the underlying physics during the solidification process of $MoSi_2/Mo_5Si_3$ eutectic.

The process of eutectic solidification, in which the liquid phase transforms into at least two solid phases simultaneously, has been extensively studied. The cornerstone theory for understanding eutectic growth was established by Jackson and Hunt [1]. The theory pointed out the interplay between the diffusion effect and interface tension. It is stated that for a given cooling rate, a steady-state spacing of eutectic lamellae shall be realized by the balance of solute undercooling and curvature undercooling, reaching a minimum value of total undercooling. Thus, this theory provides a guideline for predicting the lamellar spacing and regulating the fineness of lamellar structure by adjusting the cooling rate.

Moreover, the morphologies of eutectics are determined by the crystallographic properties of the solid phases. For example, the coupling of a facet and a non-facet phase gives rise to the formation of irregular eutectic structures, having random, discontinuous phase distribution [9]. Furthermore, the anisotropy in the interfacial energy of the solid-solid interface can lead to a large variety of unique and intriguing eutectic morphologies [10]. A noticeable characteristic of the $MoSi_2/Mo_5Si_3$ eutectic microstructure is the discontinuity of the Mo_5Si_3 rods embedded in the $MoSi_2$ matrix, which is similar to that for the typical irregular

eutectic pattern of Al-Si (Fig.1b in [9]) alloy. The mechanism of discontinuous pattern in irregular eutectics was investigated by experimental observation. It has been found that the solid-liquid interface has an uneven and unstable morphology (Fig.1d in [9]) and is in a non-isothermal state. This instability of the interface is mainly because the facet phase cannot follow the growth of the non-facet matrix; thus, it cannot form a stable coupled growth. In contrast to the non-faceted interface of Al crystal with metallic bonds, the Si crystal with covalent bonds tends to form faceted interface by growing along a specific crystallographic direction [11], exhibiting strong anisotropy of interface mobility. The preferential growth direction of each Si grain relative to the temperature gradient is random and determined by its initial orientation at the stage of nucleation. Therefore, the Si grains with random growth directions keep being overgrown by the matrix Al-phase and emerging as nuclei, causing an instability of the solid-liquid interface. Analogously, there is no doubt that the solid-liquid interface of $MoSi_2/Mo_5Si_3$ eutectic with the discontinuous pattern is also unstable during the directional solidification, principally owing to the directional bonding of the intermetallic compound.

Another irregular characteristic of the $MoSi_2/Mo_5Si_3$ script lamellar pattern is the inclined solid-solid interface relative to the temperature gradient. The inclination phenomenon of the eutectic pattern has been previously reported in the literature [12, 13]. Generally, inclined patterns can be induced by the effect of either diffusion or interface energy anisotropy. The inclination induced by diffusion occurs in thin-film samples or two-dimension simulations. When the solute diffusion is limited compared to the growth rate, eutectic lamellae grow at an angle with respect to the direction of the temperature gradient for the sake of facilitating solute exchange between the two coupled phases. The inclination angle is determined by the balance of the growth rate and diffusion rate. In the

case of another effect, i.e., anisotropy in interface anisotropy, the inclined interface is fixed to a direction determined by the crystallographic relationship between the two coupled phases. For $MoSi_2/Mo_5Si_3$ eutectic, a ledge-terrace structure has been observed at the inclined interface by high-resolution TEM (Fig.1.4b), which is a sign of lattice accommodation for reduction of elastic energy. Therefore, the inclination of $MoSi_2/Mo_5Si_3$ interface is much more likely to be caused by the anisotropy of solid-solid interface energy. However, the influence of diffusion cannot completely be excluded, and a rigorous discussion is needed to figure out the main factor for the inclined morphology.

Accordingly, the possible formation mechanisms of the irregular and complex $MoSi_2/Mo_5Si_3$ script lamellar pattern are: (I) formation of discontinuous rods led by the instability of the solid-liquid interface; (II) interface inclination caused by anisotropy of the solid-solid interface energy; (III) interface inclination induced by diffusion in the liquid. It is important to examine the contribution of these factors to the control of microstructure and the improvement of mechanical properties. In the present study, the roles of these factors in the formation of the script lamellar structure are examined in the following steps: Firstly, a regular eutectic solidification model is constructed. The front undercooling at steady state extracted from the two-dimension phase-field simulation results needs to be compared with that in the analytical results, which has direct correlations to material properties. The PF model should also be able to reproduce the spacing transition phenomena observed in the experiment and predicted by theory [1]. Secondly, the two-dimension model is extended to a three-dimension one in order to output microstructure images comparable to experimental results in [7]. Then, nucleation functionality is incorporated into this eutectic model. It is assumed that nucleation is a representation of solid-liquid interface instability, which is responsible for the pattern discontinuity. Finally, in order to find out

the primary factor that determines the inclined morphology of the script lamellar pattern, another phase-field model with anisotropic interface energy is developed. In combination with the experimental evidence, attempts are made to obtain an anisotropic description of the solid-solid interface energy. Overall, the simulation results of these steps are expected to provide a new perspective to understand the eutectic solidification process of the $MoSi_2/Mo_5Si_3$ intermetallic composite.

4.2 Analytical and Numerical models

4.2.1 Jackson-Hunt theory

The following analytical method for coupled growth of eutectic lamellae was proposed by Jackson and Hunt [1] and adapted by Dantzig et al.[14]. Starting with the Gibbs-Thomson equation, the interface undercooling can be given as,

$$\Delta T_{\text{interface}} = \Delta T_{\text{curvature}} + \Delta T_{\text{solute}} \tag{4.1}$$

which sums up the curvature undercooling and solute undercooling without consideration of the kinetic undercooling on the assumption of a low solidification rate. By solving the diffusion equation and averaging the curvature of the eutectic front, Jackson and Hunt derived the undercooling with relation to the growth velocity μ and the lamellar spacing λ for a binary eutectic system as,

$$\Delta T = A_1 \frac{\nu}{D_l} \lambda + A_2 \frac{1}{\lambda} \tag{4.2}$$

in which A_1 and A_2 are coefficients with relation to thermodynamic and interface properties, such as phase equilibrium, fusion entropy, and interface energy. The detailed properties of $MoSi_2/Mo_5Si_3$ eutectic system are listed in Table 4.1. They can be expressed as,

$$A_1 = \frac{\Delta C_0}{g_\alpha g_\beta} \frac{|m_{l\alpha}||m_{l\beta}|}{|m_{l\alpha}| + |m_{l\beta}|} \sum_{n=1} \frac{\sin^2(\mathrm{n}\pi \mathrm{g}_\alpha)}{(n\pi)^3} \tag{4.3}$$

$$A_2 = \frac{|m_{l\alpha}||m_{l\beta}|}{|m_{l\alpha}| + |m_{l\beta}|} \left(\frac{2\gamma_{\alpha l} \cos\theta_\alpha}{|m_{l\alpha}| g_\alpha \Delta S_{\alpha l}} + \frac{2\gamma_{\beta l} \cos\theta_\beta}{|m_{l\beta}| g_\beta \Delta S_{\beta l}} \right) \tag{4.4}$$

For three different cooling rates (10 mm/h, 50 mm/h, and 100 mm/h), the interface undercooling is plotted as a function of lamellar spacing. These plots act as the baselines for examining the validity of the eutectic phase-field model specified below.

4.2.2 Phase-field model of dual-phase growth

Phase-field equation governs the microstructure evolution and is derived by the variational differentiation of the total free energy, based on the principle of energy minimization. The total free energy can be described as the sum of chemical energy, interfacial energy, elastic energy. By using physical properties evaluated by other approaches, such as the CALPHAD method, First Principle calculation or experimental measurement, it is possible to perform quantitative or quasi-quantitative phase-field simulation [15, 16].

The commercially available software MICRESS (version 6.300) [17], based on the multi-phase-field framework [18], has been used for conducting a phase-field simulation of eutectic solidification. Three non-conservative order parameters (ϕ_0, ϕ_1, ϕ_2) were assigned for liquid, $MoSi_2$, and Mo_5Si_3 phases fields, and one conservative order parameter c was assigned for Si concentration in the eutectic system. The phase-field equation governing the interface kinetics is expressed as,

$$\frac{\partial \phi_\alpha}{\partial t} = \sum_{\beta=1}^{v} M_{\alpha\beta}\left[\sigma_{\alpha\beta}(\nabla^2\phi_\alpha - \nabla^2\phi_\beta) + \frac{\pi^2}{2\eta^2}(\phi_\alpha - \phi_\beta) + \frac{\pi}{\eta}\sqrt{\phi_\alpha\phi_\beta}\Delta G_{\alpha\beta}\right] \quad (4.5)$$

in which the evolution of phase α is the result of interaction with all surrounding phases. $M_{\alpha\beta}$, $\sigma_{\alpha\beta}$ and $\Delta G_{\alpha\beta}$ are interface mobility, interface energy and driving force between two phases of α and β. The artificially large interface width η is used in the simulation for computation efficiency and set to be three times the grid size for proper interface resolution. The driving force can be expressed as,

$$\Delta G_{\alpha\beta} = \Delta S_{\alpha\beta}\Delta T(c) \quad (4.6)$$

$\Delta S_{\alpha\beta}$ is the fusion entropy between α and β phase. $\Delta T(c)$ is the difference between the actual temperature in the system and the liquidus temperature for the concentration c. The diffusion equation controlling the solute redistribution in solid and liquid phases can be written as

$$\frac{\partial c}{\partial t} = \nabla(\sum_{\alpha=1}^{v} \phi_\alpha D_\alpha \nabla c_\alpha) \quad (4.7)$$

in which c_α and D_α are the concentration field and the diffusion coefficient in the α phase, respectively. The physical properties of $MoSi_2/Mo_5Si_3$ eutectic system in this phase-field model are the same as those used in the analytical method (see Table 4.1).

For 2D simulation, the mesh number of the box in the height direction is set as 200 with a grid size of 0.1 μm. The interface width is 3 times the grid size, which is the lower limit for resolution. With a single pair of lamellae in the box, the lamellar spacing can be set by changing the mesh number of the box in the width direction. In the case of 3D simulation extended from the 2D model, the mesh

Table 4.1: Physical parameters used in analytical and phase field model.

Item	Symbol	Value	Unit
Liquids Slope	$m_{l\alpha}$	-3100	K
	$m_{l\beta}$	1800	K
Liquid concentration	C_l	54.0	at.%
Concentration Difference of solid phases	ΔC_0	0.28	
Phase fraction (α-Mo_5Si_3, β-$MoSi_2$)	g_α	0.393	
	g_β	0.607	
Contact angle	θ_α	$3\pi/8$	
	θ_β	$3\pi/8$	
Fusion entropy	ΔS	5×10^6	$J/(Km^3)$
Diffusivity in liquid	D_l	2.45×10^{-8}	m^2/s
Interface energy	$\gamma_{\alpha l}$, $\gamma_{\beta l}$	1.0	J/m^2

number of the box is 50×50×100 with a grid size of 0.4 μm. The interface has the same number of grids as the 2D model. The boundary condition of lateral sides for all the simulations is periodic and that of the bottom is symmetric for both phase field and concentration field. While the boundary condition on the top side varies according to the field type and solidification condition. The phase field is symmetric while the concentration field is set as "fixed" at the top boundary. This fixed value is either manually given as 54% (the initial concentration of liquid) or solved in an external 1D diffusion domain. Additionally, in order to eliminate the effect of the top boundary on the solute distribution in the liquid, the eutectic front keeps a distance from it by using the moving frame technique.

The version of Micress (Microstructure Evolution Simulation Software) is 6.300. It runs on the Windows 10 Home operation system of a virtual machine allocated with three cores of a 3.5 GHz 6-Core Intel Xeon E5 processor and 8 GB 1866 MHz DDR3 memory. For the 3D domain with a 50×50×100 mesh, the ratio of real solidification time to computational time is about 1:20000. The simulated microstructure pattern is visualized by an open-source software ParaView

(Kitware). For quantifying the eutectic structure, the lamellar spacing of both simulation and experiment images are analyzed by Fiji, an open-source image analysis package based on Image-J. The "particle analysis" is used to obtain the barycenter coordinate information of rods in the azimuthal (perpendicular to growth direction) cross-section. An algorithm programmed in MatLab is used to determine the distance to the nearest neighbor for one rod by calculating the distances to all the other rods and choosing the minimum value. This process was repeated one by one for each rod. The lamellar spacing is obtained by averaging the values of the nearest neighbor distances.

In addition, another multi-phase-field model with a different formulation incorporated with anisotropic interface energy is employed to examine the factors for interface inclination. For the convenience of implementation, the model is derived in a different formulation and uses a set of non-dimensionalized parameters (Table 4.2). The detailed derivation of this model is presented in [13]. In brief, the phase-field equation is given as

$$\frac{\partial \phi_\alpha}{\partial t} = \frac{2}{n}\sum_{j=1}^{v} M_{ij}\left[\sum_{k=1}^{n}\frac{1}{2}(\epsilon_{ik}^2 - \epsilon_{jk}^2)\nabla^2\phi_k + (W_{ik} - W_{jk})\phi_k - \frac{8}{\pi}\sqrt{\phi_i\phi_j}\Delta f_{ij}\right] \quad (4.8)$$

The parameters M_{ij}, ϵ_{ij}, W_{ij}, and Δf_{ij} are matrix quantities representing phase interactions between neighbor phases at interfaces. M_{ij} is the interface mobility, ϵ_{ij} is the gradient energy coefficient, W_{ij} is the magnitude of energy penalty for the interface, and Δf_{ij} is the driving force calculated from the chemical free energy difference between the two phases. For describing anisotropic interface energy, the coefficient ϵ_{ij} is set to be anisotropic and given as a function of interface normal angle θ. Thus, in the two-dimension coordinate system, the Laplacian terms $\epsilon_{ij}^2\nabla^2\phi_j$ in Eq.(4.5) are replaced by

$$\nabla[\epsilon(\theta)_{ij}^2 \nabla\phi_j] - \frac{\partial}{\partial x}[\epsilon(\theta)_{ij}\frac{\partial\epsilon(\theta)_{ij}}{\partial\theta_{ij}}\frac{\partial\phi_j}{\partial y} + \frac{\partial}{\partial y}[\epsilon(\theta)_{ij}\frac{\partial\epsilon(\theta)_{ij}}{\partial\theta_{ij}}\frac{\partial\phi_j}{\partial x}] \tag{4.9}$$

The following two anisotropy functions of ϵ coefficient with different features are used in the present work,

$$\epsilon(\theta) = 1 - \delta\cos[\mathrm{k}(\theta + \theta_0)] \tag{4.10}$$

$$\epsilon(\theta) = 1 - \delta\exp\big[-\frac{\sin^2(\theta + \theta_0)}{w^2}\big] \tag{4.11}$$

The parameters δ, k, θ_0, and w in these functions are used to adjust the shape of their polar plots. The values of interface inclination resulting from introducing these different anisotropy functions are compared to discuss the anisotropy property of the interface.

Table 4.2: Parameters used in the phase-field model with anisotropic interface energy.

Item	Symbol	Value	Unit
Gas constant	R	8.314	J/(K·mol)
Grid size	L_0	4×10^{-8}	m
Temperature	T_0	1000	K
Molar volume	V_0	7×10^{-6}	m^3/mol
Interface energy	γ	0.5	J/m^2
Interface width	δ	$7.0\times L_0$	
mobility	m	1.0	[-]

4.3 Growth Simulation of Regular Eutectic without Anisotropy

4.3.1 Analysis of interface undercooling

The 2D simulation box is illustrated in Fig.4.1: a positive linear temperature gradient is distributed from the left to the right side; the domain is cooled by moving this gradient at a constant velocity. After reaching a steady state, a pair of lamellae, with a value of spacing equal to the box width, grows in a constant velocity equal to that of the temperature gradient. Both of the PF model and the JH model use the same set of physical parameters listed in Table 4.1. The parameters related to phase diagram are extracted from thermodynamic data in [19]. Based on the empirical rule that the fusion entropy per mole should be larger than 2R (R is the gas constant) for facet crystal like Molybdenum, the fusion entropy is around the value of 1.7×10^{6} $J\cdot K^{-1}\cdot m^{-3}$. Some experimental measurement has estimated the interface energy of Molybdenum to be around $0.8J/m^{2}$[20]. Considering the highly ordered crystallographic structure of both $MoSi_2$ and Mo_5Si_3 phases, the fusion entropy and interface energy are preliminarily determined as 5×10^{6} $J\cdot K^{-1}\cdot m^{-3}$ and 1.0 $J\cdot m^{-2}$. By reference to the diffusivity of Silicon in aluminum which is in the order of -8[21], the diffusivity of Silicon in Molybdenum is determined as 2.45×10^{-8} m^2/s by manually changing the value of diffusivity in this order until the spacing in simulation results become nearly consistent with that of experiment results. However, it is not guaranteed that this set of parameters can be the actual representative of the $MoSi_2/Mo_5Si_3$ eutectic system. The determination of these parameters is still in discussion.

In Fig.4.2, for three steady-state interface velocities (10 mm/h, 50 mm/h, 100 mm/h), the interface undercooling results from PF simulation (circles interpo-

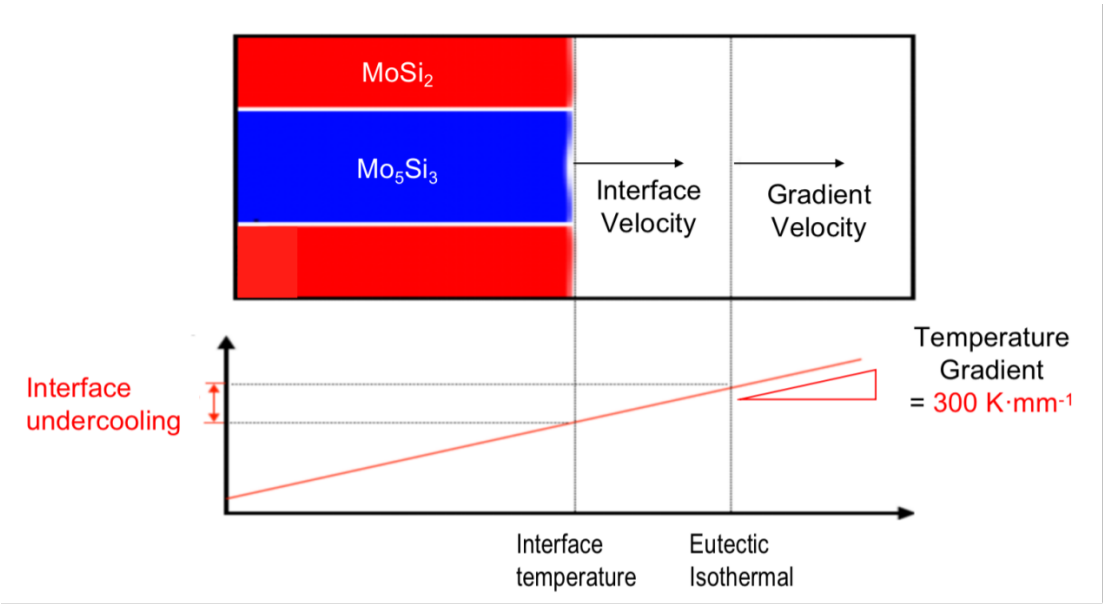

Figure 4.1: Schematic image of simulation box and temperature profile in two dimensions. The domain is cooled by moving the temperature gradient at a constant velocity. The interface undercooling reaches a stable value when the interface velocity equals to the gradient velocity at steady state.

Table 4.3: Comparison of extreme spacing results from Jackson-Hunt (JH) solution and two-dimension phase-field (PF) simulation.

Interface velocity (mm/h)	10	50	100
Extreme spacing (JH) (μm)	8.00	3.60	2.40
Extreme spacing (PF) (μm)	8.80	3.20	2.80
Deviation	10.0%	11.1%	16.7%

lated by dash lines) are plotted together with the Jackson-Hunt (JH) analytical solutions (solid lines). The curves of PF results are found to have the same valley-like shape as the JH solutions. The values of extreme lamellar spacing (denoted by arrows) from PF results are close to those from JH results for every growth velocity. As summarized in Table 4.3, the deviations between them vary in the range of 10% to 17%. However, the extreme undercooling in PF results is obviously larger than that in JH results. This is because the kinetic undercooling is neglected in the derivation of Eqs.4.1 and 4.2. However, this difference does not matter for the relatively low cooling rate in our cases. The kinetic effect is less important than the interaction between diffusion and interface tension, which determines the length scale of the eutectic structure. By the undercooling comparison above, the phase-field model is able to be put into further development for simulating the spacing transition phenomenon of the lamellar structure.

4.3.2 Spacing transition

Spacing transition phenomenon has been experimentally observed in transparent eutectic alloy [1] and also simulated by numerical methods [22]. The lamellar structure will be unstable when their spacing deviates far from the extreme condition for a given steady state growth velocity. It tends to have a more stable spacing through a transition process. In order to reproduce this process on the basis of the previously developed eutectic model with a single pair of lamellae,

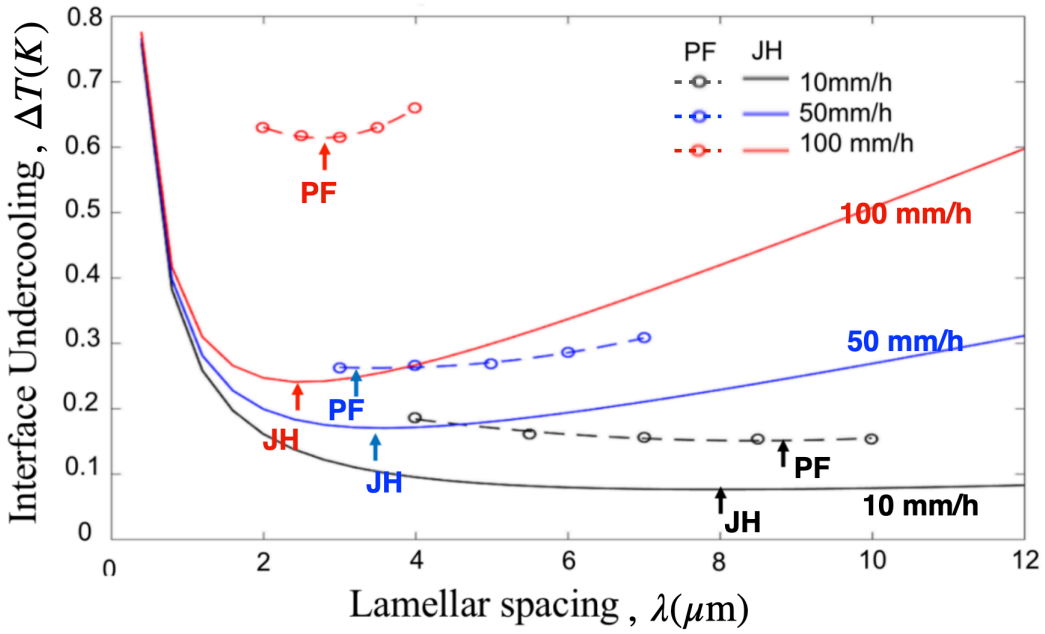

Figure 4.2: Comparison of interface undercooling between phase-field (dash lines) and Jackson-Hunt (solid lines) results at three interface velocities (10 mm/h, 50 mm/h, 100 mm/h).

we extend it to the case of multiple pairs with various magnitudes of spacing. In Fig.4.3, all the PF simulations were performed at the growth velocity of 100 mm/h, corresponding to the JH solution denoted by the red line in Fig.4.2. As Fig.4.3b shows, when the initial spacing (2.5 μm) is close to the extreme spacing (2.4 μm) denoted in Fig.4.2, although there is a small fluctuation at the beginning of the growth, all the lamellae survive and grow in a steady state eventually. In Fig.4.3a, the initial spacing (0.625 μm) is much smaller than the extreme spacing. Right after the start, some lamellae are overgrown by adjacent ones. As a result, the lamellar spacing transforms to be near the extreme spacing. In Fig.4.3c, the initial lamellar spacing is very large, and the lamellae eventually grow in an inclined angle. This instability phenomenon attracts our particular attention. The inclination observed here is surely not caused by the interface energy anisotropy, which is not included in the model. The main reason is claimed to be the spatial restriction in the two-dimension box. When the 2D model in Fig.4.3c is extended to a 3D one, as shown in Fig.4.3d,e, the rod phase in the center splits into several branches, resulting in the reduction of the spacing and the stabilization of the lamellar structure.

By analyzing the solute distribution ahead of the eutectic front in Fig.4.3c, more insights into the space-restricted instability can be obtained. Basically, the solute-rich phase and solvent-rich phase of eutectic need solute and solvent atoms for their growth, respectively. The atoms are redistributed by diffusion ahead of the solid-liquid interface. Owing to the large initial lamellar spacing, the element rejected by one phase cannot easily transport to the adjacent counter phase. The element exchange between the coupled phases is limited, resulting in the massive accumulation or depletion of the solute concentration, as indicated by the concentration contrast ahead of the interface in Fig.4.3c. As a result, the interface forms a concave shape, which is the initial stage of splitting. However,

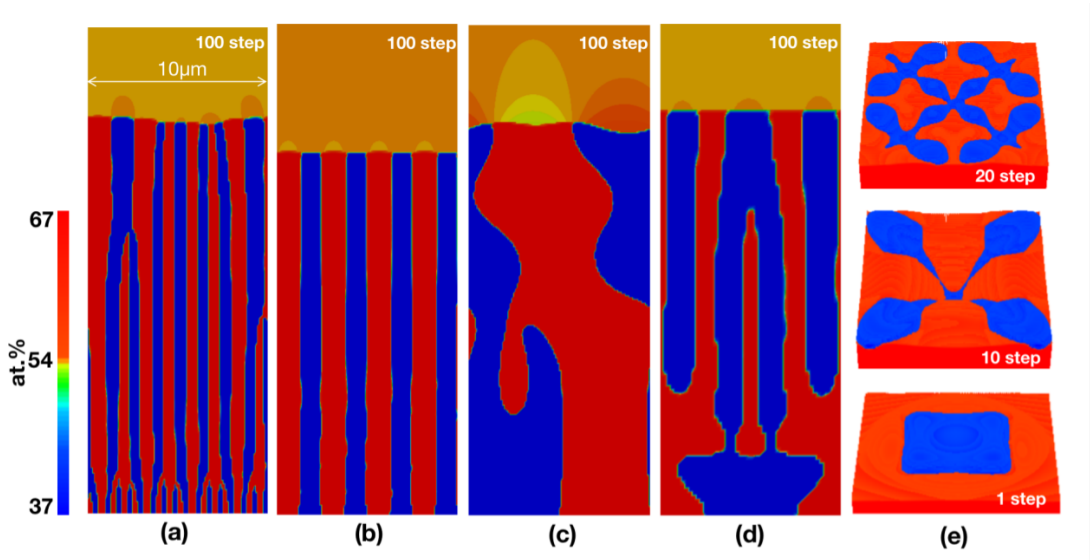

Figure 4.3: Simulation results generated by concentration field showing spacing transition for different value of initial lamellar spacing λ_{ini}= (a) 0.625, (b) 2.5, (c)(d)(e) 10 μm. (a) After some rods are overgrown in the beginning, the steady-state spacing becomes larger. (b) All lamellae can survive and spacing keep unchanged. (c) Lamella grow in an inclined angle and spacing keeps fluctuating. (d)(e) In the 3D model extended from (c), an initial single rod splits into several rods.

due to the geometrical limitation of the two-dimension box, the splitting in the case of 3D simulation (Fig.4.3d,e) cannot develop. For the sake of alleviation of the concentration accumulation or depletion, the lamellae grow at an inclined angle to facilitate the solute redistribution. From the examination above, this model is expected to produce eutectic microstructure agreeing well with the experimental and theoretical study [1] and act as a robust basis for further investigation of the influence of interface instability on the pattern continuity.

4.3.3 Eutectic growth in three dimensions (3D)

The simulation of microstructure in three dimensions (3D) has been conducted. Since the initial nuclei in the simulation box are dense and have very small mutual distance, the lamellar spacing in each velocity increases as the solid-liquid interface moved forward. In Fig.4.4, the 3D simulation boxes at steady state (first row), their cross-section images of growth direction (second row) and the corresponding experimental results (third row) are compared. In the simulation results, it can be discerned that higher growth velocity gives rise to finer microstructure in accordance with the experimental results. Fig.4.5 compares the lamellar spacing in experiments, JH solution, and PF simulation. All results show the similar decreasing tendency of lamellar spacing as growth velocity increases, but the difference between them is still noticeable. As summarized in Table 4.4, under three interface velocities (10 mm/h, 50 mm/h, 100 mm/h), the values of lamellar spacing in PF simulation deviate from the experimentally measured ones in the range of 21% to 30%. This suggests that the physical parameters we have chosen still have shortages and can be further optimized. Moreover, a significant number of preceding studies have confirmed that realistic eutectics grow within a range near the extreme condition, rather than precisely at the extreme condition with lowest undercooling [23, 24]. Thus, by choosing more appropriate parame-

ters, the deviations can be diminished but may not be eliminated completely. On the other hand, Fig.4.4 shows the pattern in simulation results is visually similar to that of experiment images having flat solid-solid interfaces and inclined rods. The reproduced similarity might be unexpectedly caused by the incorporation of a four-fold anisotropy or due to the computational mesh effect. The effect of anisotropy of solid-solid interface energy will be briefly discussed in another phase-field model afterward.

Table 4.4: Comparison of lamellar spacing results from experiment and three-dimensional phase-field (PF) simulation.

Interface velocity (mm/h)	10	50	100
Lamellar spacing (Exp.) (mum)	8.98	4.58	3.95
Lamellar spacing (PF) (mum)	6.31	3.61	2.93
Deviation	29.8%	21.1%	25.7%

4.4 Growth Simulation of Irregular Eutectic with Anisotropy

4.4.1 Lamellar discontinuity

As mentioned in the Introduction, the solid-liquid interface instability during solidification contributes to the discontinuous lamellar pattern. Basically, this instability involves the emergence of new growth sites of the Mo_5Si_3 rod phase. The manner of generating new growth sites can be either branching or nucleation ([22], Fig.8). Owing to the accumulation of rejected solute atoms, the concaves of a lamella interface are formed. Subsequently, the undercooling in the concave for the counter phase becomes larger, making it possible for the nucleation. Despite the fact that there is still no evidence to exclude the branching mechanism of Mo_5Si_3

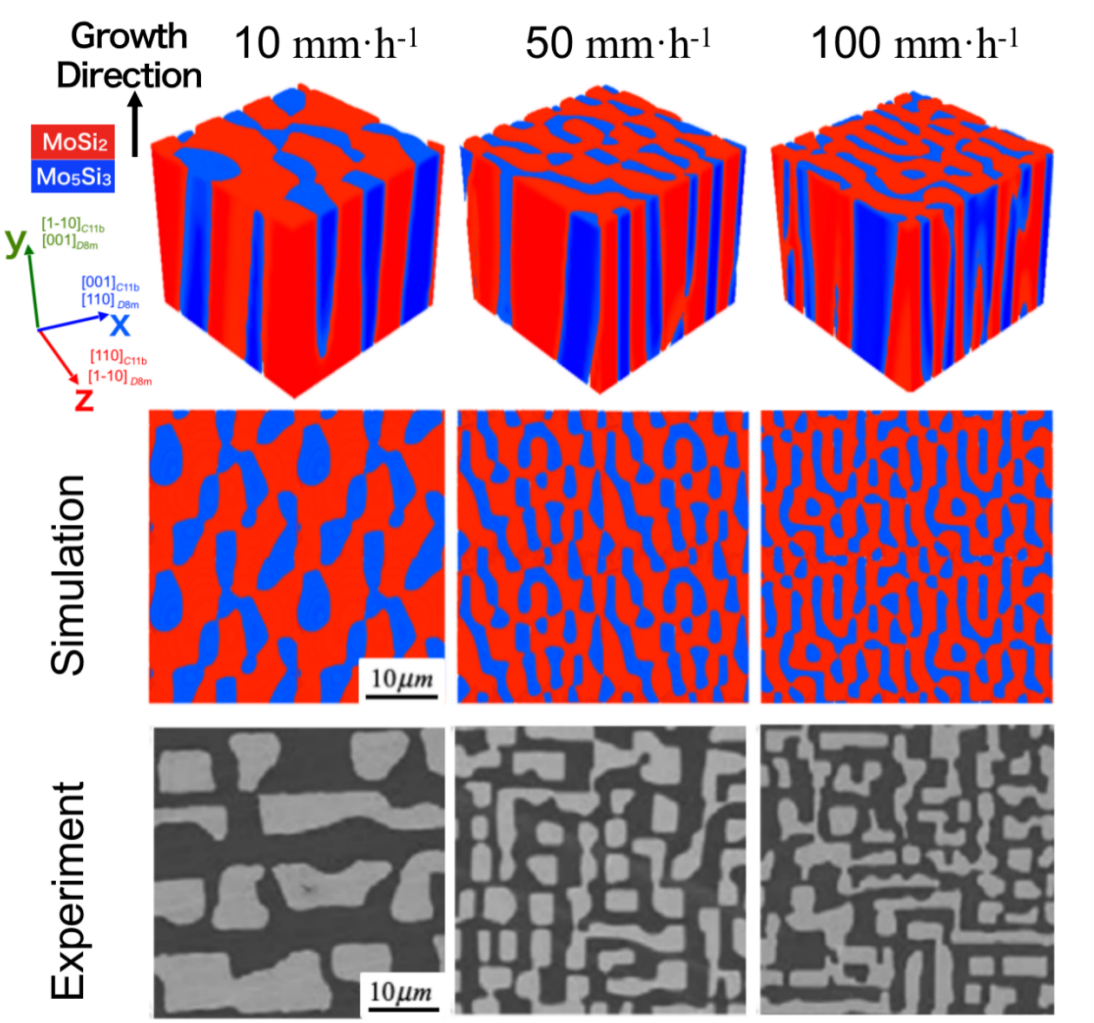

Figure 4.4: Comparison of microstructure between phase-field simulation results (upper row: 3D bird view, center row: twice mirrored images of horizontal cross-section) and experimental results (after Matsunoshita et al. [7]) for three growth rates of 10 mm/h(left), 50 mm/h (center) and 100 mm/h(right).

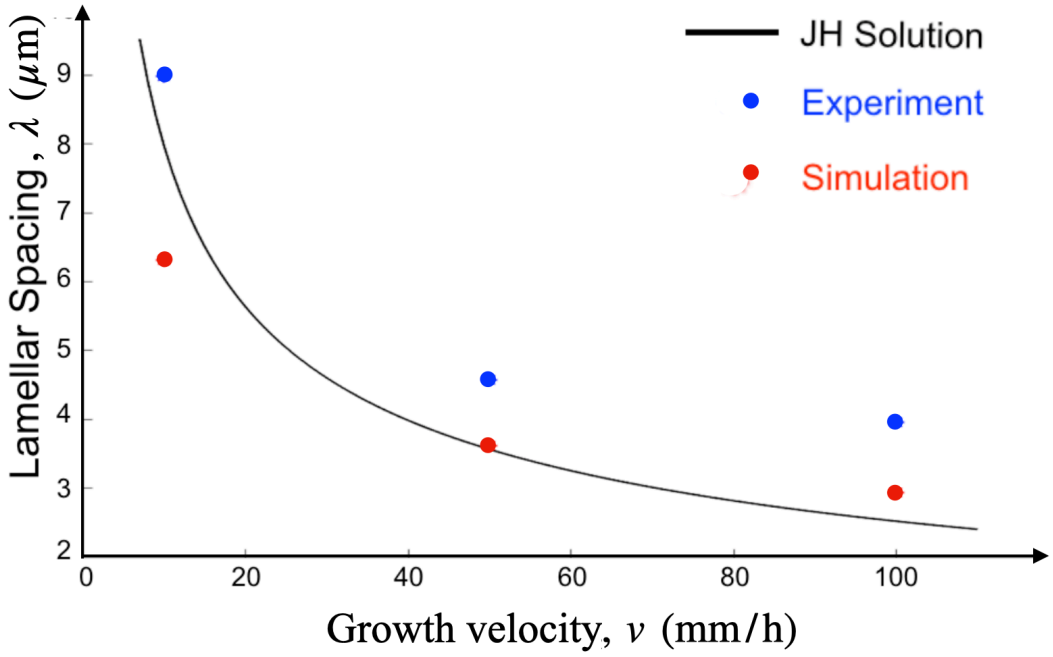

Figure 4.5: Comparison of lamellar spacing evaluated from Jackson-Hunt solution, experiment and phase field simulation. All of them show the same decreasing tendency as the interface velocity increases.

phase, in this study, nucleation is considered as a representation of the interface instability. This assumption is reasonable mainly because there is undercooling ahead of the eutectic front. The incorporation of successive nucleation over the solid-liquid interface is expected to facilitate an understanding of how interface instability affects pattern continuity.

Three cases of simulation have been performed to investigate the effect of nucleation under the growth velocity of 200 mm/h. In Case 1, it is assumed that no nucleation occurred. Fig.4.6 shows the 3D simulation domain, horizontal cross-sections, the graph of evolving lamellar spacing, and the longitudinal cross-section. It can be observed that right from the start, the spacing remains to be relatively stable. Later on, the spacing goes up as some rods are overgrown by the matrix. Eventually, the spacing reaches a larger, relatively stable value. Next, in Case 2, as shown in Fig.4.7, nucleation is introduced. For every 0.05 second, one nucleus is put at a place over the solid-liquid interface where there has the largest undercooling. It should be noted that although the temperature is uniform over the interface, the concentration is inhomogeneous and contributes to the varying undercooling over the interface. As a result, the discontinuity is reproduced seeing from the longitudinal cross-section image (Fig.4.7d), and the insight of the formation mechanism can be obtained from the graph of spacing-time in Fig.4.7c. After an initial ascending, the lamellar spacing keeps fluctuating over a long period of time. This sinusoidal-like variation of spacing is the consequence of alternate dominance of nucleation and overgrowth: right after a new nucleus appears over the interface, the spacing decreases because of the increased number of rods. The newly-formed crystal should have a random orientation. But due to the high temperature gradient and large anisotropy of interface mobility, the nuclei with unfavorable orientation cannot develop into grains with visible size. Thus, these unfavorable nuclei are neglected in this simulation. Later on, the new nucleus

with favorable orientation grows further into a rod, then replaces or merges with the adjacent rods; subsequently, the number of rods decreases and the spacing increases. The repetition of this process gives rise to the fluctuation of lamellar spacing and the discontinuity of the pattern. Finally, in Case 3, the frequency of nuclei addition is increased to every 0.02 second. As shown in Fig.4.8a-c, the resulting pattern becomes more discontinuous and even intersected. In Fig.4.8d, the 3D rods extracted from the box clearly shows the nucleation of Mo_5Si_3 phase and its interconnected structure. It is worth noting that nucleation frequencies in both Case 2 and Case 3 are relatively low such that the nuclei do not affect the growth velocity or the temperature over the interface, which is evidenced by observing the temperature profile in the simulation boxes during growth of Case 1-3. This suggests that the nuclei-induced dominance of nucleation and overgrowth proposed above is reasonable. Last but not least, it is interesting that a microstructure pattern similar to the Case 3 has been observed experimentally (Fig.4.8e) in the $MoSi_2/Mo_5Si_3$ eutectic with a ternary composition of Mo-54at.%Si-0.1at.% Co [8].

It can be claimed that the origin of the interface instability is due to the complex crystal structure for both $MoSi_2$ and Mo_5Si_3 phases. In a crystallographic analysis [8], $MoSi_2$ and Mo_5Si_3 have body-centered tetragonal structures with the types of C11b and D8m, respectively. The $(1\bar{1}0)$ plane of $MoSi_2$ and (001) plane of Mo_5Si_3 are found to be nearly perpendicular to the temperature gradient or growth direction. The formation of this set of crystallographic orientations is basically attributed to the directional bonding of intermetallic compounds. These compounds have a high degree of order after the reorganization from the liquid state (i.e., solidification), and atoms can only attach to the interface to form bonds with the crystal along well-defined crystallographic orientation, resulting in a high anisotropy of interface mobility. Accordingly, the two phases cannot

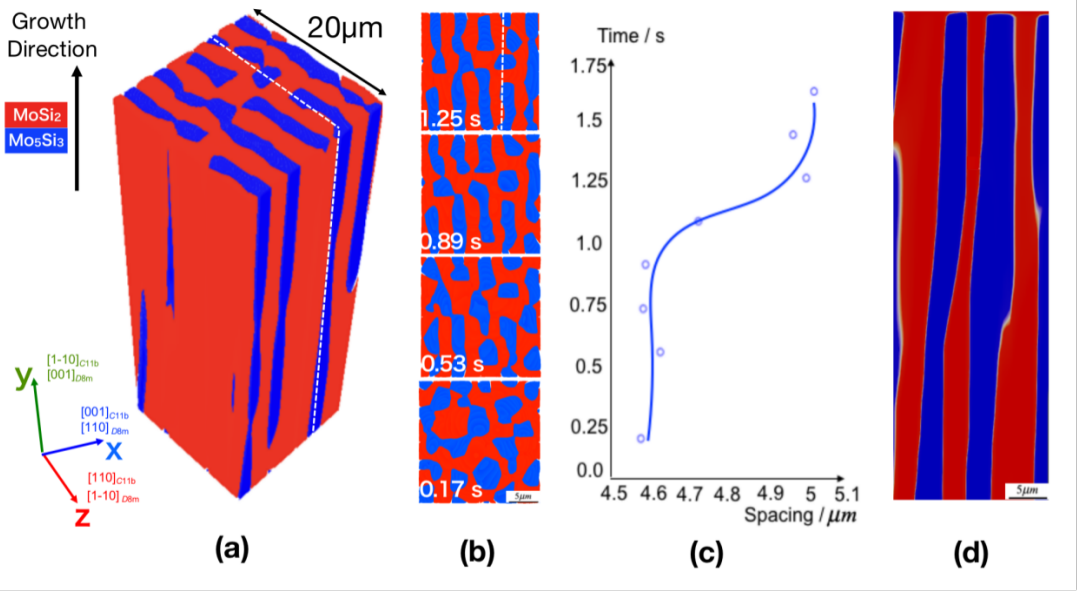

Figure 4.6: Results of three-dimension simulation without nucleation. (a) Mo_5Si_3 rod (blue) or lamellae in the $MoSi_2$ matrix (red); (b) the microstructure of cross section is evolving along with time; (c) lamellar spacing keeps relatively stable at the beginning, then becomes larger and reaches a steady state; (d) The longitudinal cross section shows continuous lamellar structure.

grow in a coupled manner even with a slight difference of the interface mobility along the growth directions. Therefore, persistent interface instability occurs during the solidification process, acting as the basis of our assumption of successive nucleation ahead of the solid-liquid interface. In addition, the nucleation process may be influenced by the alloying element. Similar to the result in Fig.4.8, it has been reported that a very small amount of Cr (typically 0.1mass%) to Al-Zn significantly reduces the grain size by changing the nucleation condition. The mechanism involves the transformation from icosahedral short-range order (ISRO) in the liquid to quasicrystals, which implies smaller interface energy and lower nucleation barrier [25, 26].

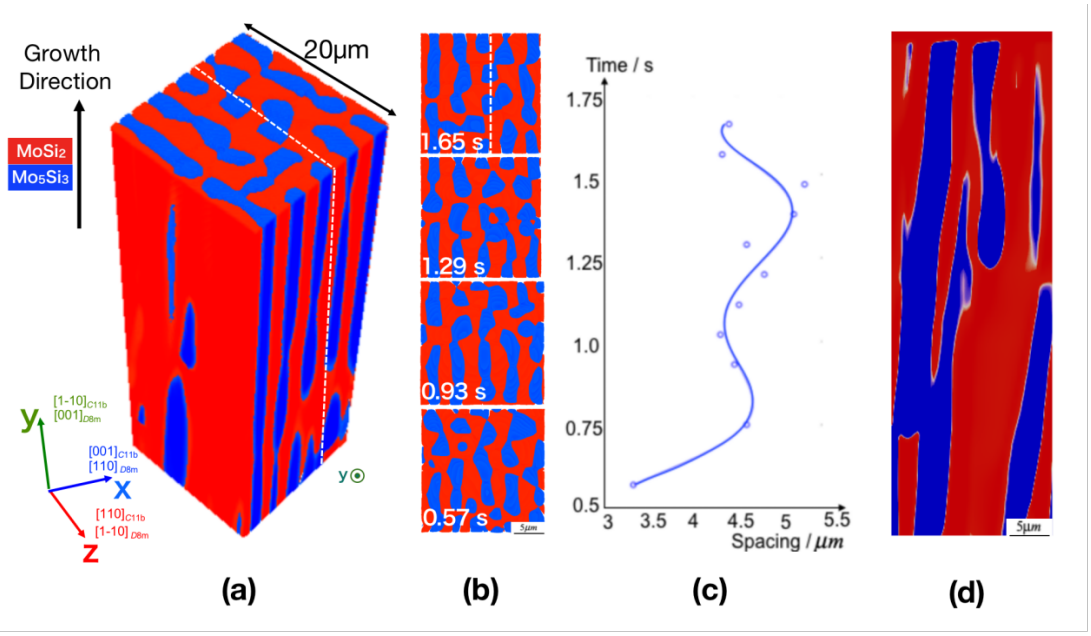

Figure 4.7: Results of nucleation-introduced three-dimension simulation. The frequency of nucleation is at 20 s^{-1} (one nucleus per 0.05s). (a) Mo_5Si_3 rod (blue) or lamellae in the $MoSi_2$ matrix (red); (b) the microstructure of the cross-section is evolving along with time; (c) after a short ascending in the beginning, the lamellar spacing keep fluctuating over a long period; (d) longitudinal cross-section (dash line area in (a)) shows discontinuous lamellar structure.

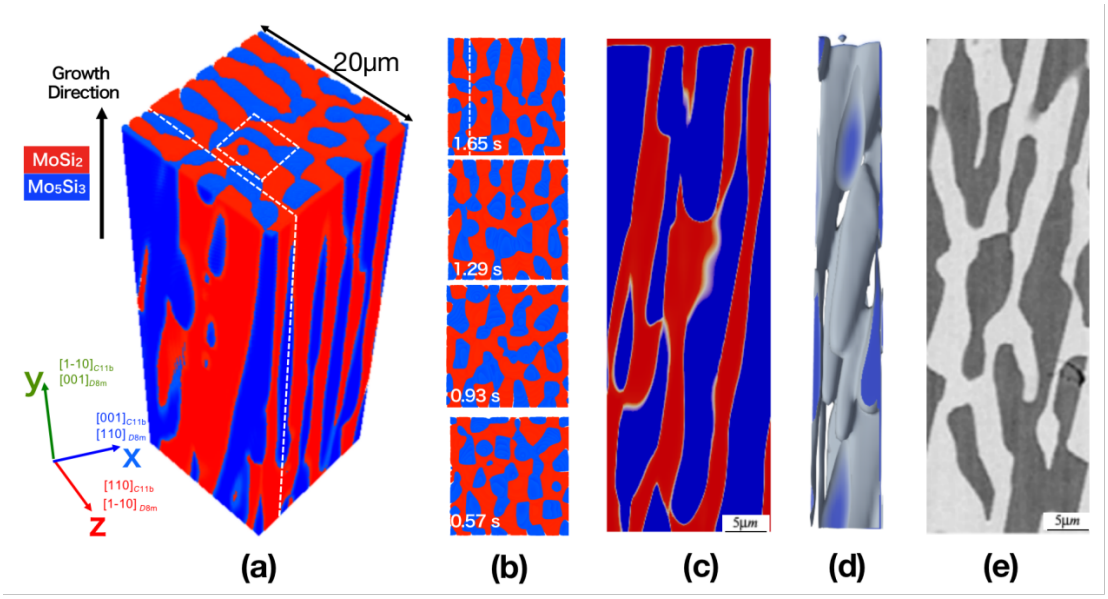

Figure 4.8: Results of nucleation-introduced three-dimension simulation. The frequency of nucleation is increased to 50 s^{-1} (one nucleus per 0.02s). (a-c) the simulated pattern became more discontinuous and intersected; (d) 3D rods extracted from the dash square area in (a) demonstrates the nucleation of Mo5Si3 phase and the replacement of old grain by new one; (e) Experimentally observed pattern in $MoSi_2/Mo_5Si_3$ eutectic alloyed with 0.1 at.% Co (after Fujiwara et al. [8]).

4.4.2 Misfit accommodation at interphase boundary

In Fig.1.4 (after Fujiwara et al.[8]), we can see the Mo_5Si_3 rod in the $MoSi_2$ has a cuboidal shape with four flat interfaces, a pair of which is inclined from the growth direction. As expected by Wulff' s construction [27, 28], the equilibrium shape should have the lowest surface energy. Thus, knowing the shape of the Mo_5Si_3 rod, it is straightforward to construct a corresponding anisotropic function of $MoSi_2/Mo_5Si_3$ interface energy. As schematically illustrated in Fig.4.9a, a similar cuboidal equilibrium shape is enveloped in an anisotropy function with four cusps. It should be noted that the anisotropic function also has an inclination, corresponding to the interface inclination. In Fig.4.9b, a 2D plot (Eq.(4.10)) with inclined cusps represents the anisotropy of interface energy on the vertical cross-section. In order to get a complete description of the interface energy anisotropy, the remaining questions concerning the specifications of the 2D anisotropy function are the following two: "What is the inclination angle?", "How deep should the cusp be?"

To answer the first question, crystallographic analysis and experimental observation should be considered. Based on lattice parameters at the eutectic temperature (1900°C), as illustrated in Fig.4.10, the mismatch between the two crystals of $MoSi_2$ and Mo_5Si_3 can be eliminated by the formation of ledge-terrace structure with a set of the atomic arrangement parameters, including the inclination angle θ having a value of 13.9° [7]. In the experimental observation by high-resolution TEM (Fig.1.4b), there is also a ledge-terrace structure at the interface, which has an inclination angle of 13.5°, almost equal to the analysis result. This consistency between analysis and experiment confirms that the inclined $MoSi_2/Mo_5Si_3$ interface has the lowest lattice strain energy and corresponds to the cusp in the anisotropy function constructed in Fig.4.9b. Therefore, the inclination angle of the function is determined to be 13.5°, the same value as experimental measure-

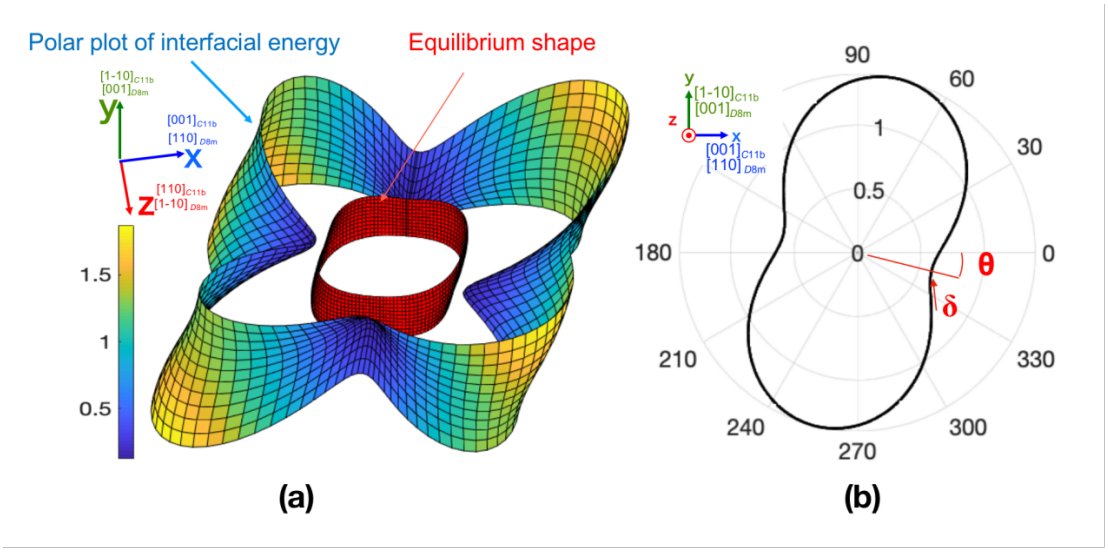

Figure 4.9: Anisotropic description of the $MoSi_2/Mo_5Si_3$ interface energy based on the characteristics of the script lamellar pattern. (a) 3D surface of anisotropic function with cusps and its equilibrium shape inside; (b) plot of a two-dimension anisotropic function which is a reduced and simplified version of the 3D surface. It also has cusps which can give rise to the inclined interfaces. θ is the inclination angle and δ is the anisotropic strength.

ment. Also, it is worth noting that the interface with anisotropic energy we are referring to is the macroscopic interface on the micrometer scale rather than the ledge or terrace interface on the nanometer scale. In the present study, the interface energy includes both components of elastic energy due to the coherency (i.e., due to crystallographic structure) and chemical energy due to interatomic bonding (i.e., electronic structure).

Having already constructed a cusp anisotropy function with a 13.5° inclination angle, we want to know if this anisotropy representation of the interface energy can enable the interface to grow precisely at the 13.5° angle. Our tool is the phase-field model constructed from Eqs.4.8 and 4.9 with anisotropic interface energy specified by the anisotropy functions (Eqs.4.10, 4.11). The initial condition of the microstructure has three phases with a triple junction and three interfaces. As shown in Fig.4.11a, the solid/solid interface has anisotropic interfacial energy (AIE) expressed by Eq.4.10, and the other two (i.e., liquid/$MoSi_2$ interface and liquid/Mo_5Si_3 interface) have isotropic interface energy (IIE). Since the model is based on the principle of energy minimization, it is expected that the AIE will result in the formation of $MoSi_2$/Mo_5Si_3 interface along the orientation perpendicular to the cusps. However, there is a force equilibrium at the triple junction, and therefore, the inclination angle of the interface deviates from the angle expected from the AIE. This indicates that the cusp needs to be deeper than a critical value, i.e., the AIE needs to be strong enough, to be able to form an interface with an inclination angle expected from the cusp of AIE.

As shown in Fig.4.11a, the cusps are shallow or nearly flat, the interface only inclines in a small angle of 4.0°, being much smaller than 13.5°. After increasing the anisotropic strength and deepening the cusp (Fig.4.11b), the resulting inclination becomes larger and increases to 5°, still being far below 13.5°. These results confirm that the liquid-solid interface does affect the inclination angle, and

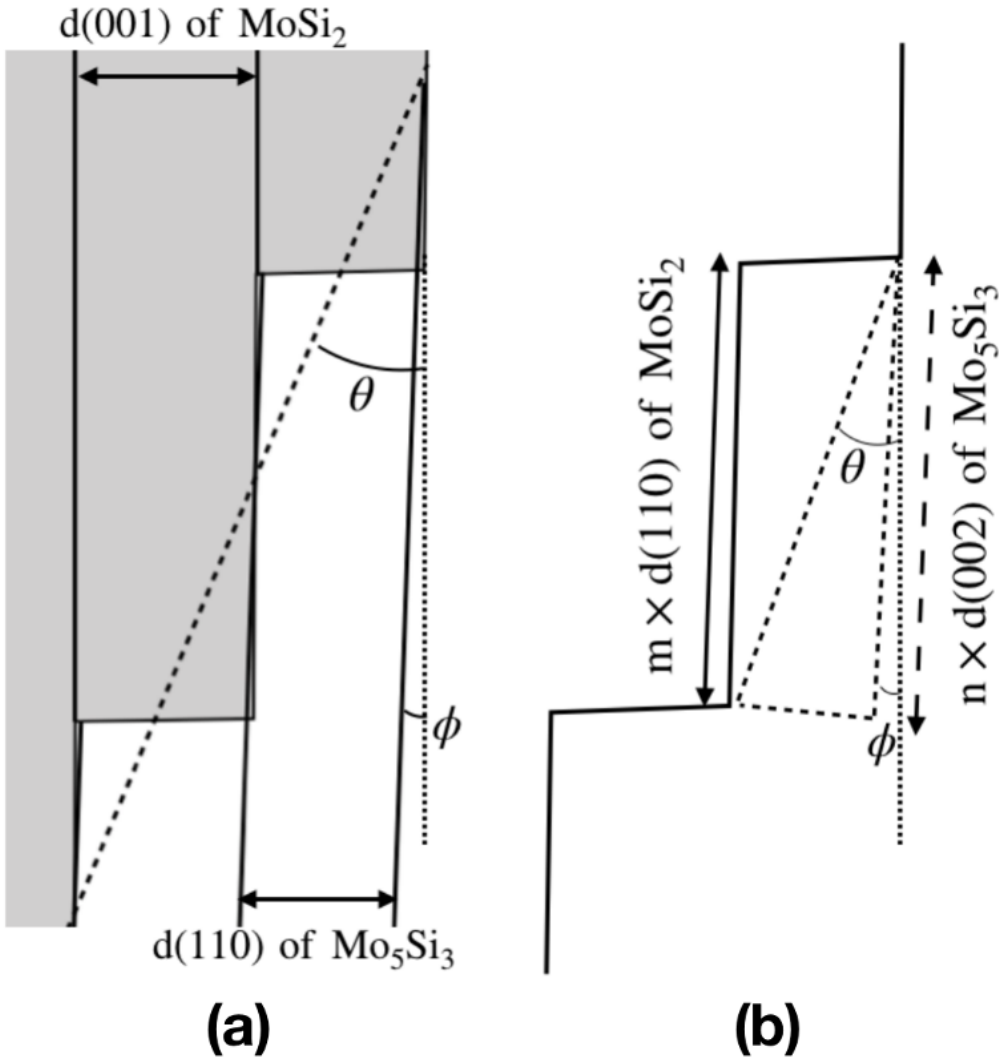

Figure 4.10: Schematics of lattice misfit accommodation by the formation of ledge-terrace structure. (a) elimination of the ledge misfit between (001) of $MoSi_2$ and (110) of Mo_5Si_3 by a rotation of angle ϕ; (b) elimination of terrace misfit between (110) plane of $MoSi_2$ and (002) plane of Mo_5Si_3 by insertion of dislocations. The resulting inclination of interface is denoted by angle θ. See Ref. [7] for the details of this crystallographic analysis.

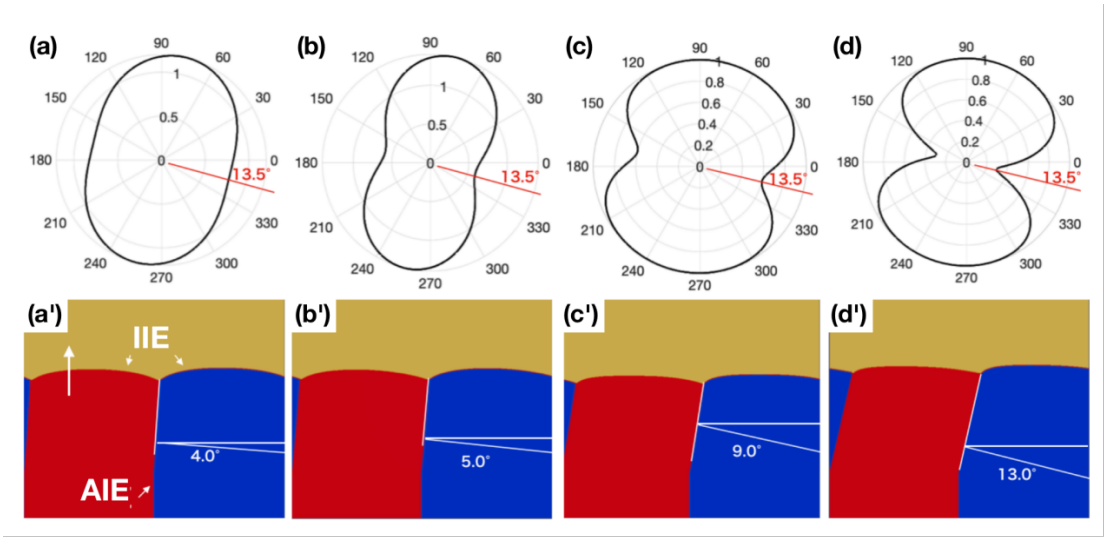

Figure 4.11: (a-d) Four types of two-fold anisotropy functions used to investigate the effect of cusp depth on the inclination angle of the solid-solid interface, and (a' -d') corresponding simulation results: (a,a') δ=0.2 in Eq.10, (b, b') δ=0.4 in Eq.4.10, (c,c') δ=0.4, w=0.4 in Eq.4.11, (d,d') δ=0.7, w=0.4 in Eq.4.11.

increasing the anisotropy strength will make the inclination angle closer to the expected value. Next, we use another anisotropy function (Eq.4.2) with sharper cusps. In Fig.4.11c, the resulting angle of the interface is 9.0°, being relatively close to 15°. After further increasing the strength in Fig.4.11d, the angle increases to be 13.0^{circ}, nearly at the value of 13.5°. However, when the anisotropy strength is further increased, numerical instability occurs, and no convergence of the inclination angle can be reached.

The crystallographic analysis demonstrates that the significant lattice misfit can be eliminated by forming a ledge-terrace structure, which has also been observed in the experiment. The results of the inclination angle and atomic arrangement in analysis and experiment are almost consistent, which means the effect of solute diffusion in the liquid phase and force equilibrium at the triple junction play immaterial roles. Thus, it becomes clear that misfit accommodation

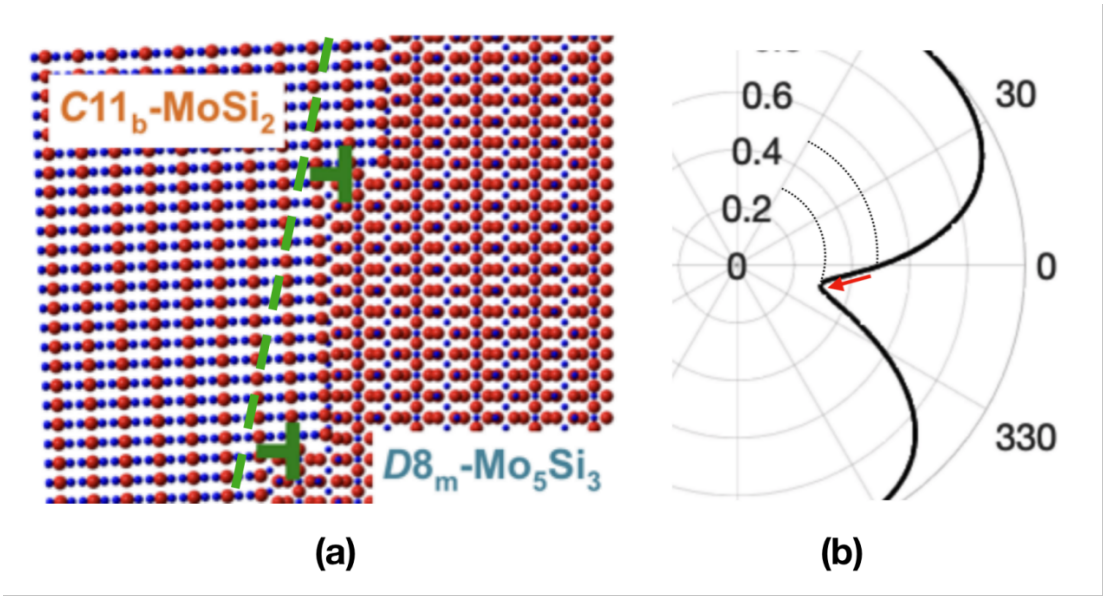

Figure 4.12: (a) Schematic illustration of the atomic arrangement of ledge-terrace structure; (b) the energy slump due to the inclination of macroscopic interface and formation of ledge-terrace structure.

plays a dominant role in determining morphology. Furthermore, the phase-field simulation result shows that the inclination angle can be nearly locked at the predetermined value only when the cusp is very sharp and deep. This means that energy relaxation accompanying with the lattice accommodation is strong, even to the extent of an energy slump (i.e., fast decrease). As illustrated in Fig.4.12, by the formation of inclined morphology rather than a vertical one parallel to the temperature gradient, the rotation of 13.5° makes the state of interface energy decrease from the level of 0.5 to a lower level 0.3. The formation of this slump has a close relationship with the coherency state of the interface and involves the generation of the elastic strain energy in the interface region. Since the current model uses a macroscopic interface description, future work could be the modeling on a microscopic scale with a rigorous consideration of elastic energy in the phase-field model.

4.5 Conclusions

In this chapter, we have discussed the formation mechanism of the script lamellar structure found in the directionally-solidified $MoSi_2/Mo_5Si_3$ eutectic structure. The conclusions can be summarized as follows: (I) The phase-field model is able to reproduce the essential physics during eutectic solidification, including interface undercooling, overgrowth, splitting, and dimension-restricted (diffusion-induced) inclination. (II) The 3D eutectic simulation reproduces the process of spacing selection and shows a length scale of microstructure close to that of experiment results. This demonstrates the validity of the present phase field model and the set of physical parameters. (III) Instability of the solid-liquid interface is responsible for the discontinuity of the script lamellar pattern. A mechanism of successive nucleation ahead of the solid-liquid interface has been proposed. The alloying element is claimed to be able to affect the nucleation condition, accordingly, the discontinuity of the irregular eutectic pattern. (IV) The interface inclination is caused by crystallographic interaction between the solid phases and has almost nothing to do with other factors such as solute diffusion in the liquid phase or the surface tension of the solid-liquid interface. The formation of ledge-terrace structure leads to a substantial relaxation of the misfit strain energy, which can be characterized as a slump of energy generated in the region of $MoSi_2/Mo_5Si_3$ interphase boundary.

References

[1] K. Jackson and J. Hunt, "Lamellar and rod eutectic growth," *Transactions of The Metallurgical Society of AIME*, vol. 236, pp. 1129–1136, 1966. 4, 4.1, 4.2.1, 4.3.2, 4.3.2

[2] J. Petrovic and A. Vasudevan, "Key developments in high temperature structural silicides," *Materials Science and Engineering: A*, vol. 261, pp. 1–5, 1999. 4.1

[3] H. Inui, K. Ishikawa, and M. Yamaguchi, "Effects of alloying elements on plastic deformation of single crystals of $mosi_2$," *Intermetallics*, vol. 8, pp. 1131–1145, 2000. 4.1

[4] H. Inui, K. Ishikawa, and M. Yamaguchi, "Creep deformation of single crystals of binary and some ternary $mosi_2$ with the c11b structure," *Intermetallics*, vol. 8, pp. 1159–1168, 2000. 4.1

[5] R. Mitra, "Mechanical behaviour and oxidation resistance of structural silicides," *International Materials Reviews*, vol. 51, pp. 13–64, 2006. 4.1

[6] D. Mason and D. Van Aken, "On the creep of directionally solidified $mosi_2/mo_5si_3$ eutectics," *Acta Metallurgica et Materialia*, vol. 43, pp. 1201–1210, 1995. 4.1

[7] H. Matsunoshita, Y. Sasai, K. Kishida, and H. Inui, "Plastic deformation of directionally solidified ingots of binary and some ternary $mosi_2/mo_5si_3$ eutectic composites," *Science and Technology of Advanced Materials*, vol. 17, pp. 517–529, 2016. 4.1, 4.4, 4.4.2, 4.10

[8] K. Fujiwara, H. Matsunoshita, Y. Sasai, K. Kishida, and H. Inui, "Effects of ternary additions on the microstructure and thermal stability of directionally-solidified $mosi_2/mo_5si_3$ eutectic composites," *Intermetallics*, vol. 52, pp. 72–85, 2014. 1.4, 1.2.2, 4.1, 4.4.1, 4.8, 4.4.2

[9] D. Fisher and W. Kurz, "A theory of branching limited growth of irregular eutectics," *Acta Metallurgica*, vol. 28, pp. 777–794, 1980. 4.1

[10] L. Rátkai, G. Tóth, L. Környei, T. Pusztai, and L. Gránásy, "Phase-field modeling of eutectic structures on the nanoscale: the effect of anisotropy," *Journal of Materials Science*, vol. 52, pp. 5544–5558, 2017. 4.1

[11] W. Kurz and D. Fisher, *Fundamentals of solidification*. Trans Tech Publications, 1986. 1, 1.2.2, 2.2.1, 4.1, 5.1

[12] S. Ghosh, A. Choundhury, M. Plapp, S. Bottin-Rousseau, G. Faivre, and S. Akamatsu, "Interphase anisotropy effects on lamellar eutectics: A numerical study," *Physical Review E*, vol. 91, p. 022407, 2015. 4.1

[13] S. Kim, W. Kim, T. Suzuki, and M. Ode, "Phase-field modeling of eutectic solidification," *Journal of crystal growth*, vol. 261, pp. 135–158, 2004. 4.1, 4.2.2

[14] J. A. Dantzig and M. Rappaz, *Solidification*. EPFL Press, 2009. 1, 2, 2.2.1, 2.2.4, 3, 4.2.1, 5.1

[15] M. Kellner, I. Sprenger, P. Steinmetz, J. Hötzer, B. Nestler, and M. Heilmaier, "Phase-field simulation of the microstructure evolution in the eutectic nial-34cr system," *Computational Materials Science*, vol. 128, pp. 379–387, 2017. 4.2.2

[16] M. Kellner, W. Kunz, P. Steinmetz, J. Hötzer, and B. Nestler, "Phase-field study of dynamic velocity variations during directional solidification of eutectic nial-34cr," *Computational Materials Science*, vol. 145, pp. 291–305, 2018. 4.2.2

[17] MICRESS©, "The microstructure evolution simulation software," 2007. 1.1, 1.2.3, 4.2.2

[18] I. Steinbach, "Phase-field models in materials science," *Modelling and simulation in materials science and engineering*, vol. 17, no. 7, p. 073001, 2009. 1.1, 2, 2.2.1, 2.2.2, 2.2.5, 3.1, 3.2.1, 3.2.3, 4.2.2, 5.2.1, 5.5

[19] T. Geng, C. Li, X. Zhao, H. Xu, Z. Du, and C. Guo, "Thermodynamic assessment of the nb–si–mo system," *Calphad*, vol. 34, no. 3, pp. 363–376, 2010. 4.3.1

[20] B. C. Allen, "The interfacial free energies of solid chromium, molybdenum and tungsten," *Journal of the Less Common Metals*, vol. 29, no. 2, pp. 263–282, 1972. 4.3.1

[21] P. Saidi, *Simulation Based Study of Solidification in Aluminum-Silicon System*. PhD thesis, Université Laval, 2015. 4.3.1

[22] B. Nestler and A. A. Wheeler, "A multi-phase-field model of eutectic and peritectic alloys: numerical simulation of growth structures," *Physica D:*

Nonlinear Phenomena, vol. 138, no. 1-2, pp. 114–133, 2000. 2.2.5, 4.3.2, 4.4.1

[23] A. Choudhury, M. Plapp, and B. Nestler, "Theoretical and numerical study of lamellar eutectic three-phase growth in ternary alloys," *Physical Review E*, vol. 83, no. 5, p. 051608, 2011. 4.3.3

[24] R. Trivedi, J. T. Mason, J. D. Verhoeven, and W. Kurz, "Eutectic spacing selection in lead-based alloy systems," *Metallurgical Transactions A*, vol. 22, no. 11, pp. 2523–2533, 1991. 4.3.3

[25] G. Kurtuldu, P. Jarry, and M. Rappaz, "Influence of cr on the nucleation of primary al and formation of twinned dendrites in al–zn–cr alloys: Can icosahedral solid clusters play a role?," *Acta Materialia*, vol. 61, pp. 7098–7108, 2013. 4.4.1

[26] G. Kurtuldu, A. Sicco, and M. Rappaz, "Icosahedral quasicrystal-enhanced nucleation of the fcc phase in liquid gold alloys," *Acta Materialia*, vol. 70, pp. 240–248, 2014. 4.4.1

[27] J. W. Gibbs, "On the equilibrium of heterogeneous substances," *American Journal of Science and Arts*, vol. 17, pp. 300–320, 1879. 4.4.2

[28] R. Qin and H. K. D. H. Bhadeshia, "Phase-field model study of the effect of interface anisotropy on the crystal morphological evolution of cubic metals," *Acta Materialia*, vol. 57, pp. 2210–2216, 2009. 3.2.2, 4.4.2

Chapter 5

Rapid Solidification of Alloy

The solute redistribution in alloy solidification is responsible for the formation of various patterns, such as dendrite and eutectic (Sec. 1.1). The simulation results in two dimensions in Fig.2.11 show the dependency on the diffuse interface width, which needs to be overcome through a numerical scheme in order to achieve the true solution of the interface morphology, namely quantitative simulation [1, 2, 3, 4]. Another issue of simulating solidification in some advanced processing, such as additive manufacturing, is that the equilibrium assumption within the interface may lose its validity. Non-equilibrium solute partitioning may arise as the interface moves at a high velocity [5, 6, 7]. Nowadays, the definition of the quantitative phase-field modeling of alloy solidification has been extended to a wide range of cooling conditions, involved with both equilibrium and non-equilibrium solute partitioning. In order words, the requirements of quantitative solidification simulation have two aspects: one is that the interface kinetics should not be affected by the artificially wide interface; two is that the partition coefficient in the diffuse interface should vary with the interface velocity.

In this chapter, a new diffuse interface model has been proposed for quantitatively simulating binary alloy solidification. Starting from the Gibbs-Thomson equation, which is the classical theory that describes the dynamics of a sharp

interface, the phase-field equation is derived using a traveling wave solution that represents a diffuse interface. To tackle the spurious effects caused by the variation of liquid concentration within the diffuse interface with artificial width, a middle obstacle is introduced to "sharpen" the diffuse interface and an invariant liquid concentration can be found for determining a constant undercooling in the interface normal direction. For slow solidification under equilibrium conditions, the convergence performance of the dendrite tip shows superior invulnerability to the width effect of the diffuse interface. For rapid solidification under non-equilibrium conditions, the output partition coefficients obtained from the steady-state concentration profiles agree with the input velocity-dependent function. The proposed model is promising to be an indispensable tool for the development of advanced alloy materials through the microstructure control of solidification under a wide range of cooling conditions.

5.1 Non-equilibrium Solute Partitioning

In alloy solidification, solute partitioning can be either equilibrium or non-equilibrium, depending on the interface velocity [8, 9] (Fig.5.1). Local equilibrium is usually assumed within the interface moving at a slow or moderate speed and the solute with limited solubility is partially rejected from the newly formed solid. The concentrations on the two sides of the steady-state interface lie on the solidus and liquidus of the equilibrium phase diagram. When the interface velocity becomes high, the amount of captured solute exceeds the solubility and the liquid concentration ahead of the interface becomes far away from the liquidus. Consequently, the morphology and concentration distribution in the microstructures resulting from slow and fast solidification processes are distinct. Thus, it is vital to fully describe the process of non-equilibrium solute partitioning, which is

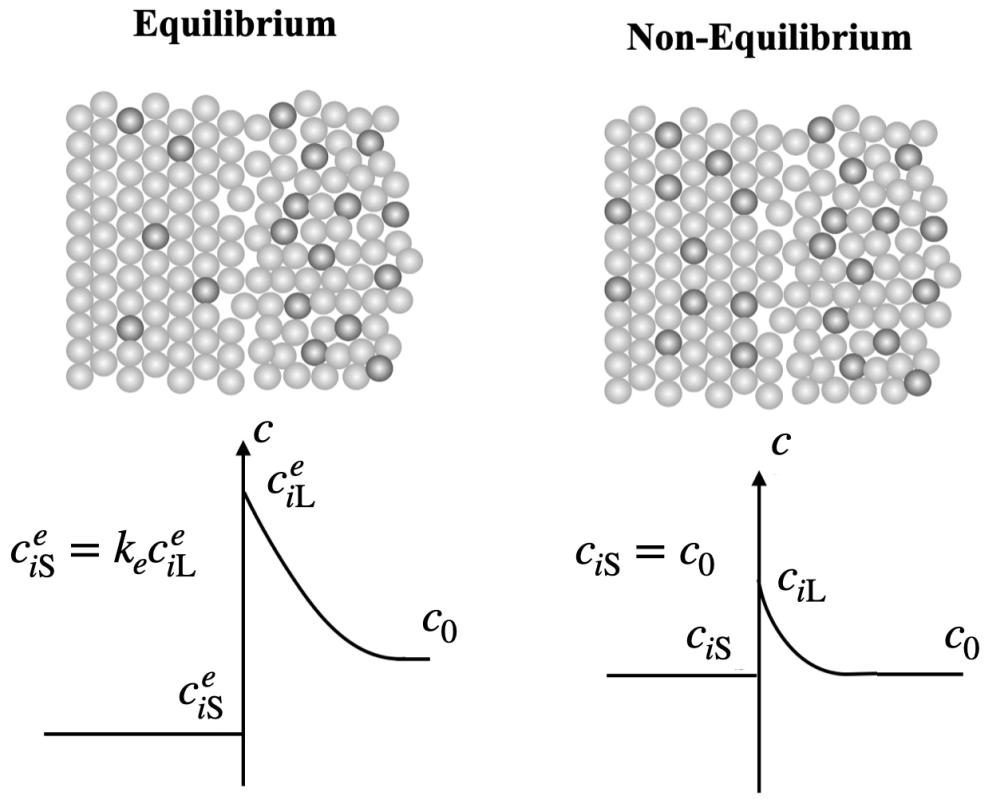

Figure 5.1: Schematic of the solute profiles across the interface. (a) equilibrium solute partitioning for low interface velocity; non-equilibrium solute partitioning for high interface velocity.

dependent on interface velocity, for optimizing the processing conditions during rapid solidification and developing advanced alloy materials.

The continuous growth (CG) model [6, 10] and the local non-equilibrium (LN) model [11, 12] are two established models for describing the non-equilibrium solute partition. The interface is assumed to be a sharp plane in these analytical models. Correspondingly, numerical models including diffuse interfaces were developed in accordance with the analytical ones. They are the so-called parabolic [7, 13, 14] and hyperbolic [15] phase-field models, respectively. Despite the phys-

ical correctness of these phase-field models, they can hardly be implemented in two-dimensional space to be relevant to the characteristic length of the microstructure because the width of the diffuse interface in these models needs to have a physical size on the nano-scale. If the interface width is artificially enlarged to reduce the computational cost, the numerical models are invalid in matching the analytical ones. It is required to develop numerical schemes that can improve the computational efficiency of the diffuse interface models without losing the connection to the analytical sharp interface models.

The so-called quantitative phase-field model [2, 3, 16, 17] is the parabolic model with an artificially wide interface. They can be mapped unto the analytical sharp interface model through thin-interface analysis and additional flux incorporated into the diffusion equation. The simulation results of alloy solidification can possibly be independent of the interface width once a thin interface limit is reached. It should be noted that the convergence of the results from these models is mostly limited to low-speed interfaces under equilibrium conditions. It is still challenging to extend them to simulate high-speed interfaces under non-equilibrium conditions.

Despite the success of quantitative modeling of equilibrium solidification, the phase-field models for rapid solidification are still under active development [18, 19, 20, 21, 22, 23, 24]. The essence of all these models lies in the regulation of solute redistribution within the diffuse interface by referring to the CG or LN analytical models. In the work of Tatu et al.[18] and Kavousi et al.[19], the anti-trapping current is modified for regulating non-equilibrium solute partitioning. Results weakly dependent on the interface width can be obtained. Ji et al.[22] reproduced the banded structure consistent with experimental observation. In their model, the solute transport in the diffuse interface region is enhanced by introducing a diffusivity interpolated by a quadratic function, which should be

adapted according to the interface width. The model proposed by Steinbach et al.[25] incorporates a third kinetic equation for controlling the exchange of solute atoms between solid and liquid phases within the interface. The results tend to be dependent on the interface width and the kinetic parameter (permeability) needs to be determined by fitting to the experimental or analytical data [26].

The present work chooses a new approach to mapping the diffuse interface model to its sharp interface counterpart. Rather than mapping the parabolic or hyperbolic phase-field models unto their analytical counterparts, the velocity-dependent partition coefficients obtained from CG and LN models can be straightforwardly incorporated into the proposed diffuse interface model. The simulations of dendrite growth under equilibrium conditions and excessive solute trapping under non-equilibrium conditions will be demonstrated to verify the applicability of the proposed model.

5.2 Proposed Model for Rapid Solidification

5.2.1 Standard model of alloy solidification

The governing equations, including the phase-field equation and diffusion equation, of the standard model are revisited prior to the proposal of the numerical scheme to eliminate the side effect of the artificially wide interface. The kinetics of the sharp interface is described by the Gibbs-Thomson equation,

$$v = \mu(\Delta T - \Gamma\kappa) \tag{5.1}$$

The motion of the interface is driven by the contributions from interface undercooling ΔT and the surface pressure related to curvature κ and Gibbs-Thomson coefficient Γ, which is the ratio of surface energy to fusion entropy. The pro-

portional relationship between the net contribution and interface velocity v is suggested by the kinetic coefficient μ.

In the diffuse interface model, a continuous field parameter is used to represent the bulk phases as well as the interface. The so-called phase field keeps constant in the bulk regions and varies smoothly within the interface region. Conventionally, the value of the phase field changes from 1 in the solid to 0 in the liquid, showing a diffuse profile at the interface. For pure substances, the equation that governs the kinetics of the diffuse interface can be expressed by referring to the Gibbs-Thomson equation. The resulting phase-field equation [27, 28] is

$$\frac{1}{|\nabla\phi|}\frac{\partial\phi}{\partial t} = \mu\left[\Delta T - \Gamma\nabla\left(-\frac{\nabla\phi}{|\nabla\phi|}\right)\right] \tag{5.2}$$

in which interface velocity v and curvature κ are replaced by the gradient and local change of the phase field ϕ. For isothermal conditions when ΔT is constant throughout the domain, Eqs.(5.1) and (5.2) are identical if a proper solution for the phase field with a diffuse interface profile can be found. Compared to the Gibbs-Thomson equation, the phase-field equation facilitates the numerical simulation of pattern formation because the position, curvature, and morphology of the interface can be implicitly and easily obtained from the spatially continuous phase field.

The solution of the phase field can be found by minimizing the total free energy of the whole domain with bulk phases and diffuse interface. Following the derivation in [29], the solution of the steady-state diffuse interface in 1D is specified as,

$$\phi = \begin{cases} 1 & x < -\eta/2 \\ \frac{1}{2} - \frac{1}{2}\sin\frac{\pi}{\eta}(x - vt) & -\eta/2 \leq x \leq \eta/2 \\ 0 & x > \eta/2 \end{cases} \tag{5.3}$$

which is the so-called traveling wave solution. The interface width is η and the velocity is v. The values of the phase field in the solid and liquid regions are 1 and 0, respectively. For position within the interface ($-\eta/2 + vt \leq \mathrm{x} \leq \eta/2 + vt$), the solution shows a diffuse contour constructed by the sinusoidal function, which has singularities at the boundaries between the interface and bulk regions. Despite this, the traveling wave solution has its advantage in numerical implementation and is related to the double obstacle function used in the free energy functional. With this solution, Eq.(5.2) can be reformulated to be,

$$\frac{\partial\phi}{\partial t} = \mu\left\{\Gamma\left[\nabla^2\phi + \frac{\pi^2}{\eta^2}(\phi - \frac{1}{2})\right] - \frac{\pi\sqrt{\phi(1-\phi)}}{\eta}\Delta T\right\} \tag{5.4}$$

For a moving interface of a dilute binary alloy with a negative liquidus slope, the solute atoms are rejected from the growing solid into the liquid. The concentration on the solid side is lower than that of the liquid side. Thus, the concentration profile shows a jump at the interface and a diffusion layer in the bulk liquid. This jump can be expressed as

$$c_{i\mathrm{S}} < c_{i\mathrm{L}} \tag{5.5}$$

in which the subscript "i" denotes the position at the interface. In the diffuse interface model, this jump is manifested by a continuous transition across the interface (Fig.5.2). By assuming the interface is a mixture of the solid and liquid phases, the concentrations of solid and liquid are individual field variables and the

overall concentration is weighted by the local phase fractions, which is indicated by the local phase field. The relation of the three distinct concentration fields is expressed by,

$$c = c_{\mathrm{S}}\phi + c_{\mathrm{L}}(1-\phi) \tag{5.6}$$

Similarly, the change of the local overall concentration is the sum of changes in individual solid and liquid phases. The fluxes according to Fick' s law in solid and liquid phases are also weighted by the local phase factions,

$$J_{\mathrm{S}} = -\phi D_{\mathrm{S}} \nabla c_{\mathrm{S}} \tag{5.7}$$

$$J_{\mathrm{L}} = -(1-\phi) D_{\mathrm{L}} \nabla c_{\mathrm{L}} \tag{5.8}$$

in which D_S and D_L are diffusivities in solid and liquid phases. The diffusion equation [27, 28] can then be written by complying with the law of mass conservation,

$$\frac{\partial c}{\partial t} = -\nabla\big(J_{\mathrm{S}} + J_{\mathrm{L}}\big) \tag{5.9}$$

which can be expanded by the chain rule of derivative,

$$\frac{\partial c}{\partial t} = D_{\mathrm{S}}(\nabla\phi\nabla c_{\mathrm{S}} + \phi\nabla^2 c_{\mathrm{S}}) + D_{\mathrm{L}}\big[-\nabla\phi\nabla c_{\mathrm{L}} + (1-\phi)\nabla^2 c_{\mathrm{L}})\big] \tag{5.10}$$

Special attention needs to be paid to the boundary conditions of the liquid and solid concentrations at their limits within the interface. During the numerical implementation of the diffusion equation, the fluxes in the liquid and solid should

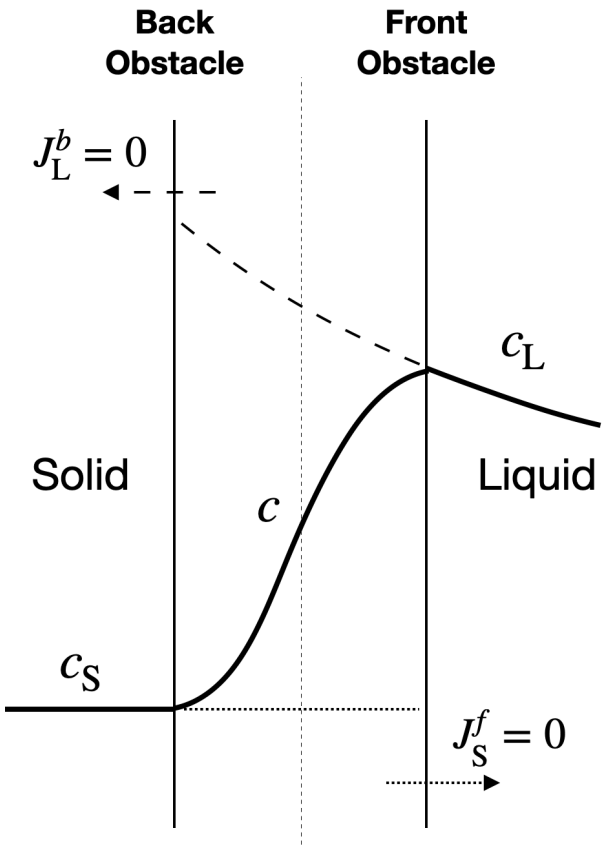

Figure 5.2: Schematic image of the liquid, solid, and overall concentration fields of a moving interface in the diffuse interface model. The change of overall concentration comes from the sum of changes in the solid and liquid phases, which are implemented separately in computation through the diffusion equation. The fluxes at the limits (back and front obstacles) of liquid and solid phases are set to zero.

be blocked where the phase fractions become zero:

$$J_{\mathrm{L}}^{b} = J_{\mathrm{S}}^{f} = 0 \tag{5.11}$$

Here, we designate these places as obstacles for solute transport. The limit of the liquid phase is called the back obstacle, while the one of the solid phase is called the front obstacle. The physical meaning of these obstacles is that the solute in the liquid phase can not be transported to the solid phase by diffusion, and vice versa.

5.2.2 Middle obstacle approach

In the sharp interface model, the propagation of the interface is accompanied by the inter-diffusion of solute between solid and liquid within the interface as well as the long-range transport of solute away from the interface toward two sides. The former results in solute partitioning and rejection, while the latter lowers the concentration at the interface. The steady state is realized when the two processes are balanced. Correspondingly, the same processes happen in the diffuse interface model. In the following paragraphs, the details of mapping the diffuse interface model unto its sharp interface counterpart will be explained.

Fig.5.3 demonstrates the coupled phase and concentration fields in two consecutive steps. The local change of phase field is denoted by $\delta\phi$, which is the amount of liquid that transforms into solid. This change is accompanied by the change of local concentration δc. If a steady state is realized, the two concentration profiles should be identical except for the shifted position. To determine the amount of δc, the diffuse interface is divided into several representative volumes (RVs) to show the specific processes in each individual numerical grid. In Fig.5.4, the RV is a rectangle with two separate areas representing the mixture of solid and liquid

phases with the denoted fractions and concentrations. As the local phase field changes, fractions and concentrations in the current RV on the left-hand side are reconfigured in the next RV on the right-hand side. The fraction of the newly formed solid is $\delta\phi$. Theoretically, for the dilute alloy with a negative liquidus slope, the newly formed solid can not capture all the solute of its previous liquid, which has a concentration of c_L. The amount of trapped solute is related to the inter-diffusion (partitioning) process in the sharp interface model. If the interface velocity is very large, the time for phase transformation is so limited that the capture coefficient λ may approximate unity and no solute is rejected from the solid. For most cases when interface velocity is low and moderate, the time is sufficient for the exchange of solute between the local solid and liquid. The capture coefficient λ is smaller than 1 and the amount of rejected solute can be determined to be,

$$\delta \mathrm{c} = (1 - \lambda)\mathrm{c_L}\delta\phi \tag{5.12}$$

which is the local descending amplitude of the concentration profile in Fig.5.3.

The capture coefficient is unknown yet. Intuitively, it has a relation to the partition coefficient as both of them approach unity at high interface velocity. However, they are different in their physical meanings. The latter is the result of the equality of chemical potential and is related to the inter-diffusion between the solid and liquid phases. The capture process represents the solute flow from the liquid to the solid. A relation between these two coefficients can be found by considering the mass conservation and equality of chemical potential. In the present work, for the sake of simplicity at the beginning of model development, it has been assumed that the capture coefficient equals to the partition coefficient and that all rejected solute atoms are released to the local liquid. This assumption

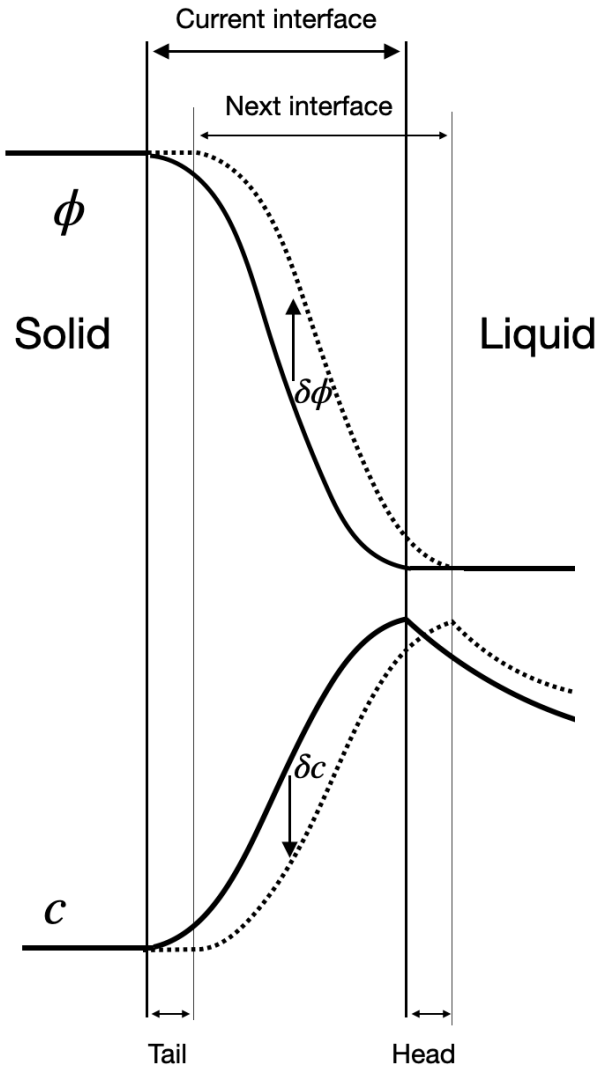

Figure 5.3: Schematic image of the coupled phase and concentration fields in two sequential steps. As the interface moves forward, the concentration profile shifts in the same direction as a result of solute partitioning and long-range transport.

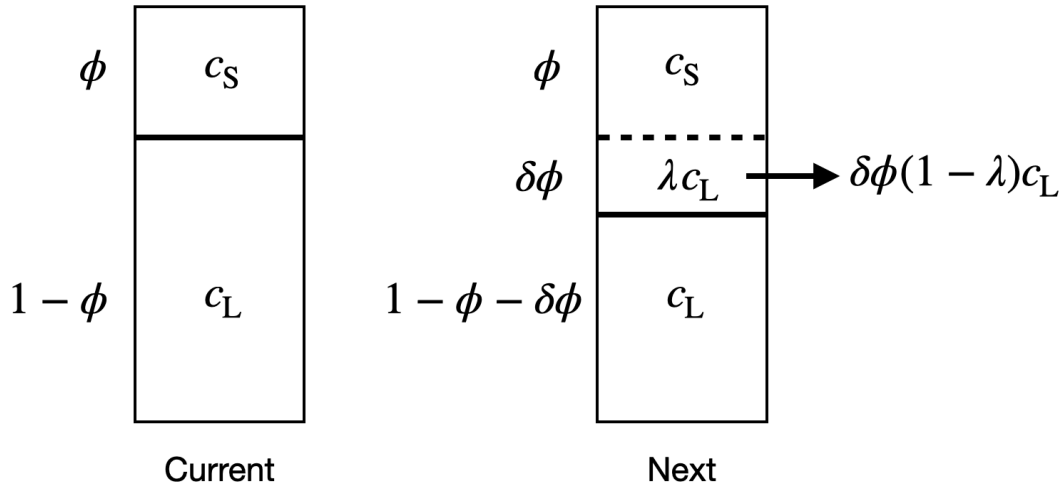

Figure 5.4: The changes of phase and concentration fields in a representative volume (RV) of the diffuse interface. For simplicity, the capture coefficient is assumed to be the partition coefficient, which can be the function obtained from either CG or LN model.

brings about two consequences: one is that the present model is a one-sided model, in which the diffusion in the solid has been neglected; another one is that the capture coefficient can be a function of the interface velocity, which can be obtained from the analytical CG or LN models. Thus, the function of the CG model can be straightforwardly input into the phase field model through the capture coefficient. It can be expressed as

$$\lambda = k(v) = \frac{k_e + v/v_{\mathrm{D}}}{1 + v/v_{\mathrm{D}}} \tag{5.13}$$

In future work, the exact relation between the capture and partition coefficients needs to be derived to incorporate the effect of solute diffusion in the solid phase. Also, the partition coefficient function of the LN model will be used to more fully describe the non-equilibrium solute trapping using the proposed phase-field model.

One may ask how to deal with rejected solute δc associated with the change $\delta\phi$ in each RV. In the sharp interface model, the rejected solute should be transported by long-range diffusion into both liquid and solid phases. In the diffuse interface model, it should be released to the local solid and liquid phases. However, problems should arise when the interface width is artificially enlarged. It takes a long distance to transport the solute out of the interface region. The rejected solute in the tail area (Fig.5.3) can not be released into the liquid because there is no liquid in that area after the phase transformation. As a result, they should be trapped in the solid. The solute trapping in the diffuse interface model inherently exists in all alloy phase-field models. If the interface width has a physical size on the nano-scale, the parabolic model resembles the sharp interface CG model in modeling solute trapping [7, 13]. However, in the model with an enlarged diffuse interface, the trapping becomes excessive and undesired. An operation on the rejected solute is needed to enhance the solute transport and eliminate this spurious effect caused by the artificially wide diffuse interface.

In the present work, the anti-trapping operation has been accomplished by collecting the rejected solute atoms in each RV and then casting them in the normal direction of the interface. This can be realized by iteratively searching the next grid in the normal direction of the interface during the numerical implementation (See appendix). This anti-trapping operation on the rejected solute δc facilitates the solute redistribution within the artificially wide diffuse interface. It is crucial and should be implemented with care to avoid spurious effects that may easily arise. For example, if all the rejected solute atoms are collected and cast into the bulk liquid just in front of the interface, the solute transport is excessively enhanced by this operation in the normal direction of the interface. This enhancement is proportion to the interface width and affects the simulation results. Therefore, a natural and sophisticated way is required to emulate the

solute redistribution process in the sharp interface model.

A middle plane of the interface is used to "sharpen" the diffuse interface model. As illustrated in Fig.5.5, the diffuse interface is divided into the front and back parts by the middle plane, which is called the middle obstacle (MO) here. As the dashed arrows in Fig.5.5 suggest, the rejected solute atoms in the back part should be collected and cast just in front of the middle obstacle, whereas the ones in the front part should be transferred to the local liquid and transported away by diffusion. As a result, the diffuse interface, which has been assumed to be a mixture of solid and liquid, can then be regarded as the extensions from the bulk solid and liquid phases separated by the imaginary "sharp" interface. The tangential diffusion in the diffuse interface turns out to be the diffusion process in the bulk phases.

As the rejected solute atoms δc in the two parts separated by the middle obstacle are transported in distinct manners, the profiles of the liquid concentration on the two sides should be quite different. In the front part of the diffuse interface, the profile joins with the middle obstacle and extends its gradient to the diffusion layer in the bulk liquid; in the back part of the diffuse interface, because the liquid concentration is not affected by the collect-and-cast operation, the concentration inside the back part should be quickly flattened by the diffusion process. The liquid concentration just behind the middle obstacle can be regarded as the liquid concentration at the sharp interface. Because it might be independent of the interface width, it is called invariant concentration c_L^{inv}, which can be used to determine the interface undercooling.

$$\Delta T = T_{\mathrm{m}} - T_i + c_{\mathrm{L}}^{inv} m_{\mathrm{L}} \tag{5.14}$$

in which T_m, T_i, and m_L are the melting point, interface temperature, and liquidus

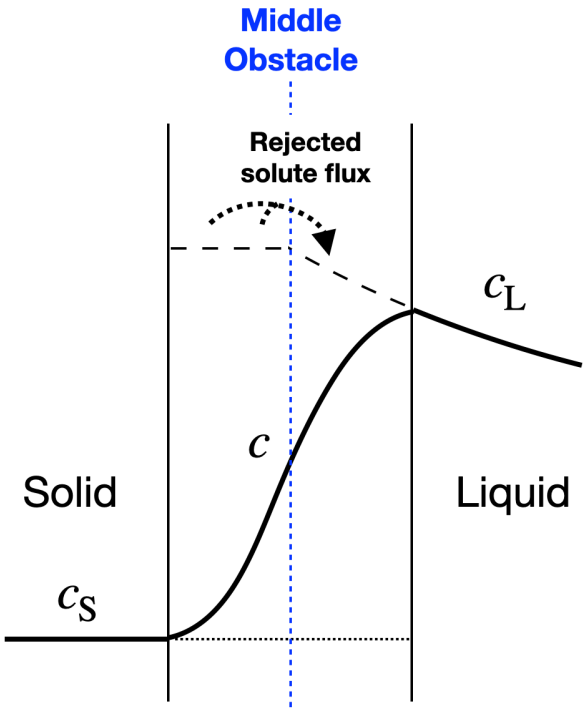

Figure 5.5: Schematic concentration profiles as a result of the anti-trapping operation and the middle obstacle. The rejected solute atoms in the back part are collected and cast (see appendix) just ahead of the middle obstacle and the ones in the front part are transferred locally to the liquid and transported out of the interface by diffusion. An invariant concentration can be found just behind the middle obstacle.

slope. The concentration of each gird within the interface should be determined by searching the nearest invariant concentration in the normal direction through the numerical technique applied in the collect-and-cast operation (See appendix).

5.3 Solidification Simulation of Al-Cu Alloy

The binary alloy system is chosen to be Al-1.3at.%(3wt.%)Cu. The physical parameters [17, 30] are as follows: melting point of pure aluminum, 931 K; diffusivity of copper in the liquid, 2.4×10^{-9} m^2/s; liquidus slope, -600 K/at.; partition coefficient, 0.14; Gibbs-Thomson coefficient, 2.4×10^{-7} Km. Other physical and numerical parameters will be mentioned in the following simulation results.

5.3.1 Low growth rate

The isothermal temperature is set to be 917 K for low-rate solidification under equilibrium conditions. In 1D simulation (Fig.5.6), the diffuse interface is resolved by 8 grids. The total solute is conserved in the whole domain, suggesting the anti-trapping (collect-and-cast) operation does not change the nominal concentration. As expected, the liquid concentration profile shows a discontinuity at the position of the middle obstacle. In the 2D simulation (Fig.5.7 inset), the dendrite grows in a moving frame until its tip velocity reaches a steady state. The computational domain has a physical size of 32 μm$\times$64 μm. The resolution of the domain depends on the interface width, which should be adjusted by comparing it with the tip velocity and the resulting diffusion length. Three interface widths (3.0, 1.5, and 0.75 μm) are used and each of them is resolved by 6 girds. To maintain numerical stability, the kinetic coefficient is chosen to be 0.5×10^{-3} m/(s·K), which is 200 times smaller than the physical value of 0.1 m/(s·K) for the atomically rough surface [31].

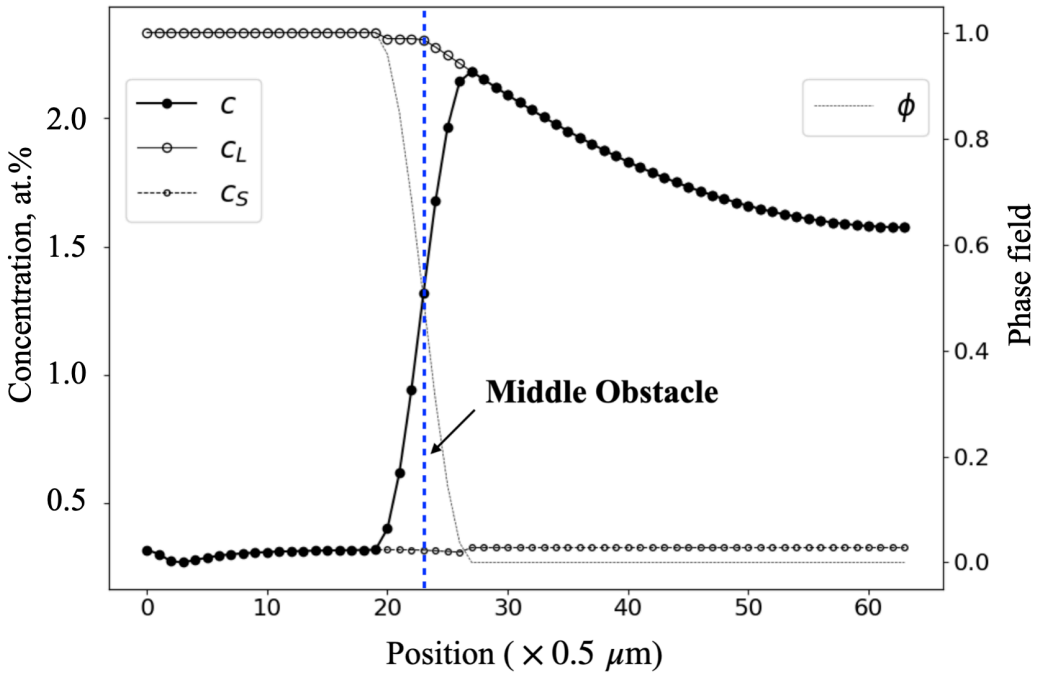

Figure 5.6: 1D simulation result with concentration and phase field profiles. The concentration in the liquid phase shows a discontinuity at the middle obstacle, where ϕ=0.5. The liquid phase has the equilibrium concentration in the solid. The same is for the solid phase.

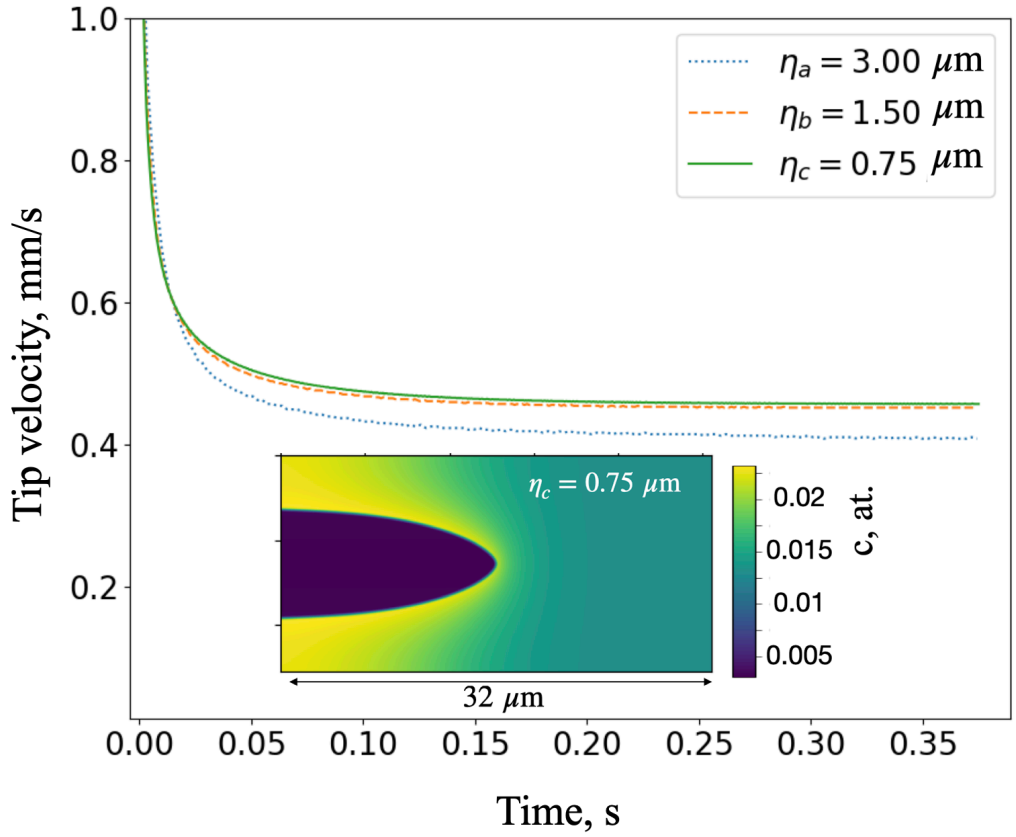

Figure 5.7: Change of dendrite tip velocity with time under isothermal condition (917K). The inset figure is the concentration map that shows the steady-state dendrite arm in a moving frame at 0.35s.

As plotted in Fig.5.7, three cases of dendrite simulation reach steady states after the physical time of 0.35 s. As the interface width decreases, the tip velocity converges at a value of around 500 μm/s. The diffusion length l_D [30] ahead of the tip is the ratio of diffusivity to the tip velocity and has a value of about 4.8 μm. In principle, l_D should be larger than the interface width η in phase-field simulation. The ratio of l_D to η is a common measure of numerical performance. The smaller the ratio, the higher the efficiency. In the present simulation, the convergence happens with the interface width η_b=1.5 μm because the difference between the tip velocities in simulations with η_b and η_c is less than 1.5%. The ratio l_D/η_b is about 3.2, which suggests a competitive performance compared to the established quantitative model in the literature [2, 16, 17]. Even with the interface width η_a, the difference in tip velocity from the converged ones is around 10%. This suggests that the tip velocity is highly invulnerable to the width effect of the diffuse interface owing to the middle obstacle approach. The model is efficient in simulating solidification under equilibrium conditions. The correctness of the dendrite morphology will be verified by comparison with quantitative models and theoretical analysis [32] in future work.

5.3.2 High growth rate

As the isothermal temperature becomes low and the interface velocity increases, the solute partitioning process turns to be non-equilibrium and dependent on the interface velocity. As the interface velocity reaches as high as about 1 m/s, the diffusion length is shortened to about a few nanometers. Thus, the width of the interface in simulation should be also on the nano-scale. The kinetic coefficient is chosen to have a physical value of 0.1 m/(s·K) in the following simulation.

Fig.5.8 shows the concentration profiles of two high-speed moving interfaces. The diffusion length varies according to the interface velocity. The solid concen-

trations are equal to the far field liquid concentration, exhibiting the complete trapping phenomenon, which is the typical feature of the steady state during non-equilibrium solidification [25]. The liquid concentration profiles overlap with overall concentrations in the bulk liquid and show a step in the interface, where the invariant concentration lies. The large difference between the invariant and equilibrium concentration suggests the large deviation from the equilibrium and high undercooling at the interface. The undercooling is calculated by referring to the vertical distance to the liquidus in the equilibrium phase diagram. It should be noted that the velocity-dependent liquidus slope [32] and the effect of solute drag [10] have not been considered in the present work.

The partition coefficients obtained from concentration profiles under a range of temperatures are plotted against the interface velocities. The partition coefficient is defined to be the ratio of invariant concentration to the solid concentration near the interface. When the temperature is high, the complete trapping steady state may not happen, but the instant velocity and partition coefficient can still be measured. These point data from simulations are plotted in Fig.5.9 along with the function of the CG model, which has been input into the PF model according to Eq.5.13. A good agreement between them can be discerned. As shown in Fig.5.10, when the interface width in the PF model increases, the steady-state velocity and partition coefficient deviate from the results of the small interface width. For the interface width of 5 nm, the deviation ($<10\%$) is obvious but still acceptable and the points stay near the curve of the CG model.

As the PF model is capable of simulating velocity-dependent solute partitioning, it is expected to reproduce experimentally relevant phenomena. The banded structure [33] formed during rapid solidification features in the cyclic growth with equilibrium and non-equilibrium solute partitioning. A temperature gradient (10^7 K/m) is imposed on the domain and the constant cooling rate (6×10^6 K/s) gives

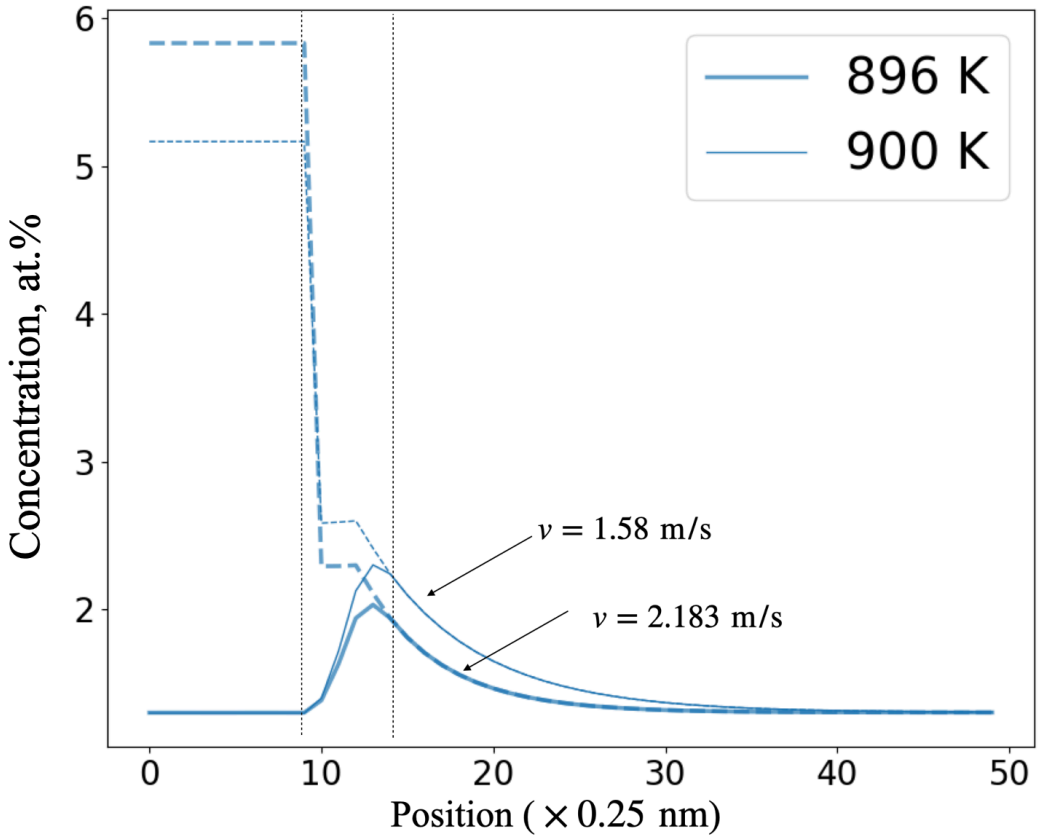

Figure 5.8: Steady states of rapid growth under isothermal conditions. The complete trapping phenomenon is the typical feature of the steady state of rapid solidification. Interface undercooling is calculated by referring to the liquidus in the equilibrium phase diagram (velocity-dependent liquidus slope and solute drag have not been considered yet).

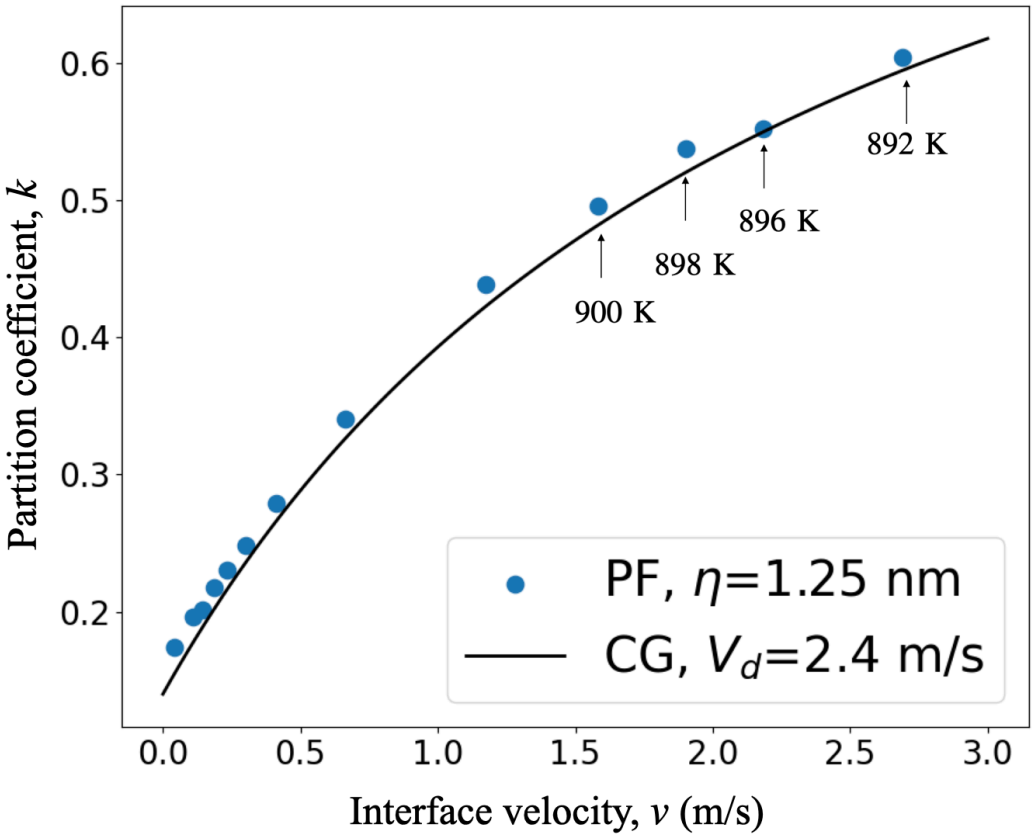

Figure 5.9: Partition coefficients from analytical model and simulation results. The diffuse interface width in the PF model is 1.25 nm.

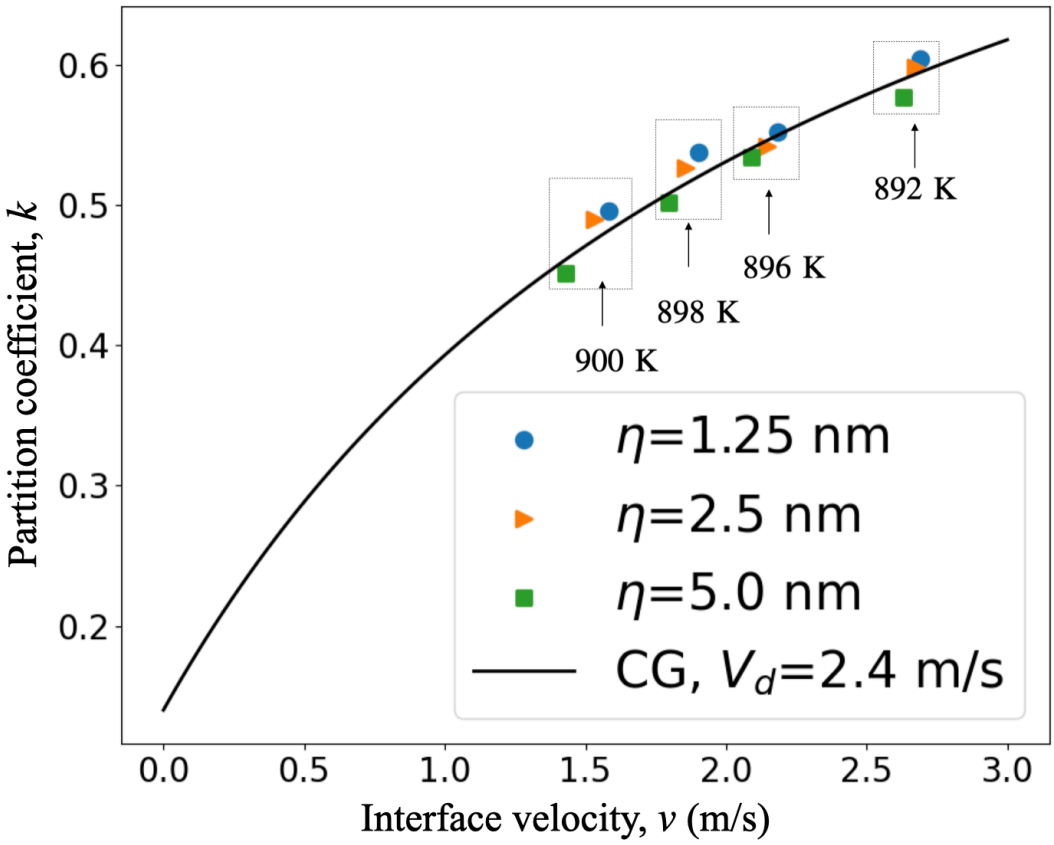

Figure 5.10: Partition coefficients obtained from PF simulation with different interface widths are compared. All interfaces are in complete trapping steady states. Interface velocity appears to deviate as the interface width increases.

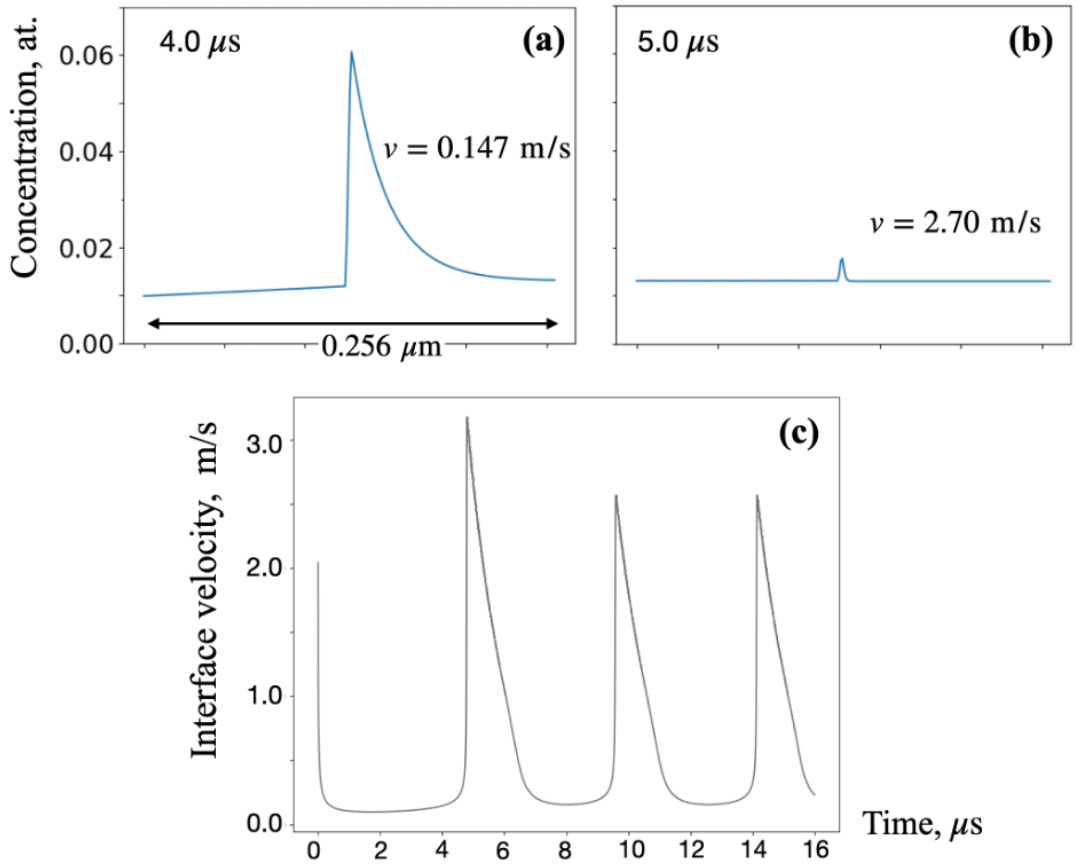

Figure 5.11: Oscillatory growth under directional cooling condition ($G_{\mathrm{T}} = 10^7$ K/m, R=6 $\times$ 10^6 K/s). The initial temperature at the interface is 905K. (a) diffusion-controlled slow interface under the equilibrium condition; (b) attachment-controlled fast interface under the non-equilibrium condition; (c) Interface velocity shows significant oscillation during the interface propagation under a moving temperature gradient.

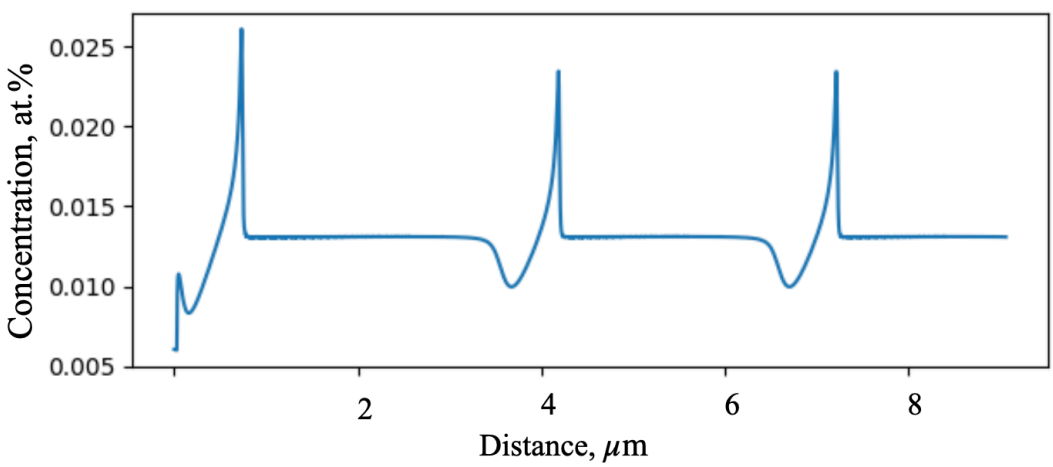

Figure 5.12: Concentration profile after the pulled growth in Fig.5.11

.

rise to the pulling velocity of 0.6 m/s. The initial temperature at the interface is 905 K. As shown in Fig.5.11(a, c), the interface grows at a low velocity in the beginning and the concentration jump at the interface suggests diffusion-controlled growth under the equilibrium condition. The interface velocity does not adapt to the pulling velocity immediately because of the accumulating solute ahead of the interface. It only increases gradually because of the decreasing interface temperature. Until a critical state is reached at 4.3 μs, the interface velocity surges to be over 3 m/s and the growth is no longer controlled by the solute diffusion but by the atomic attachment (Fig.5.11b). Because of the high propagation speed, the interface moves far ahead along the temperature gradient, the decreased undercooling relaxes the motion of the interface. The interface slows down and returns to be controlled by diffusion. As Fig.5.11c shows, the cycle of fast and slow growth modes continues with a steady amplitude of oscillation, which can be discerned from 10 to 16 μs. The resulting concentration distribution (Fig.5.12) after solidification is remarkably similar to the banded structure observed in Fig.1.5 and in literature [33].

5.4 Conclusions

A type of phase-field model that can effectively model alloy solidification under both equilibrium and non-equilibrium conditions is explained and demonstrated. Under equilibrium conditions, the convergence behavior of the dendrite tip is invulnerable to the width effect of the diffuse interface. An acceptable convergence happens when the ratio of diffusion length l_D to interface width η approaches 3.5. Under non-equilibrium conditions, the velocity-dependent partition coefficient from the CG model can be simply input into the PF model. The output one-dimension results agree with the input function. The simulation results are weakly affected even when the ratio is less than 1. The middle obstacle approach has been proven to be effective in "sharpening" the diffuse interface in phase-field modeling. Future work will relate the capture coefficient to the partition coefficient so that solute diffusion in the solid is included. The velocity-dependent liquidus slope and the effect of solute drag on the interface undercooling are also required to achieve a more accurate simulation. 2D and 3D simulations are to be conducted and compared with analytical theories and experimental observations.

5.5 Appendix: Explanation of the collect-and-cast operation and invariant concentration in 2D

The key feature of the traveling wave solution, which is related to the double obstacle free energy density, is that there are singularities at the boundary between the bulk region and interface region. This is quite different from the phase field model with a double well free energy density in its free energy functional. The

choice of traveling wave solution has many benefits [29]. In the current model, the reason for choosing this solution is that it enables zeros fluxes at the interface limits and facilitates the collect-cast operation, which is adopted to avoid undesired solute trapping in the diffuse interface.

The collect and cast operation might easily be understood in 1D, as shown in Fig.5.5. Here, it is illustrated in the 2D domain to clarify the detailed process. In Fig. 5.13, the distribution of phase field in the numerical grids is denoted by the grey scale of the dots. The polygonal lines that connect the dots are back, middle and front obstacles from the inner to the outer sides. After the evolution of the phase field, the forward motion of the interface comes from the increment of the phase field near and in the diffuse interface. The amount of rejected solute due to the local transformation of liquid to solid can then be determined according to Eq.5.12. As the solid-line arrows denote, the rejected solute is cast just ahead of the middle obstacle. Similarly, the dashed-line arrows denote the path of searching invariant concentration just behind the middle obstacle. The path of these arrows is calculated by the following steps:

Step 1: Calculate the interface normal vector at the initial grid (i, j), which is

$$\vec{n} = (n_x, n_y) \tag{5.15}$$

Step 2: Search the next grid by referring to the interface normal. Because both are smaller than 1, the next grid should be determined by rounding the above indexes to be 0 or 1. The gird indexes are

$$(i + [n_x], j + [n_y]) \tag{5.16}$$

Accordingly, the next next grid indexes are

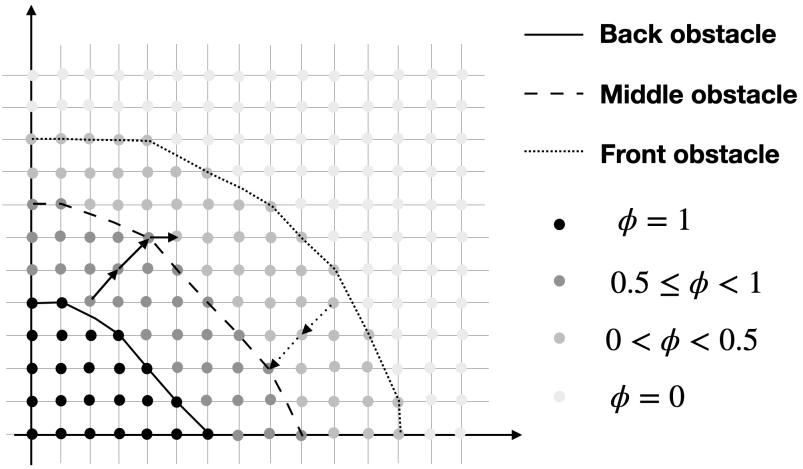

Figure 5.13: Schematic of the grid-by-grid distribution of phase field in two dimensions. The solid-line arrows show the path of casting the rejected solute. The dashed-line arrows show the path of searching invariant concentration.

$$(i + [2n_x], j + [2n_y]) \tag{5.17}$$

The grid search should repeat until the phase field is lower than 0.5.

Step 3: The rejected solute should be subtracted from the initial grid and added to the grid just ahead of the middle obstacle.

References

[1] A. Karma and W.-J. Rappel, "Quantitative phase-field modeling of dendritic growth in two and three dimensions," *Physical review E*, vol. 57, no. 4, p. 4323, 1998. 5

[2] A. Karma, "Phase-field formulation for quantitative modeling of alloy solidification," *Physical review letters*, vol. 87, no. 11, p. 115701, 2001. 5, 5.1, 5.3.1

[3] B. Echebarria, R. Folch, A. Karma, and M. Plapp, "Quantitative phase-field model of alloy solidification," *Physical review E*, vol. 70, no. 6, p. 061604, 2004. 5, 5.1

[4] M. Ohno, "Quantitative phase-field modeling and simulations of solidification microstructures," *ISIJ International*, vol. 60, no. 12, pp. 2745–2754, 2020. 5

[5] A. A. Wheeler, W. J. Boettinger, and G. B. McFadden, "Phase-field model of solute trapping during solidification," *Physical Review E*, vol. 47, no. 3, p. 1893, 1993. 2.2.3, 5

[6] M. J. Aziz, "Model for solute redistribution during rapid solidification," *Journal of Applied Physics*, vol. 53, no. 2, pp. 1158–1168, 1982. 5, 5.1

[7] N. Ahmad, A. Wheeler, W. J. Boettinger, and G. B. McFadden, "Solute trapping and solute drag in a phase-field model of rapid solidification," *Physical Review E*, vol. 58, no. 3, p. 3436, 1998. 5, 5.1, 5.2.2

[8] W. Kurz and D. Fisher, *Fundamentals of solidification*. Trans Tech Publications, 1986. 1, 1.2.2, 2.2.1, 4.1, 5.1

[9] J. A. Dantzig and M. Rappaz, *Solidification*. EPFL Press, 2009. 1, 2, 2.2.1, 2.2.4, 3, 4.2.1, 5.1

[10] M. J. Aziz and W. Boettinger, "On the transition from short-range diffusion-limited to collision-limited growth in alloy solidification," *Acta metallurgica et materialia*, vol. 42, no. 2, pp. 527–537, 1994. 5.1, 5.3.2

[11] S. Sobolev, "Rapid solidification under local nonequilibrium conditions," *Physical Review E*, vol. 55, no. 6, p. 6845, 1997. 5.1

[12] Y. Yang, H. Humadi, D. Buta, B. B. Laird, D. Sun, J. J. Hoyt, and M. Asta, "Atomistic simulations of nonequilibrium crystal-growth kinetics from alloy melts," *Physical review letters*, vol. 107, no. 2, p. 025505, 2011. 5.1

[13] S. G. Kim, W. T. Kim, and T. Suzuki, "Phase-field model for binary alloys," *Physical review e*, vol. 60, no. 6, p. 7186, 1999. 2.2.3, 2.2.3, 5.1, 5.2.2

[14] D. Danilov and B. Nestler, "Phase-field modelling of solute trapping during rapid solidification of a si–as alloy," *Acta Materialia*, vol. 54, no. 18, pp. 4659–4664, 2006. 5.1

[15] P. Galenko, E. Abramova, D. Jou, D. Danilov, V. Lebedev, and D. Herlach, "Solute trapping in rapid solidification of a binary dilute system: a phase-field study," *Physical Review E*, vol. 84, no. 4, p. 041143, 2011. 5.1

[16] M. Ohno and K. Matsuura, "Quantitative phase-field modeling for dilute alloy solidification involving diffusion in the solid," *Physical Review E*, vol. 79, no. 3, p. 031603, 2009. 5.1, 5.3.1

[17] A. Carré, B. Böttger, and M. Apel, "Implementation of an antitrapping current for a multicomponent multiphase-field ansatz," *Journal of crystal growth*, vol. 380, pp. 5–13, 2013. 5.1, 5.3, 5.3.1

[18] T. Pinomaa and N. Provatas, "Quantitative phase field modeling of solute trapping and continuous growth kinetics in quasi-rapid solidification," *Acta Materialia*, vol. 168, pp. 167–177, 2019. 1.2.3, 5.1

[19] S. Kavousi and M. A. Zaeem, "Quantitative phase-field modeling of solute trapping in rapid solidification," *Acta Materialia*, vol. 205, p. 116562, 2021. 1.2.3, 5.1

[20] Y. Gu, X. He, and D. Han, "On the phase-field modeling of rapid solidification," *Computational Materials Science*, vol. 199, p. 110812, 2021. 5.1

[21] Z. Li, H. Xing, W. Lu, and X. Dong, "Quantitative phase-field modeling of directional growth with kinetic effects in quasi-rapid solidification," *Materials Letters*, vol. 311, p. 131618, 2022. 5.1

[22] K. Ji, E. Dorari, A. J. Clarke, and A. Karma, "Microstructural pattern formation during far-from-equilibrium alloy solidification," *Physical Review Letters*, vol. 130, no. 2, p. 026203, 2023. 5.1

[23] A. Mukherjee, J. A. Warren, and P. W. Voorhees, "A quantitative variational phase field framework," *Acta Materialia*, vol. 251, p. 118897, 2023. 5.1

[24] S. Kavousi, V. Ankudinov, P. K. Galenko, and M. A. Zaeem, "Atomistic-informed kinetic phase-field modeling of non-equilibrium crystal growth during rapid solidification," *Acta Materialia*, vol. 253, p. 118960, 2023. 5.1

[25] I. Steinbach, L. Zhang, and M. Plapp, "Phase-field model with finite interface dissipation," *Acta Materialia*, vol. 60, no. 6-7, pp. 2689–2701, 2012. 5.1, 5.3.2

[26] L. Zhang, E. V. Danilova, I. Steinbach, D. Medvedev, and P. K. Galenko, "Diffuse-interface modeling of solute trapping in rapid solidification: Predictions of the hyperbolic phase-field model and parabolic model with finite interface dissipation," *Acta materialia*, vol. 61, no. 11, pp. 4155–4168, 2013. 5.1

[27] W. J. Boettinger, J. A. Warren, C. Beckermann, and A. Karma, "Phase-field simulation of solidification," *Annual review of materials research*, vol. 32, no. 1, pp. 163–194, 2002. 1.1, 2.2.3, 5.2.1, 5.2.1

[28] C. Beckermann, H.-J. Diepers, I. Steinbach, A. Karma, and X. Tong, "Modeling melt convection in phase-field simulations of solidification," *Journal of Computational Physics*, vol. 154, no. 2, pp. 468–496, 1999. 2.2.1, 2.2.2, 2.2.3, 5.2.1, 5.2.1

[29] I. Steinbach, "Phase-field models in materials science," *Modelling and simulation in materials science and engineering*, vol. 17, no. 7, p. 073001, 2009. 1.1, 2, 2.2.1, 2.2.2, 2.2.5, 3.1, 3.2.1, 3.2.3, 4.2.2, 5.2.1, 5.5

[30] R. Trivedi and W. Kurz, "Solidification microstructures: A conceptual approach," *Acta metallurgica et materialia*, vol. 42, no. 1, pp. 15–23, 1994. 5.3, 5.3.1

[31] K. M. Beatty and K. A. Jackson, "Monte carlo modeling of silicon crystal growth," *Journal of Crystal Growth*, vol. 211, no. 1-4, pp. 13–17, 2000. 5.3.1

[32] R. Trivedi and W. Kurz, "Dendritic growth," *International Materials Reviews*, vol. 39, no. 2, pp. 49–74, 1994. 1.2.3, 2.1, 5.3.1, 5.3.2

[33] M. Gremaud, M. Carrard, and W. Kurz, "Banding phenomena in al fe alloys subjected to laser surface treatment," *Acta metallurgica et materialia*, vol. 39, no. 7, pp. 1431–1443, 1991. 5.3.2

Chapter 6

Concluding Remarks

The properties of crystalline materials depend largely on the microstructures formed during solidification processing. The solidification microstructure of many industrially important materials can hardly be controlled because of the unknown formation mechanisms. In this research, the phase-field method has been used to simulate the complex pattern formation in solidification associated with the simultaneous contributions of crystal anisotropy and solute redistribution. The content is summarized as follows:

Chapter 1 The microstructure problems in three different material systems have been introduced. They are multi-crystalline silicon in solar cells, $MoSi_2/Mo_5Si_3$ eutectic for ultra-high temperature application, and rapidly solidified aluminum alloys. A framework of phase-field models that can simulate the microstructure formation of these crystalline materials requires the proper description of the faceted anisotropy and equilibrium/non-equilibrium processes during solute redistribution.

Chapter 2 The fundamental solidification processes, including the interface kinetics under isothermal condition, growth of grain with anisotropic surface energy, and solute partitioning in alloy solidification, have been simulated in comparison to the analytical predictions. The criteria of accuracy in phase-field modeling has

been formulated and the artificial width of the diffuse interface has been verified to be the key limitation for quantitative simulation.

Chapter 3 To elucidate the mechanism of the grain boundary development during the directional solidification of multi-crystalline silicon, the phase-field model incorporated with anisotropic surface properties of faceted silicon crystal has been developed. The interplay between the energetic and kinetic effects of the groove surfaces has been revealed and is believed to be a key knowledge for controlling the grain structure of multi-crystalline silicon.

Chapter 4 A comprehensive study on the complex eutectic structure of MoSi2/Mo5Si3 has been presented. Based on the comparison between the numerical results and experimental observations, the formation mechanisms of the so-called script lamellar pattern have been revealed. The rod (Mo5Si3) discontinuity originates from the solid-liquid interface instability, which is represented by nucleation in this study. The inclination of rods is caused by the lattice misfit accommodation at the interphase boundary with the ledge-terrace atomic arrangement.

Chapter 5 The rapidly solidified aluminum alloy exhibits microstructures different from the dendritic patterns in casting processing. The solute redistribution in rapid solidification processing, such as additive manufacturing, is far from equilibrium. A new phase-field model that quantitatively simulates alloy solidification has developed by introducing the so-called middle-obstacle (MO). The velocity and morphology of the simulated dendrite tip can be independent of the interface width under equilibrium conditions. In addition, the model shows its capability of simulating the concentration oscillation caused by non-equilibrium solute partitioning during rapid solidification.

Chapter 6 The methodology, achievements, and implications of the present study have been briefly reviewed. In summary, this study provides a framework for constructing phase-field models to elucidate the mechanisms underlying the formation

of solidification microstructure for the development of advanced crystalline materials.

—— Postscript ——

The microstructure problems in the solidification of crystalline materials can be complex considering the multiple physical processes happening simultaneously during the motion of the solid-liquid interface, even in the case of pure substances, such as multi-crystalline silicon. The dynamics of the solid-liquid interface may become even more elusive when multiple components, phases, and orientations are considered. With the advanced experimental observation equipment, the elucidation of the fundamental mechanism remains to be challenging and cost-consuming. The numerical method is the hope of material scientists and engineers for exploring the real-time process underlying the formation process of microstructure.

In contrast, the concept of the diffuse interface is simple. It is consistent with both physical reality and human intuition. The mathematical equation that governs the motion of a diffuse interface can be derived either from the kinetic theory or the thermodynamic principles. The simplicity of the diffuse interface model persists even until the implementation in the programming languages. As long as the undercooling meets the stability criteria, the model can produce analytically-correct results in three dimensions, which should be implemented with much more effort by its sharp interface counterpart requiring explicit tracking of the interface. The simplicity and accuracy of the diffuse interface model are valid for pure substances under isothermal conditions. As the transport phenomena are considered, the inhomogeneous distribution of solute and temperature across the diffuse interface leads to width-dependent results. Nevertheless, the simplicity in the implementation of the diffuse interface remains and even the qualitative re-

sults can reveal the underlying processes that can hardly be realized by theoretical derivation or observed by the most advanced microscopy.

The power of the diffuse interface model lies in its ability to incorporate multiple physical effects into its simple governing equation with two competing terms. The driving force term can be calculated according to the various field variables (temperature, concentration, and stress). The anisotropy of the surface energy owing to the crystallographic symmetry can be appropriately incorporated into the term of the surface pressure, which counters the bulk driving force. However, no matter how exquisitely the model is designed and implemented, the validity of the simulation results needs to be verified by experimental observation. The numerical model can never produce facts but can only produce results that need to be verified. Namely, the numerical model is the playground for materials scientists to build up the imagination of what is happening in materials and which effect is dominant. The true power of the phase-field method can be unleashed only when its limitation is fully recognized.

In the present study, the focus is purely on the solid-liquid interface and the resulting pattern formation. In fact, all the microstructure problems in solidification can be reduced to the problem of the moving solid-liquid interface. Therefore, if the solid-liquid interface dynamics can be fully described, the formation of the microstructure can be understood. For example, in the directional growth of multi-crystalline silicon, two or more grains grow together along the temperature gradient. Because the surface energy and kinetic coefficient are anisotropic, the prediction of their grain boundary extension requires an accurate description of orientation-dependent properties of the solid-liquid interface; In the directional growth of eutectic with two different phases, the solid-liquid interface motion is affected by the solute exchange ahead, which may result in a complicated spacing transition process; with the incorporation of the solute redistribution in and near

the solid-liquid interface, the growing solid may develop to be a dendrite rather than a nearly spherical ball when the slight anisotropy of surface energy is incorporated. Therefore, the anisotropy and transport process need to be appropriately described to correctly simulate the interface dynamics.

The main achievements of present works lie in the descriptions of both anisotropy and solute redistribution in the phase-field models. In terms of anisotropy, the faceted shape of the silicon crystal has been successfully reproduced in comparison with the experimental observation. In addition, the description of the anisotropic surface properties is further verified by conducting a simulation of grain boundary extension under low and high cooling rates. The effects of the orientation relationship of adjacent grains and the cooling condition on the direction of the grain boundary have been thoroughly elucidated through the numerical simulation. On the other hand, in terms of solute redistribution, the coupling of the phase field and concentration field has been proven to be independent of the interface width of the diffuse interface. This means the dendrite in the binary alloy might be the "true" shape, which is completely relevant to the input physical conditions, such as temperature, surface energy, and kinetic coefficient. The capability of calculating the true shape with much less computational cost has a profound influence on computational materials science because the microstructure length and the concentration distribution can be quantitatively predicted using numerical models once the experimentally-measured properties of materials are input into the model. In the near future, the phase-field models can truly become a predictive tool rather than only elucidating the qualitative physical effects.

The modeling work using the phase-field method in this thesis has solved the three major microstructure problems, including grain selection in multi-crystalline silicon, complex Mo-Si eutectic structure, and rapid solidification of Aluminum alloy. The insights and knowledge gained from the simulation are of high value

for the development of crystal growth technology and the application of additive manufacturing, which are part of the grand field of solidification science and engineering. On the other hand, the developed phase-field models that can accurately describe faceted anisotropy and non-equilibrium kinetics can serve as the building blocks for integrated computational materials engineering (ICME). The present study contributes to the techniques and knowledge for the development of advanced materials for the sustainability of human society.

Achievements

Publications

- C. Zhu, Y. Seguchi, M. Okugawa, C. Guo, and Y. Koizumi "Influences of growth front surfaces on the grain boundary development of multi-crystalline silicon during directional solidification: 2D/3D multi-phase-field study." Materialia 27 (2023) 101702.

- C. Zhu, J. Yamamoto, Y. Koizumi, K. Yuge, K. Kishida, and H. Inui "Comprehensive Phase Field Study on Directionally-Solidified $MoSi_2/Mo_5Si_3$ Eutectic Alloy" Materials Science Forum 1016 (2021) 749-754.

- C. Zhu, Y. Koizumi, A. Chiba, K. Yuge, K. Kishida, and H. Inui "Pattern formation mechanism of directionally-solidified $MoSi_2/Mo_5Si_3$ eutectic by phase-field simulation.", Intermetallics 116 (2020) 106590.

- C. Zhu, Y. Seguchi, M. Okugawa, and Y. Koizumi "Middle-obstacle approach of mapping phase-field model to its sharp interface correspondence under universal cooling condition." Phy. Rev. E (Under review)

Other publication

- Y. Liu, M. Okugawa, K.Saito, D. Izumikawa, C. Zhu, Y. Seguchi and Y. Koizumi "Phase-Field Modeling of Spinodal Decomposition in Fe-Cr-Co Alloy under Continuous Temperature-changing Conditions" ISIJ International (2023)

International Conferences

- C. Zhu, Y. Koizumi, A. Chiba, K. Yuge, K. Kishida, and H. Inui "Pattern Formation Mechanism of Directionally-Solidified $MoSi_2/Mo_5Si_3$ Eutectic Examined by Phase Field Method" Beyond Nickel-Based Superalloy conference, Nara, 2019.6 (Oral)

- C. Zhu, Y. Koizumi, A. Chiba, K. Yuge, K. Kishida, and H. Inui "A Phase Field Study on Script Lamellar Pattern of $MoSi_2/Mo_5Si_3$ Eutectic", Materials Research Society 2018 Fall Meeting, Symposium PM06-Advances in Intermetallic-Based Alloys for Structural and Functional Applications, Boston, 2018.11 (Oral)

Domestic Conferences

- C. Zhu, Y. Seguchi, M.Okugawa and Y.Koizumi "A Phase-field Methodology for Alloy Solidification under Universal Cooling Conditions," Japan Institute of Metals and Materials Fall Conference, Tokyo, 2023.3 (Oral)

- C. Zhu, Y. Koizumi and C.Guo "Understanding the Grain Boundary Development of Silicon during Directional Solidification: Phase-Field Simulation," Japan Institute of Metals and Materials Fall conference, Fukuoka,

2022.9 (Oral)

- C. Zhu, Y. Koizumi and C.Guo "Understanding the Grain Boundary Development of Silicon during Directional Solidification: Phase-Field Simulation," Japan Institute of Metals and Materials Fall conference, Fukuoka, 2022.9 (Oral)

- C. Zhu and Y. Koizumi "Modeling of Dislocation by Phase-Field Crystal Method," Japan Institute of Metals and Materials Fall conference, Okayama, 2019.10 (Poster)

- C. Zhu, Y. Koizumi, A. Chiba, K. Yuge, K. Kishida, and H. Inui "Pattern Formation Mechanism of Directionally-Solidified $MoSi_2/Mo_5Si_3$ Eutectic by Phase Field Simulation", Japan Institute of Metals and Materials Fall Meeting, Tokyo, 2019.3 (Poster)

- C. Zhu, Y. Koizumi, A. Chiba, K. Yuge, K. Kishida, and H. Inui "A Phase Field Study on Script Lamellar Pattern of $MoSi_2/Mo_5Si_3$ Eutectic", Japan Institute of Metals and Materials Fall Meeting, Sendai, 2018.9 (Poster)

Acknowledgments

The journey of this study started from the time when I was at Tohoku University, where I met my advisor Prof. Yuichiro Koizumi. His passion for the phase-field method inspired me to explore this numerical approach and apply it to material problems. A second person I want to mention is Prof. Ingo Steinbach who is also a phase-field enthusiast. His lectures on the fundamentals of the phase field have inspired me to understand what numerical simulation really is and how to use it. The other people I would like to say thanks to are, Prof. Nicolas Provatas at McGill University, Prof. Tomohiro Takaki at Kyoto Institute of Technology, Prof. Toshiyuki Koyama at Nanoya University, and Prof. M. P. Gururajan at Indian Institute of Technology Bombay, who are the pioneers in phase-field method and helped me tremendously directly or indirectly. In the scope of materials science, I would like to say thanks to Prof. Akihiko Chiba and Prof. Kozo Fujiwara at Tohoku University who guided me to do simulations that are useful to experimenters. My sincere thanks should go to Prof. Masato Yoshiya, Prof. Takeshi Yoshikawa, and Prof. Kazunori Sato who spent precious time reviewing and correcting this thesis. I would like to say thanks again to Prof. Yuichiro Koizumi because he provided me with support and direction throughout my graduate study. The same thanks are given to Prof. Yuheng Liu, Prof. Masayuki Okugawa, and all the other members of the research group. Finally, I express my deep gratitude for the funding support from PCoMS (Professional development Consortium for

Computational Materials Scientists) and JSPS (Japan Society for the Promotion of Science).

The most special thanks are given to my family members, including my dear wife and our parents. Without their mental and financial support, I can not endure the hard times during my overseas life in Japan for over 5 years. Yes, I indeed had lots of happy times thanks to my friends and many kind neighbors. I will never forget my life experience in Japan and always try to be a good contributor to both Chinese and Japanese societies.